



**HAL**  
open science

# Soot modelling in flames and Large-Eddy Simulation of thermo-acoustic instabilities

Ignacio Hernández Vera

► **To cite this version:**

Ignacio Hernández Vera. Soot modelling in flames and Large-Eddy Simulation of thermo-acoustic instabilities. Other. Institut National Polytechnique de Toulouse - INPT, 2011. English. NNT : 2011INPT0134 . tel-04240315

**HAL Id: tel-04240315**

**<https://theses.hal.science/tel-04240315>**

Submitted on 13 Oct 2023

**HAL** is a multi-disciplinary open access archive for the deposit and dissemination of scientific research documents, whether they are published or not. The documents may come from teaching and research institutions in France or abroad, or from public or private research centers.

L'archive ouverte pluridisciplinaire **HAL**, est destinée au dépôt et à la diffusion de documents scientifiques de niveau recherche, publiés ou non, émanant des établissements d'enseignement et de recherche français ou étrangers, des laboratoires publics ou privés.



# THESE

En vue de l'obtention du

## DOCTORAT DE L'UNIVERSITÉ DE TOULOUSE

Délivré par *Institut National Polytechnique de Toulouse*  
Discipline ou spécialité : *Énergétique et transferts*

---

Présentée et soutenue par *Ignacio HERNÁNDEZ VERA*  
Le 14 décembre 2011

Titre :  
*Soot modeling in flames and Large-Eddy Simulations of  
thermo-acoustic instabilities*

---

### JURY

*A. Trouvé Rapporteur*  
*P. Bruel Rapporteur*  
*J.B.W. Kok Examineur*  
*F. Dupoirieux Examineur*  
*T. Poinsot Examineur*

---

Ecole doctorale : *Mécanique, Énergétique, Génie Civil et Procédés*  
Unité de recherche : *CERFACS (réf : TH-CFD-11-123)*  
Directeur(s) de Thèse : *Bénédicte Cuenot, Gabriel Staffelbach*  
Rapporteurs : *Arnaud Trouvé, Pascal Bruel*



# Table of Contents

<b>Abstract / Résumé</b>	<b>7</b>
<b>Acknowledgements</b>	<b>9</b>
<b>Preface</b>	<b>11</b>
<b>1 General introduction</b>	<b>13</b>
1.1 Context . . . . .	13
1.2 Objectives of this thesis . . . . .	17
<b>I Soot formation modeling in flames</b>	<b>19</b>
<b>2 Brief review of soot modeling</b>	<b>21</b>
2.1 The challenges of soot modeling and simulation . . . . .	21
2.2 State of the art of soot modeling . . . . .	22
2.3 Review of application cases . . . . .	23
<b>3 Methodology</b>	<b>25</b>
3.1 Choice of the soot model . . . . .	25
3.2 Numerical tools for soot modeling . . . . .	27
<b>4 Test cases</b>	<b>35</b>
4.1 Non-radiative cases . . . . .	36
4.1.1 Non-premixed flames . . . . .	37
4.1.2 Premixed flames . . . . .	42
4.2 Soot/gas/radiation coupling . . . . .	52
<b>5 Conclusions and perspectives I</b>	<b>55</b>
5.1 Conclusions on soot modeling . . . . .	55
5.2 Perspectives . . . . .	56

<b>II</b>	<b>LES of thermo-acoustic instabilities</b>	<b>59</b>
<b>6</b>	<b>Introduction</b>	<b>61</b>
6.1	Theory and phenomenology of CI . . . . .	61
6.2	Numerical tools for CI . . . . .	65
6.2.1	Large Eddy Simulation for CI . . . . .	65
6.2.2	Acoustic solver for CI . . . . .	69
<b>7</b>	<b>Configuration: the LIMOUSINE test rig</b>	<b>71</b>
7.1	Objectives . . . . .	71
7.2	Geometry and operating characteristics . . . . .	72
7.3	Measurement devices . . . . .	74
7.4	Experiments . . . . .	75
<b>8</b>	<b>LES of the LIMOUSINE test rig</b>	<b>79</b>
8.1	Computational parameters . . . . .	79
8.2	Presentation of simulations . . . . .	85
8.2.1	Simulations performed . . . . .	85
8.2.2	Computational ressources and cost . . . . .	85
8.3	Simulation 1: reference case for OP1 . . . . .	86
8.3.1	Cold flow . . . . .	86
8.3.2	Hot flow . . . . .	89
8.4	Simulation 1.1: influence of fuel inlet conditions . . . . .	106
8.5	Simulation 1.2: influence of air inlet conditions . . . . .	108
8.6	Simulations 1.3 and 1.4: influence of mesh . . . . .	109
8.7	Simulation 1.5: influence of adiabaticity . . . . .	115
8.8	Simulation 1.6: influence of radiative heat losses . . . . .	116
8.9	Simulation 2: influence of the OP. . . . .	119
8.10	Simulation 3: influence of burner geometry . . . . .	124
8.11	Comparison with experimental results . . . . .	128
8.11.1	Version V.3 at OP1 . . . . .	128
8.11.2	Version V.3 at OP2 . . . . .	132
8.11.3	Version V.2 at OP1 . . . . .	133
<b>9</b>	<b>Conclusions and perspectives II</b>	<b>135</b>
9.1	Conclusions on LES of thermo-acoustic instabilities . . . . .	135
9.2	Perspectives . . . . .	136
	<b>References</b>	<b>150</b>
	<b>Appendices</b>	<b>153</b>
<b>A</b>	<b>The 1D code <i>CAN2SOOT</i></b>	<b>153</b>
A.1	Introduction . . . . .	153
A.2	Derivation of the equations . . . . .	153
A.2.1	Soot model and simplifications . . . . .	153
A.2.2	Discretization . . . . .	154

A.3 Numerical solution . . . . .	155
A.3.1 Problem formulation . . . . .	155
A.3.2 Problem solution . . . . .	156



# Abstract

In the first part of the present PhD. thesis a methodology is presented that allows to predict the soot produced in one-dimensional academic flames, where a semi-empirical soot model is used in combination with a complex chemistry and a detailed radiation solver. The methodology is applied to the computation of soot in a set of ethylene/air counterflow diffusion flames. Several oxidation models are tested and the constants of the model were adjusted to retrieve the experimental results. Also, the effect of radiative losses on soot formation and the flame structure is evaluated. Finally, the performance of the soot model is evaluated on 1D premixed flames, where an alternative expression for the surface growth term is proposed to better reproduce the experimental findings.

In the second part of the thesis, Large-Eddy Simulation (LES) and acoustic analysis tools are applied to the prediction of limit cycle oscillations (LCO) of a thermo-acoustic instability appearing in a partially premixed methane/air academic burner operating at atmospheric pressure. The LES captures well the appearance and development of the LCO and a good agreement is found between simulations and experiments in terms of amplitude and frequency of the LCO. Some light is shed on the mechanisms leading to the existence of such instability. Then, a preliminar uncertainty quantification (UQ) analysis is performed, where the effect on the features of the LCO of several computational parameters such as the inlets impedances, mesh refinement or heat losses is assessed. Also, the LES captures well the flame stability behaviour dependence on the operating point and the burner geometry.

**Keywords:** Soot, radiation, combustion, Large-Eddy Simulation, acoustics, thermo-acoustic instabilities, limit-cycles, heat losses.

# Résumé

Dans la première partie de cette thèse de doctorat une méthodologie est présentée qui permet de prédire les niveaux de suies produits dans des flammes laminaires monodimensionnelles, ou un modèle semi-empirique de suies est utilisé en combinaison avec une chimie complexe et un solveur radiatif détaillé. La méthodologie est appliquée au calcul de suies dans une série de flammes de diffusion à contre-courant d'éthylène/air. Plusieurs modèles d'oxydation de suies sont testés et les constantes du modèle sont ajustées afin de retrouver un meilleur accord avec les expériences. L'effet des pertes thermiques radiatives sur la formation de suies et la structure des flammes est évalué. Finalement, la performance du modèle de suies est évalué sur des flammes prémélangées monodimensionnelles, ou une expression alternative du terme de croissance de surface est proposée pour reproduire les résultats expérimentaux.

Dans la deuxième partie de cette thèse, des outils de Simulation aux Grandes Échelles (SGE) et d'analyse acoustique sont appliqués à la prédiction des oscillations de cycle limite (OCL) d'une instabilité thermo-acoustique qui apparaît dans un brûleur académique partiellement prémélangé de méthane/air à pression atmosphérique. La SGE prédit bien l'apparition et le développement des OCL et un bon accord est trouvé entre simulations et expériences en termes d'amplitude et fréquence des OCL. La simulation permet de révéler certains aspects clés responsables du comportement instable de la flamme. Ensuite, une analyse préliminaire de la quantification des incertitudes est faite, ou l'effet des paramètres tels que l'impédance des entrées, le degré de raffinement du maillage ou les pertes thermiques sur les caractéristiques des OCL est évalué. Aussi, la SGE prédit bien la dépendance de la stabilité de la flamme du point d'opération et de la géométrie du brûleur.

**Mots clés:** Suies, rayonnement, combustion, Simulation aux Grandes Échelles, acoustique, instabilités thermo-acoustiques, cycles limite, pertes thermiques.

# Acknowledgements

## Remerciements / Agradecimientos

Tout d'abord je tiens à remercier les seniors du CERFACS : Bénédicte Cuenot, Thierry Poinot et Laurent Gicquel, pour avoir su m'encadrer et pour partager leurs connaissances, j'ai énormément appris pendant mes trois années de thèse.

Likewise, I thank Professor Jim Kok and his team (Reddy, Juan Carlos, Mehmet, Can, Santosh and Mina) for their warm welcome during my stay at the *University of Twente* in April 2011.

Ensuite, je voudrais remercier (par ordre chronologique) : Eléonore Riber, Olivier Vermorel, Olivier Cabrit, Jorge Amaya, Marta García, Benedetta Franzelli (la reine de *CANTERA!*), Gabriel Staffelbach et Damien Poitou pour avoir répondu à toutes mes questions (dont une partie non-négligeable s'avérait, sans doute, des bêtises!). Un remerciement spécial est adressé à Guillaume Lecocq, pour m'avoir aidé pendant les moments critiques de la thèse et pour garder foi en moi quand je n'y croyais plus.

Je voudrais remercier (bien sûr!) les collègues (et amis) du CERFACS (ou d'ailleurs) avec lesquelles j'ai partagé de belles et enrichissantes expériences pendant ces trois dernières années, à savoir (par stricte ordre alphabétique) : Alex, Anthony, Basti, David, Greg, Jean Baptiste, Jean Philippe, Logan (a.k.a. Mr. BBQ), Marina, Matthias, Nacho, Patricia, Sabrina, Stephan, Thomas et Victor.

I also would like to thank the "Limousine crew" for the great weekends spent together in random cities around Europe: Bela, Patrick, Salvo, Sebastian, Harmen, Basti, Can, Mehmet, Juan Carlos, Santosh, Mina, Roel, Thomas, Lukas, Antonio and Simone.

Y por supuesto le agradezco a mis padres el apoyo brindado desde la distancia que, sin duda, ha sido un factor clave en la finalización de mi tesis.

Funding from the European Commission, within the Marie Curie Actions - Initial Training Networks, under call FP7-PEOPLE-2007-1-1-ITN, LIMOUSINE project with number 214905, is gratefully acknowledged.



# Preface

The work presented herein has been carried out as part of the LIMOUSINE project (**L**imit cycles of thermo-**a**coustic oscillations in gas turbine combustors), within the framework of the Marie Curie Actions and funded by the European Commission. The project is participated by several academic as well as industrial partners and coordinated by Prof. J.B.W. Kok, from the University of Twente (The Netherlands).

The project is devoted to the study of the limit-cycle behaviour of the acoustic pressure oscillations within the combustion chamber of gas turbines and the subsequent mechanical vibrations induced on the structural components. It constitutes a multidisciplinary approach whose final goal is to provide answers to the current needs of the gas turbine industry in Europe. The project aims, then, to come up with fundamental understanding of these complex phenomena. It also expects to create a new generation of young engineers and scientists with the necessary skills to support the gas turbine manufacturers in Europe.

The project provides research training and support in various topics such as:

- Combustion
- Acoustics
- Aerodynamics
- Structural mechanics
- Materials science
- Active control

The study of these topics is tackled using diverse approaches such as theoretical work, numerical analysis and experimental techniques. More importantly, the LIMOUSINE project provides a framework and the necessary infrastructures to allow for the knowledge exchange between researchers, as it is important to look at these topics as making part of an ensemble, as will be explained further in this work.



# Chapter 1

## General introduction

### 1.1 Context

There are numerous aspects motivating the improvement of the energetic efficiency and operation performance of combustion systems. Nowadays 90% of the energy produced on earth is done so through the combustion of fossil fuels [132].  $CO_2$  emissions of anthropogenic nature (see Fig. 1.1) are responsible for global warming due to the greenhouse effect, whereby gases present in the atmosphere act as a radiation trap, diminishing the radiation emitted to the atmosphere and leading to a rise in the mean temperature of the Earth [82]. The long term effects of global warming are devastating, it is a must to play an active role in the attenuation of greenhouse gases emissions. From an economic point of view, costs associated to fossil fuels consumed by countries for industry, transportation, etc, constitute a significant part of their GNP. Besides, petroleum depletion is a reality, expected to take place before the end of the present century, hence the growing concern on the management and utilization of such resources.

In particular, gas turbines constitute an interesting alternative for energy production, where the energy contained in the fuel used is transformed into mechanical energy through combustion (natural gas is the most commonly used fuel, although other fossil fuels such as synthesis gas are being used more and more). Their development was motivated by military applications in the first half of the XXth century and their performance has been greatly increased since then [131]. Gas turbines can be found in sizes ranging from microturbines used for distributed power generation of less than 1 MW of power, or even less, to stationary industrial gas turbines, delivering powers of more than 200 MW (Fig. 1.2).

The development of new technologies for efficient combustors with limited climate impact can not be achieved without high-fidelity simulations. This

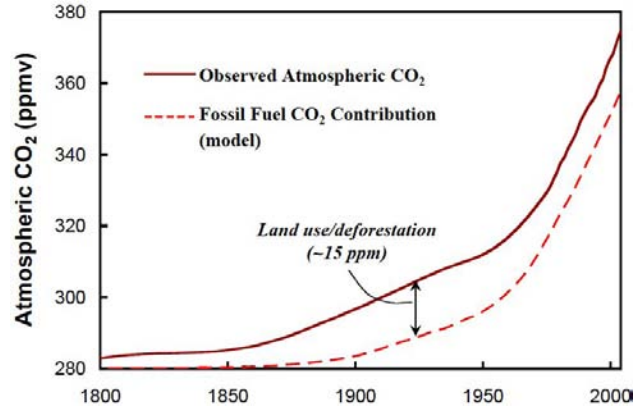


**Figure 1.1:** Measured and predicted atmospheric  $CO_2$  content, from Kharecha [76].

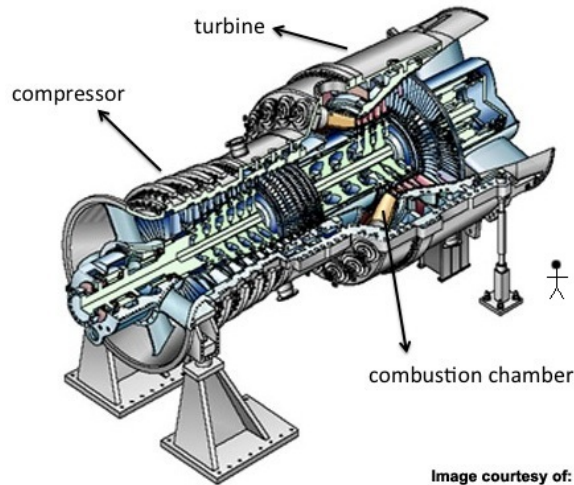


**Figure 1.2:** The SGT5-8000H developed by Siemens is the largest gas turbine in the world. Installed at a combined-cycle power plant in Irsching (Germany) with a cycle power output of 545 MW and a global efficiency of 60 %.

statement is often heard in the combustion community but today it leads to new questions in terms of simulations. Of course, CFD methods are currently used to design combustors and numerical combustion has become a standard tool in most companies [117]. However combustion simulation codes are still unable to address multiple questions which are critical for tomorrow's combustion chambers. This thesis focuses on two of these issues:

1. Soot emission by flames remains a difficult challenge for combustion simulations and, in most cases, is simply ignored. However, there are numerous reasons why soot formation in flames is worth being accounted for

[17, 104]. Soot present in the exhaust gases of commercial aircrafts engines may change the physico-chemistry of the atmosphere, as they trigger the nucleation of cirrus clouds [73], which in turn changes the climate in high air traffic zones as a result of a radiative balance. The exhaust gases released at ground level from vehicles (mainly Diesel engines) contain soot particles, which are hazardous for human health [70]. Soot also plays a major role in devices such as industrial furnaces (Fig.1.3(a)) or boilers, where the goal is to maximize the heat exchange through radiation to a load. In this sense, soot particles are desirable within the furnace, but unwanted at the outlet [151]. This poses technical challenges to designers, which can only be overcome if the phenomenology of soot formation and oxidation is well understood. Besides, soot-driven radiation is important in the development of wildfires (Fig.1.3(b)) and compartment fires [148]. Finally, heat fluxes to the liner walls of gas turbine combustion chambers must be correctly predicted to evaluate walls life-cycle [86].

2. The constraints imposed on the pollutant levels (such as  $NO_X$  or soot for example) being produced in combustion chambers have led to the development of Lean Premixed (LP) combustion technologies. Unfortunately, it is well known that LP combustors are prone to combustion instabilities (CI) when operated [45]. These oscillations appear in most chambers and are usually due to coupling between acoustics and unsteady flame movements [26, 38, 44, 92, 116, 117]. When a combustor is submitted to combustion instabilities, it usually leads to structure damages, flashback, quenching or loss of control. It must be avoided at all costs. Unfortunately, the prediction of instabilities at the design stage remains a considerable task and CFD codes today are unable to meet this challenge. If CI appear when the engine is already in operation, it can lead to catastrophic failures and loss of human lives. Virtually all kinds of high-performance engines exhibit CI at some stage of their development, necessitating costly modifications or restrictions in their operating range. The case of rocket engines (solid or liquid propulsion) may be the most significant because CI were encountered since the early developments in the 1930s and it is still an active research field (see for example the French-German cooperation within the REST committee). For industrial gas turbines, the occurrence of CI is a common problem and most companies (such as Alstom, Siemens or Ansaldo) have been addressing these issues for a long time. Their interest in understanding and predicting CI allowed leading research on their specific geometries as well as more fundamental activities through European projects such as FUELCHIEF and PRECCINSTA for example. In the case of aeronautical engines, CI are the source of tremendous difficulties. For example, significant progress within European companies to design low  $NO_X$  combustion chambers lead, in most cases, to engines exhibiting CI that could not be commercialized despite being very efficient in terms of  $NO_X$  mitigation. In industrial furnaces or even domestic heaters, CI



(a)



(b)

**Figure 1.3:** Large sooting flames found in (a) Glass furnaces. (b) Wildfires.

are also observed and often handled with the same (costly) trial-and-error approach.

These two issues have to be viewed today in the field of LES (Large Eddy Simulations) methods which are replacing classical RANS (Reynolds Average Navier Stokes) techniques. RANS have reached today a level of maturity and development which limits their future improvements. As emphasized by the recent DOE report [8] dedicated to High Performance Computing (HPC), replacing RANS by LES today makes sense because HPC allows to simulate combustors with LES on thousands of processors in a short time and with an accuracy and reliability which can not be reached with RANS [7, 97, 112, 128, 134]. However, this requires developing submodels for LES which are adapted to these tech-

niques, one of the goals of the present work.

Note that CI's are often directly influenced by heat losses [134, 138] so that both aspects studied in this work (soot formation and CI) are linked.

## 1.2 Objectives of this thesis

The objective of the present work is to make progress in two fields:

- Models for soot formation.
- Sensitivity of combustion instability models.

Both studies will be performed in the framework of LES tools. The two issues are linked: without a good model for soot, the level of heat losses can not be determined and this work will show that combustion instabilities are very sensitive to heat losses. On the other hand, any level of combustion instability will also alter soot emission. Therefore these issues are obviously coupled in any combustion chamber. To study them however, it is more convenient to use a 'divide and conquer' approach and to study them separately, especially when validation using experimental data is required. This is what was done here: The soot level at the exhaust remains a design constraint for multiple combustion chambers but reliable models for soot emission are still missing. In this thesis, we will develop soot models for laminar and turbulent flames and validate them on a set of simple flames (Part I).

In the field of combustion instabilities, recent progress in simulations has been tremendous and LES codes today are capable of simulating full annular chambers of gas turbines and capturing their unstable modes [144, 145]. A major difficulty encountered during these developments is the sensitivity of results to many input parameters: chemical models, wall temperatures, small changes in boundary conditions, etc. This is not surprising and most experimentalists know how sensitive combustion oscillations can be to multiple parameters. However, it raises new scientific questions on the use of LES for instabilities: what is important and what is not to simulate the unstable modes of a given burner? At which level of precision must the LES be extended? For example, is it important to include radiation, heat losses, fully detailed geometry, sophisticated chemistry? In Part II of this thesis, these points are studied by computing a new burner installed at Twente University in the framework of the Limousine European project coordinated by Prof. J.B.W. Kok. This burner has been computed with LES and we will investigate the sensitivities of the computation to multiple parameters. More generally, this part will fit into the question of UQ (Uncertainty Quantification) methods for thermoacoustics. UQ for fluid mechanics is a fast growing field (see for example work at Stanford University by Prof. Iaccarino or at Paris VI by Prof. Sagaut) but UQ for thermoacoustics is a virtually untouched topic. What makes UQ for thermoacoustics an interesting research field is that the response of combustion to acoustic perturbations is a

strongly non-linear function of a great number of parameters (both physical and geometrical) so that the occurrence of CI is subject to bifurcation, hysteresis and other sharp or even discontinuous variations. Consequently, the combustion community (researchers and industries alike) is facing considerable difficulties to predict CI in a reliable way at the design stage of combustion chambers and UQ studies have become necessary.

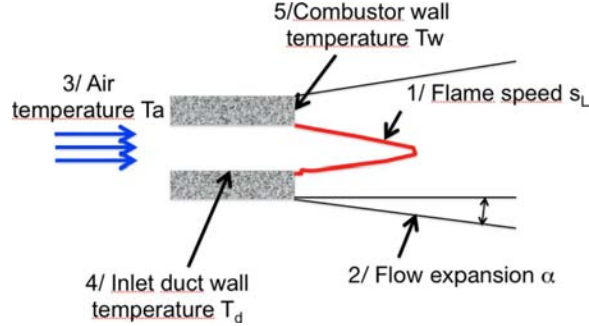


**Figure 1.4:** Uncertainty quantification in a laminar premixed flame [137].

One example of simple UQ study for combustion instability is the work of Selle *et al.* [137] performed for a laminar Bunsen-type flame (Fig. 1.4) where the effects of air and wall temperature as well as flame speed and flow expansion on the flame transfer function were studied. Results showed that the most important parameter (controlling the flame response in terms of delay) was the value of the flame speed and the temperature of the duct walls where the premixed gas is injected ( $T_d$  in Fig. 1.4). Both parameters are submitted to large uncertainties and both control the flame response: the flame speed is determined by chemical kinetics and remains a difficult quantity to predict accurately (typically for the flame of Fig. 1.4, an uncertainty on laminar flame speed of 2 cm/s, corresponding to 5% error, must be expected). The temperature of the inlet duct requires a dual heat transfer computation because this duct is cooled by the fresh gas and heated by the flame: here large uncertainties (of the order of 50 to 100 K) must be expected. As a consequence, if one must predict the flame response of the system of Fig. 1.4, the uncertainty on the flame response associated to these two uncertain parameters can be significant and change the conclusions of a computation from 'stable' to 'unstable'. Obviously, this type of uncertainty must be evaluated and controlled: in the example of Fig. 1.4, results show that efforts will be required to better characterize the flame speed (by separate measurements or additional chemistry computations) and the inlet duct temperature (by measuring it or by performing an additional preliminary dual heat transfer simulation). This result was obtained for a simple low-power premixed flame. In the present work, a turbulent non-premixed flame will be considered: this is a much more complicated device and it is difficult to say a priori which parameters will be determinant in controlling the flame instabilities. This will be the objective of Part II in the present thesis.

## Part I

# Soot formation modeling in flames



## Chapter 2

# Brief review of soot modeling

### 2.1 The challenges of soot modeling and simulation

In the field of numerical simulation of combustion processes there exist few points that bear such a high level of complexity as that presented by the prediction of soot formation. The difficulties encountered in the simulation of such phenomenon lies, not only on fundamental concepts, but also on technical aspects. These two points are interrelated.

From a fundamental point of view, the understanding of the physical and chemical phenomena leading to the formation of soot particles is incomplete. The work performed by the team of Prof. Frenklach [6, 23, 54, 56, 57, 74] among other authors has enormously contributed to the development of this particular field. The chemistry of soot is very complex, in the sense that the initial formation and later growth of soot particles depends on extremely complex chemical paths involving typically hundreds of species and chemical reactions. Even though these mechanisms have been partially deciphered, there are still aspects yet to be discovered.

Also, it is not sufficient with describing the amount of soot mass production, but it is also interesting to predict the size of the particles and their spatial distribution, which brings additional complexity to the problem. Moreover, soot particles adopt complicated shapes when they start to interact together by coalescence (see Fig. 3.1), which is not easy to model.

In addition, computations of soot formation usually necessitates the inclusion of additional physical models such as thermal radiation, as soot has been shown to have a strong impact on the thermal radiation field due to its radiative properties [75, 151].

From a technical viewpoint the problems arising are steadily being overcome due to the fast development of computing technology. However, accurate computations of soot formation in complex geometries are still far from the present capabilities. One could imagine that, in order to predict soot accurately, the whole chemical path leading to soot formation, oxidation and growth should be described. The description of such chemical mechanisms necessitates the need to describe the formation of numerous chemical species, up to benzene and higher aromatics. This approach usually leads to a large number of chemical species and reactions.

This aspect, together with the polydispersion of soot particles sizes and the additional physical models needed which lead to high computational costs, which is not always affordable, or even available nowadays.

But again, it is often possible to work around these problems. The interest in developing computational methods for soot production has led to the development of cheapest (although less accurate) approaches for soot prediction, which make use of chemical mechanisms reduction [55], tabulation techniques [84], etc. Some of these approaches will be discussed in Section 2.2.

## 2.2 State of the art of soot modeling

There are many soot formation and oxidation models available in the literature. According to Kennedy [75], soot models can be classified in order of growing complexity as empirical, semi-empirical and detailed models:

- Empirical correlations are based on global quantities obtained with experimental measurements. They aim at predicting sooting tendencies of pure fuels or fuel blends [25] rather than providing with local quantities. They are a very first approach towards the identification of potential soot-emitting systems.
- Semi-empirical models, on the other hand, model the soot formation locally, including some physico-chemical phenomena [62] leading from the main fuel [10, 11, 80, 102] or an intermediate species [89] to the formation, further growth and oxidation of soot particles. Yet, they are still ad-hoc models, in the sense that they are not free from constants adjusted empirically to fit the soot measurements in a particular type of burner, fuel and combustion regime. These models are usually monodisperse, in the sense that only the average particle size is considered at each point of the domain. They remain the best choice when quick estimations of soot levels are sought.

Polydisperse models take into account the transport of soot particles of different sizes, their distribution features described by a particle size dis-

tribution function (PSDF). Several approaches exist for the solution of this PSDF. Stochastic methods [12] make use of the Monte Carlo method to address this problem. There exist some models based on the method of moments (MOM) [50, 54, 104], which aim at reconstructing the PSDF by transporting a finite number of its moments. An alternative method is known as the discrete sectional method (DSM) [39, 106], which classify the soot particles into sections of growing size, within each of them the size distribution is continuous and its shape is presumed. These models are valid for a wide range of fuel types and operating conditions and they provide with a detailed description of the soot particles characteristics. This allows to get a further comprehension of the phenomenology of soot formation, at the expense of a high computational cost due to the number of extra variables to be transported.

When it comes to the understanding of soot inception and growth, PAH have been identified as the species leading to the formation of the nascent soot particles [62]. Since acetylene ( $C_2H_2$ ) is the main precursor of PAH, the formation and growth of soot particles are directly linked to the  $C_2H_2$  concentration. As it should be expected, the further up the chemical species is taken as soot precursor, the more accurate the model will be. This is the reason why soot is usually calculated in combination with detailed chemical schemes, which can provide the soot model with the soot precursors requested.

- Finally, detailed models [23, 98, 104] are an attempt to take into account all the phenomenology of soot formation from the decomposition of the main fuel, through the appearance of intermediate species and polyaromatic hydrocarbons (PAH) all the way down to the inception of the first soot particles and beyond. This approach provides with estimations of soot formation valid for a wide range of fuel types and operating conditions. Their drawback is their high computational cost, as a result of the large number of additional species to be transported, which render them prohibitive for their application on industrial geometries.

## 2.3 Review of application cases

Extensive work exists in the literature dealing with simulations of soot production in laminar [27, 72, 80, 100, 105, 143, 152] and turbulent [20, 22, 50] diffusion flames at atmospheric pressure. Detailed validation of the numerical simulations is possible thanks to the numerous experimental publications describing well-characterized flames, such as [1, 22, 85, 122, 143].

Numerical [43, 49, 100] and experimental [2, 154] work has also been published, to a much lesser extent, on soot production in premixed flames. The

effect of pressure on soot formation has been investigated. High soot levels are observed in flames operating at high pressure, representative of the conditions usually found in gas turbines or internal combustion engines [18].

Soot modeling strategies have been proposed for turbulent combustion in the frameworks of RANS [21] and LES [48–50] and applied to academic cases, typically ethylene/air jet flames. The interaction between soot formation and turbulence is of outmost importance for these applications, as the dependence of soot formation with temperature and chemical species is highly non-linear. Soot formation at the sub-grid scale needs advanced models able to capture this dependence so as to provide with the right soot formation and oxidation rates.

Attempts have also been made on the application to complex scenarios such as gas turbines combustion chambers [21] or compartment fires [148]. In the field of Diesel engines it is worth citing the works by Wooldridge [64] and Marchal [96]. The latter one utilizes a sectional approach to predict soot formation within an experimental test rig representative of Diesel engines technology. In particular it is focused on the prediction of particles size distribution.

For such complex configurations, usually a trade-off is made between computational cost and accuracy in the soot predictions, and semi-empirical soot models are usually selected for this kind of simulations. Soot prediction models and strategies for its application to industrial combustion systems is advancing at a fast pace, although at the moment a complete model is lacking allowing to accurately predict soot levels at the burners outlet, and also at the outlet of the whole system (at the outlet of the turbine in a gas turbine engine). The advances in this field will continue to develop due both to the efforts of the scientific community and to the parallel increase in computing power.

# Chapter 3

## Methodology

### 3.1 Choice of the soot model

The objective of this work is to study the behaviour and the control parameters of a soot model in view of a future implementation in a 3D CFD solver for the application to soot predictions in industrial geometries. Prior to that step, the model parameters must be optimized and the results validated in academic laminar flames. As the choice of the soot model is usually a tradeoff between accuracy and computational cost, the semi-empirical model proposed by Leung *et al.* [89] has been chosen, as it provides good estimations of the soot levels at a fairly low computational cost. Leung's soot model considers two transported variables, the soot mass fraction  $Y_s$  and the soot particle number density  $n$ . Their conservation equations are:

$$\frac{\partial \rho Y_s}{\partial t} + \frac{\partial \rho Y_s u_i}{\partial x_i} = -\frac{\partial}{\partial x_i} (\rho Y_s V_{t,i}) + \dot{\omega}_s'' \quad (3.1)$$

$$\frac{\partial}{\partial t} \left( \rho \frac{n}{N_A} \right) + \frac{\partial}{\partial x_i} \left( \rho \frac{n}{N_A} u_i \right) = -\frac{\partial}{\partial x_i} \left( \rho \frac{n}{N_A} V_{t,i} \right) + \dot{\omega}_n'' \quad (3.2)$$

where  $\rho$  and  $u_i$  are the density and the velocity in the  $i$  direction respectively, and  $N_A = 6.022 \cdot 10^{26}$  [*particles/kmol*]. The terms on the right hand side of the equations correspond, respectively, to the thermophoretic transport and the source terms:

- Thermophoretic velocity

$$V_{t,i} = -0.54 \frac{\mu}{\rho} \cdot \frac{1}{T} \cdot \frac{\partial T}{\partial x_i} \quad (3.3)$$

Thermophoresis is the physical phenomenon whereby soot particles in presence of a temperature gradient are driven towards lower temperature

zones. The contribution of this phenomenon to the net transport velocity is accounted for through the inclusion of the thermophoretic velocity  $V_{t,i}$ .

- Soot mass fraction source term  $\dot{\omega}_s''$

$$\dot{\omega}_s'' = M_s \left[ \underbrace{k_1(T) [C_2H_2]}_{\text{nucleation}} + \underbrace{k_2(T) f(S) [C_2H_2]}_{\text{surface growth}} - \underbrace{k_3(T) S [O_2]}_{\text{oxidation}} \right] \left[ \frac{kg}{m^3 \cdot s} \right] \quad (3.4)$$

- Soot particle number density source term  $\dot{\omega}_n''$

$$\dot{\omega}_n'' = \frac{1}{N_A} \left[ \underbrace{\frac{2}{C_{min}} N_A k_1(T) [C_2H_2]}_{\text{nucleation}} - \underbrace{2C_a \left( \frac{6M_s}{\pi\rho_s} \right)^{1/6} \left( \frac{6\kappa T}{\rho_s} \right)^{1/2} C_s^{1/6} [\rho n]^{11/6}}_{\text{coagulation}} \right] \left[ \frac{kmol}{m^3 \cdot s} \right] \quad (3.5)$$

where  $C_{min} = 100$  is the number of carbon atoms in a nascent soot particle,  $C_a = 9.0$  is an agglomeration rate constant,  $\kappa = 1.38 \cdot 10^{-23} [J/K]$  is the Boltzmann constant,  $\rho_s = 2000 [kg/m^3]$  is the soot density,  $M_s = 12.011 [Kg/Kmol]$  is the molar mass of soot,  $S$  is the soot surface area per unit volume and  $C_s = \rho Y_s / M_s$  is the soot concentration. The reaction rates  $k_i(T)$  are of the form  $k_i(T) = A_i T^{n_i} e^{-T_i/T} [s^{-1}]$  and the constants  $A_i$ ,  $n_i$  and  $T_i$  are shown in Table 3.1. The constants of the model were adjusted by Leung and coworkers to retrieve the soot levels measured experimentally in a set of ethylene/air counterflow diffusion flames by Vandsburger *et al.* [150].

$A_1$	$A_2$	$A_3$
$0.1 \cdot 10^5$	$0.6 \cdot 10^4$	$0.1 \cdot 10^5$
$T_1 [K]$	$T_2 [K]$	$T_3 [K]$
21100	12100	19680
$n_1$	$n_2$	$n_3$
0	0	0.5

**Table 3.1:** Leung's soot model constants.

The source terms describe the physico-chemistry of soot formation. Four stages are identified:

1. **Nucleation:** inception of a new soot particle from its precursors. Acetylene is considered as the sole soot precursor, the inception rate is therefore proportional to the  $C_2H_2$  concentration (in  $[kmol/m^3]$ ).

2. **Surface growth:** increase in mass of soot particles due to the addition of carbon by chemical reactions occurring on the particles surface. The function  $f(S)$  in Eq. (3.4) expresses the dependence of the soot surface growth term on the soot surface area. In the model,  $f(S) = \sqrt{S}$ , which is a simple expression that accounts for the effect of the so-called particle aging, *i.e.* the reduction in reactivity of soot particles as they traverse the flame, which slows down their surface growth rate. The underlying physics of this aging process is still not fully understood, the most known theory being that of Frenklach and coworkers [74], referred to as the hydrogen-abstraction-carbon-addition (HACA) mechanism. This theory explains the growth of PAH as a function of the local availability of hydrogen radicals. This mechanism is thus extended to the surface growth of soot particles, which will as well be dependent on the  $H$  atoms concentration, which will activate their surface prior to the addition of carbon mass. As  $H$  depletion takes place (usually out of the reactive fronts), soot particles experience a reduction in surface growth rate due to the diminishing number of active sites. This confines soot surface growth to the regions where  $H$  radical is present. The dependence of the surface growth rate on the  $H$  concentration is not accounted for in Leung's model, but it is only proportional to the  $C_2H_2$  concentration.
3. **Coagulation:** binding of two soot particles to form a bigger one. It only depends on the temperature and on the particles number density. It constitutes a sink term in Eq. (3.2) since the effect of coagulation is to reduce the number of particles while the total mass of soot is conserved.
4. **Oxidation:** consumption of soot mass by oxidizing species on the soot particles surface. Leung's model only considers oxidation by  $O_2$  species. However, oxidation by  $OH$  is important [35] and its inclusion in the model is deemed necessary [52, 102]. The effect of soot oxidation by  $OH$  is evaluated further in this work.

Leung's model is monodisperse, as only one averaged soot particles size is considered to exist at a particular location in space and instant of time. Soot particles are supposed to take on a spherical shape, hypothesis which is plausible for incipient particles, but which starts to differ from reality as soot particles start to coalesce. Soot aggregates are the result of the collision of elementary soot particles, that bond together to form bigger, complicated fractal-like structures, as seen in Fig. 3.1.

## 3.2 Numerical tools for soot modeling

1. The open source software *CANTERA* [41] was used to compute one-dimensional premixed and diffusion flames, allowing then to obtain temperature, velocity and chemical species profiles. To model the gas-phase chemistry, several mechanisms were considered: GRI-Mech 3.0 [142], ABF

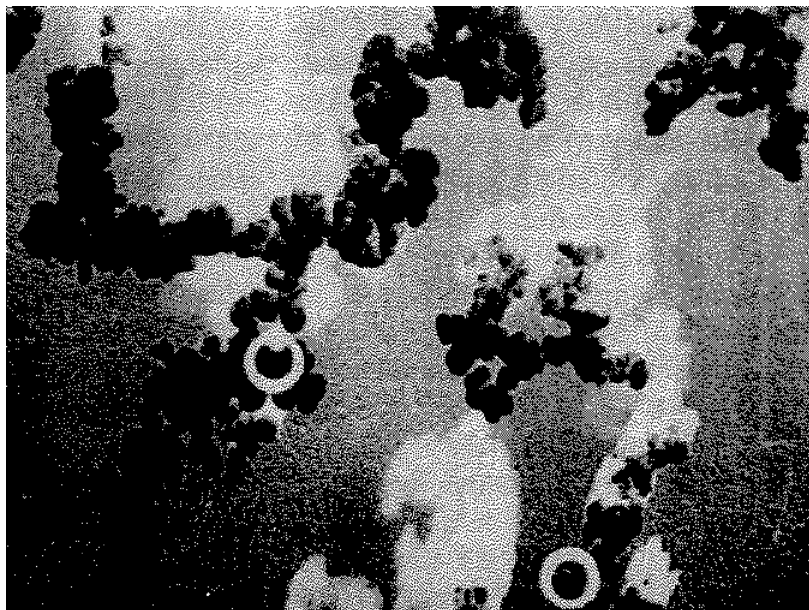


**Figure 3.1:** Electron micrograph of soot particles of mean diameter 20 nm, from Haynes [62]. Elementary soot particles (highlighted in white) coalesce to form large soot aggregates.

[6], Blanquart [17], UDEL [40] and UCSD [149].

In order to assess their capabilities, several ethylene/air, one-dimensional, freely-propagating laminar flames at atmospheric pressure were computed. The computed adiabatic flame temperature  $T_{ad}$  is shown in Figure 3.2. There is good agreement among the different mechanisms. Only GRI-Mech 3.0 slightly underpredicts  $T_{ad}$  with respect to the others. Figure 3.3 shows a comparison between experimental (symbols) and computed (lines) laminar flame speeds,  $S_L$ , for different values of the equivalence ratio  $\Phi$ . GRI-mech 3.0 and ABF yield values of  $S_L$  between 20% and 35% higher than the experimental values. Blanquart agrees well with the experiments along the whole range of  $\Phi$  studied. UCSD slightly overpredicts  $S_L$  for  $\Phi < 1.3$  but agrees well for richer flames. UDEL predicts values of  $S_L$  of about 6% higher for stoichiometric flames, and agrees well for lean and rich mixtures.

Considering these results, only Blanquart and UDEL mechanisms are kept. UDEL has 911 reactions and 70 species, which go up to benzene. On the other hand, Blanquart has 928 reactions and 148 species, describing the formation of higher aromatic rings up to cyclopentapyrene. In view of their future combination with a soot model, further tests are performed to ascer-

tain their capabilities in predicting soot precursors concentrations. Two species are tracked: acetylene and benzene. A low-pressure,  $C_2H_4/O_2$  rich laminar premixed flame stabilised over porous burner from Bhargava [13] was computed. Conductive and radiative losses to the burner are responsible for the stabilization of this kind of flames, and are difficult to model. For that reason, and in order to focus on the chemistry, computations with an imposed T profile (from the experiment) are performed. Figures 3.4 and 3.5 show the computed  $C_2H_2$  and  $A_1$  profiles obtained with the UDEL mechanism for the resolved and the imposed temperature profiles cases. The agreement between experiment and simulation is reasonable. Imposing the temperature has a limited effect on the  $C_2H_2$  concentration profiles, for which the shape of the profile is well recovered but the peak is not well situated. For  $A_1$ , imposing the correct T greatly improves the prediction, indicating that chemistry is sufficiently accurate. Again, the shape is recovered, although the location and height of the peak are underestimated. However, semi-empirical soot models require orders of magnitude only, and the above results are considered reasonable in a first step.

In light of the results, the UDEL mechanism is selected as the best candidate for our purposes. The predictive performance of UDEL for soot precursors is comparable to that of Blanquart, but at a much lower computational cost. Furthermore, its combination with a semi-empirical soot model will demand a re-adjustment of the constants values anyway.

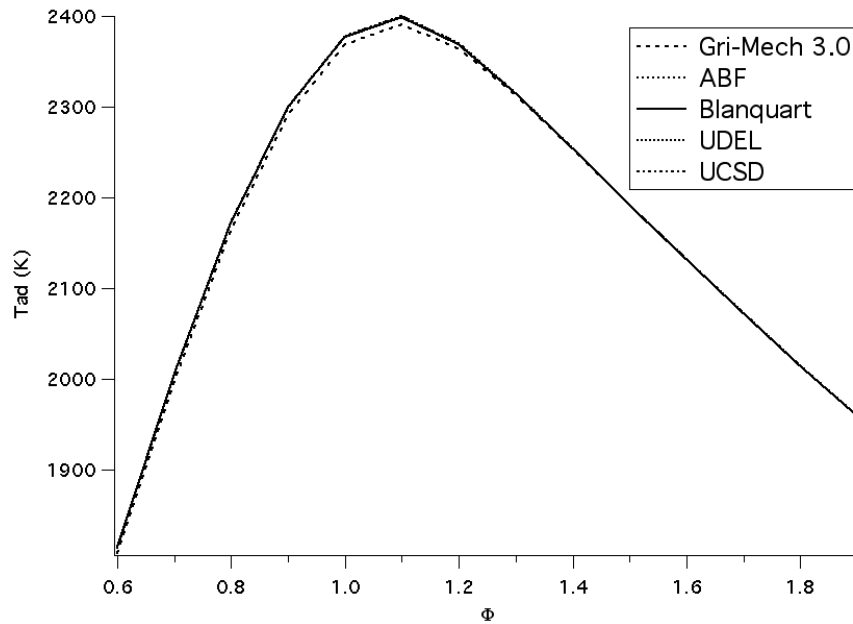


**Figure 3.2:** Adiabatic flame temperature of a freely-propagating laminar ethylene/air 1D flame computed with different chemical mechanisms.

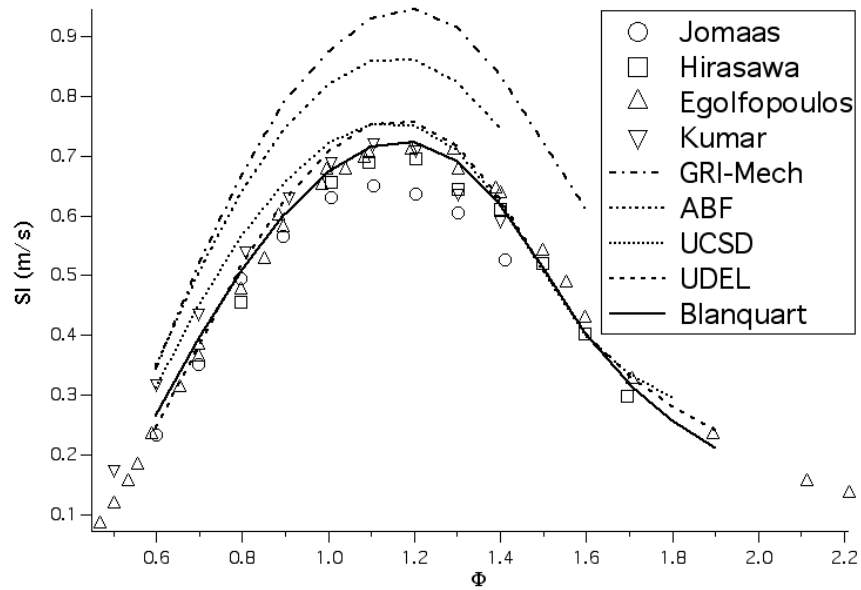


**Figure 3.3:** Laminar flame speed of a freely-propagating ethylene/air 1D flame computed with different chemical mechanisms (lines) and experimental measurements (symbols).

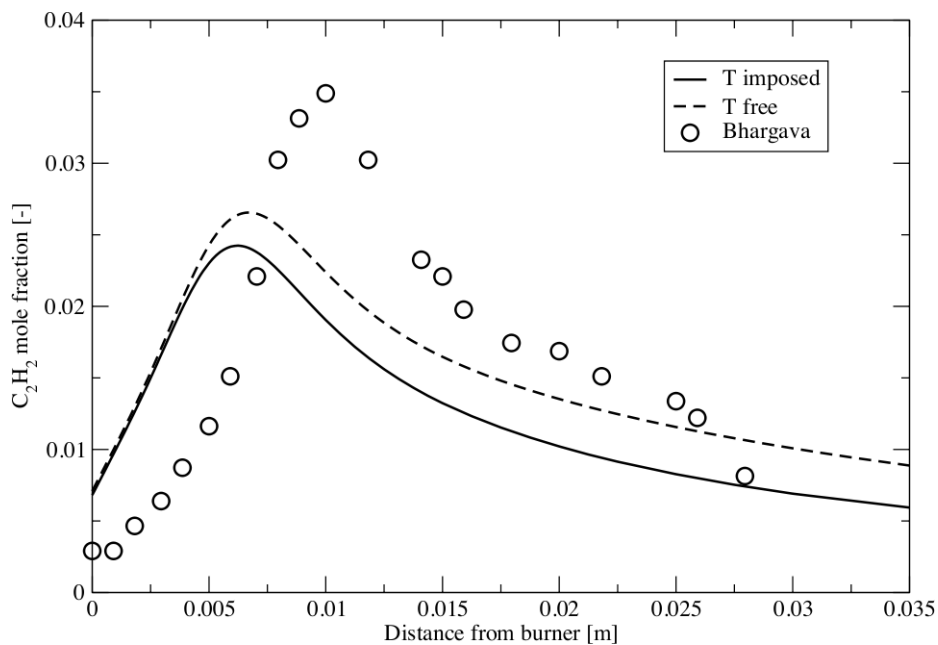


**Figure 3.4:** Comparison between experimental and computed  $C_2H_2$  profiles using UDEL mechanism in the Bhargava flame.

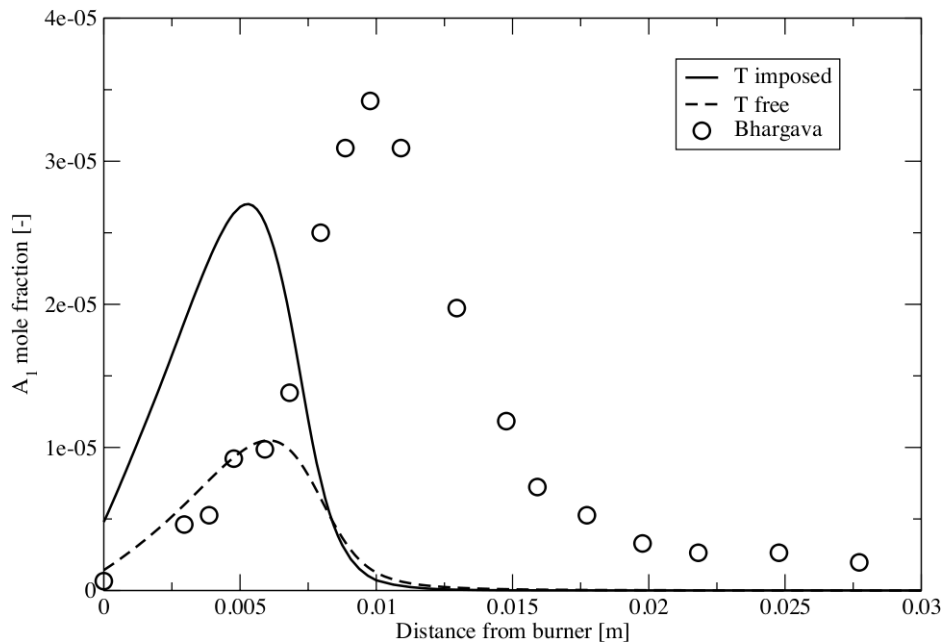


**Figure 3.5:** Comparison between experimental and computed  $A_1$  profiles using UDEL mechanism in the Bhargava flame.

2. A numerical code, *CAN2SOOT*, was built (see Appendix A) allowing to solve the soot variables transport equations in one-dimensional premixed and counterflow diffusion flames on non-uniform meshes. A first order finite differences spatial discretization was used. The steady-state solution is obtained integrating the equivalent pseudo-transient problem with a first order (Euler's method) temporal scheme until convergence is reached. Temperature, velocity, density and chemical species profiles used for the computation correspond to a flame solution given by *CANTERA* and soot is calculated at a post-processing stage. This implies that soot has no effect on the flame structure, as there is no feedback in the flame calculation. This hypothesis of one-way interaction is usually adopted in the literature [96].
  
3. In the cases where radiation is considered, the discrete ordinates method DOM code *PRISSMA*<sup>1</sup> [3, 118, 119] is used. *PRISSMA* tackles the problem of long distance thermal exchanges by solving the radiative transfer equation (RTE), where both emission and absorption of radiation are taken into account. Radiative exchanges within flames are important, particularly in the presence of soot, due to its strong radiative emission and absorption properties. Soot is expected to have a large impact on the radiative balance, therefore radiation must be taken into account when computing soot. Only  $H_2O$ ,  $CO_2$ ,  $CO$  and soot are considered as radiative species and the detailed spectral model SNBcK [60] is used. An expression for the spectral absorption coefficient of soot was taken from Liu *et al.* [95]. The effect of radiation on the flame structure and soot formation will be assessed by performing simulations with and without radiation.

When radiation is included in the computations the three numerical tools *CANTERA*, *CAN2SOOT* and *PRISSMA* are used sequentially as shown in Fig. 3.6 to compute the flame structure, the soot volume fraction profiles and the radiative source term respectively. The 1D solution is interpolated into a 2D mesh which is then extruded to produce a rectangular 3D solution compatible with the radiative solver. *PRISSMA* calculates the radiative source term ( $S_r$ ), which expresses the net volumetric energy gain due to the balance between the emitted and the absorbed radiation per unit of time. Appropriate boundary conditions are used for the calculation of radiation: perfectly absorbing boundary conditions at  $T=300$  K are imposed at the fuel and oxidiser inlet planes whereas pseudo-periodic (reflecting) boundary conditions are set on the four planes corresponding to the burnt gases outflow, as sketched in Fig. 3.7.

---

1. <http://www.cerfacs.fr/prissma/>

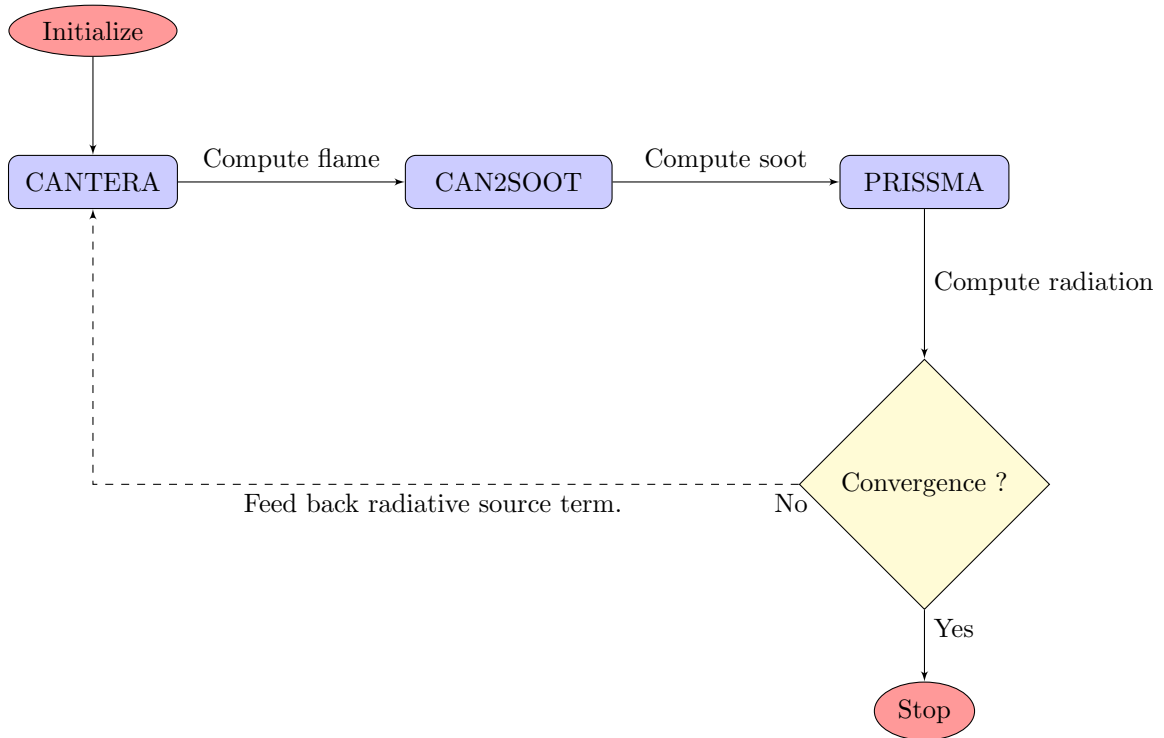


**Figure 3.6:** Flow chart of the solution procedure for soot/gas/radiation coupled simulations.

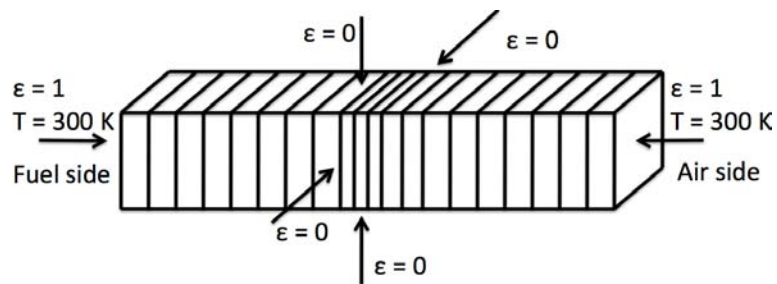


**Figure 3.7:** Sketch of the 3D computational domain and the boundary conditions used for the computation of radiation with *PRISSMA*, where  $\epsilon$  refers to the emission coefficient at the boundaries.

The calculated  $S_r$  term along the central axis is then fed back to *CANTERA* and plugged in the energy equation to account for the volumetric power gain/loss. This sequence is repeated until convergence of the solution is attained, in this case when the relative change in soot volume fraction peak is lower than  $10^{-5}$ , as proposed by Liu *et al.* [95]. This procedure leads to a fully gas phase/soot/radiation coupled solution. Note that the soot feedback on the flame structure is only due to radiative losses, no direct effect of soot formation on the species profiles is accounted for in the model.

# Chapter 4

## Test cases

Industrial combustion systems such as gas turbine combustors present a wide variety of combustion regimes. Even though perfectly premixed systems are preferred for their efficiency and low pollutants emissions characteristics, security reasons impose the use of the so-called technically premixed systems. In these systems, fuel/air mixing takes place upstream of the flame, but the mixing process is not completed before the fresh gases reach the flame front. As a result the fresh gases burn both in premixed and diffusion regimes. Diffusion flames can also be explicitly found in these systems, such as the pilot flames to ensure the ignition of the reactants.

Accurate predictions of soot concentration within such systems demand soot models capable of describing soot formation in premixed, partially-premixed and diffusion flames. However, most of the existing soot formation models rely on semi-empirical findings rather than detailed chemical mechanisms. They were built to reproduce experimental results for particular flames (either diffusion or premixed), and the adaptation of such models to both regimes is not straightforward.

Leung's model was originally adjusted to reproduce experimental results on ethylene/air counterflow diffusion flames. Here, it is tested on different sets of well-characterised laminar diffusion and premixed flames to assess its performance for different regimes. The flames studied are:

- **Diffusion flames:** Several laminar ethylene/oxygen/nitrogen counterflow diffusion flames with varying oxygen content in the oxidiser stream were computed. This set of flames was reported by Hwang & Chung [67], who measured profiles of soot volume fraction. These flames were also studied by Vandsburger *et al.* [150]. Opposed streams of ethylene/nitrogen and oxygen/nitrogen mixtures are supplied through circular nozzles at a constant velocity of 19.5 cm/s. Two kinds of flames are studied:

The first one are referred to as soot formation (SF) flames. The flame lies

on the oxidizer side, where soot particles are formed. These particles are convected away towards the central plane and evacuated without being oxidized. Three flames of this kind are reported with varying oxygen content in the oxidizer stream  $X_{O,o}$ , which takes values of 0.2, 0.24 and 0.28. The fuel stream is composed of pure ethylene.

On the other hand, in the so-called soot formation/oxidation (SFO) flames the flame appears on the fuel side. Particles formed in this region are then convected towards a high oxygen content region at high temperature, where they are completely oxidized. Oxygen mole fraction in the oxidizer stream is  $X_{O,o} = 0.9$  and the fuel mole fraction in the fuel stream  $X_{F,f}$  takes values of 0.23, 0.25 and 0.28.

The kind of flame obtained (SF or SFO) depends on the concentrations of fuel and oxygen. The characteristics of each flame are summarized in Table 4.1:

	SF_0.2	SF_0.24	SF_0.28	SFO_0.23	SFO_0.25	SFO_0.28
$X_{F,f}$	1	1	1	<b>0.23</b>	<b>0.25</b>	<b>0.28</b>
$X_{O,o}$	<b>0.2</b>	<b>0.24</b>	<b>0.28</b>	0.9	0.9	0.9

**Table 4.1:** Summary of the Hwang & Chung flames parameters.  $X_{F,f}$  and  $X_{O,o}$  indicate the mole fractions of fuel and oxygen in the fuel and oxidizer streams respectively.

- **Premixed flames:** The premixed flames studied here for soot computations correspond to a set of rich ethylene/air laminar premixed flames stabilised over porous burner. These flames were investigated by Xu *et al.* [154], where measurements of temperature, chemical species, soot volume fractions, soot surface area, soot formation rates etc. were reported. Three different flames were selected, their inlet equivalence ratio ranging between 2.34 and 2.94 ( $C/O$  ratio takes values of 0.78, 0.88 and 0.98).

## 4.1 Non-radiative cases

In this section, computations are described where radiation was not taken into account. *CANTERA* and *CAN2SOOT* were used sequentially. The former was used to compute the flame structure whereas the latter was used to compute soot in a post-processing stage. This implies that no feedback of soot on the flame structure was accounted for, neither through the consumption of chemical species nor through the effect of soot-driven radiative losses.

### 4.1.1 Non-premixed flames

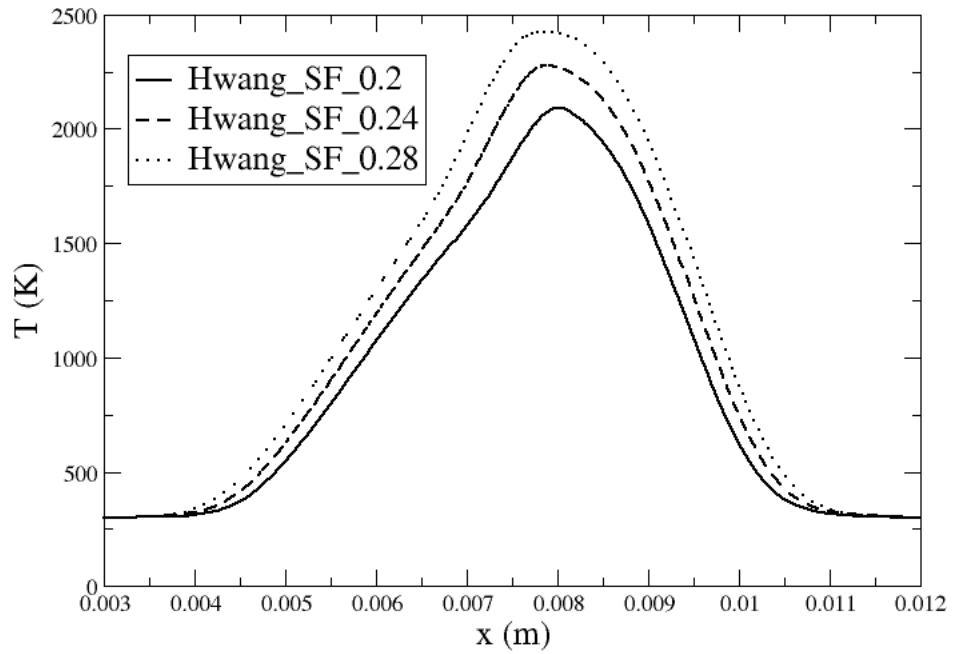
Figure 4.1 shows the calculated temperature  $T$ , and acetylene mole fraction  $X_{C_2H_2}$ , corresponding to the SF flames. As the oxygen content in the oxidiser stream is increased the peak values of  $T$  and  $X_{C_2H_2}$  increase too.

Figure 4.2 shows the computed soot volume fraction profiles ( $f_v = \rho Y_s / \rho_s$ ) in the three SF flames from Hwang & Chung as well as their measurements and those of Vandsburger. The agreement between measurements and computation is reasonable. The profiles shapes are well predicted, although the computed soot peak values are underpredicted by a factor of 2 with respect to the experiments in the SF\_0.24 and SF\_0.28 flames. This result is ascribed to the fact that the chemical mechanism used throughout this work is not the same one used by Leung *et al.*, based on which the model constants were fixed. However, the trend of increase with increasing flame temperature and acetylene concentration is well captured by the model.

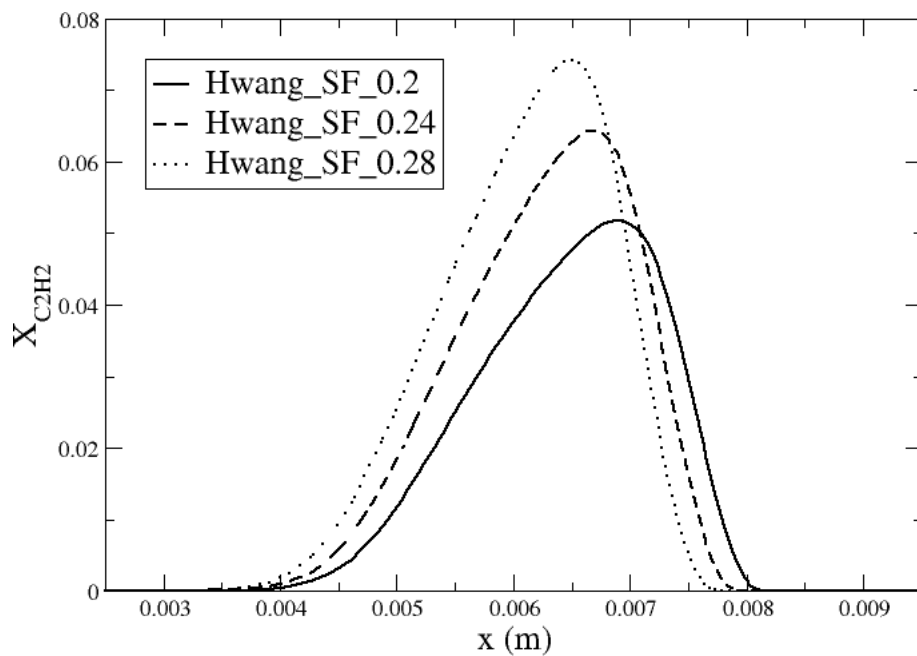
To evaluate the effect of soot oxidation on the soot predictions an additional oxidation term by  $OH$  as proposed by Liu *et al.* [94] is included in the original model. Soot profiles are again calculated in the SF flames from Hwang & Chung and the results are shown in Fig. 4.3. Predicted peak values of soot volume fraction decrease about 10% for the SF\_0.28 flame with respect to the computation with oxidation only due to  $O_2$ . This difference would be more important if the predicted soot levels were higher. The effect of the  $OH$  oxidation is lower for flames with lower oxygen index, as less soot is produced.

Figure 4.4 shows the calculated temperature  $T$ , and acetylene mole fraction  $X_{C_2H_2}$ , corresponding to the SFO flames. There is a slight increase in temperature and also an increase in the acetylene concentration peak as the oxygen content in the oxidiser stream increases.

Fig. 4.5 shows a comparison between the experimental measurements of Hwang & Chung and the computed soot volume fraction, using both the original Leung's model and the one with the additional oxidation term by  $OH$ . Peak values are overpredicted by a factor of 3. Also, the computed  $f_v$  profiles seem to be shifted 0.5 mm towards the oxidiser stream, which is the direct consequence of the computed acetylene profiles being also shifted by the same distance, with respect to the computations performed by Hwang & Chung. As a result of the  $C_2H_2$  profile being shifted, now soot is being formed in a higher temperature region, as temperature grows in the region  $x < 6mm$ , which explains the overprediction of soot volume fractions. The effect of soot oxidation is more important than in the SF flames, as the  $f_v$  peak values decrease by 40% when the oxidation by the  $OH$  radical is plugged.



(a)



(b)

**Figure 4.1:** Calculated profiles corresponding to the SF counterflow diffusion flames from Hwang & Chung. (a) Temperature. (b) Acetylene mole fraction.

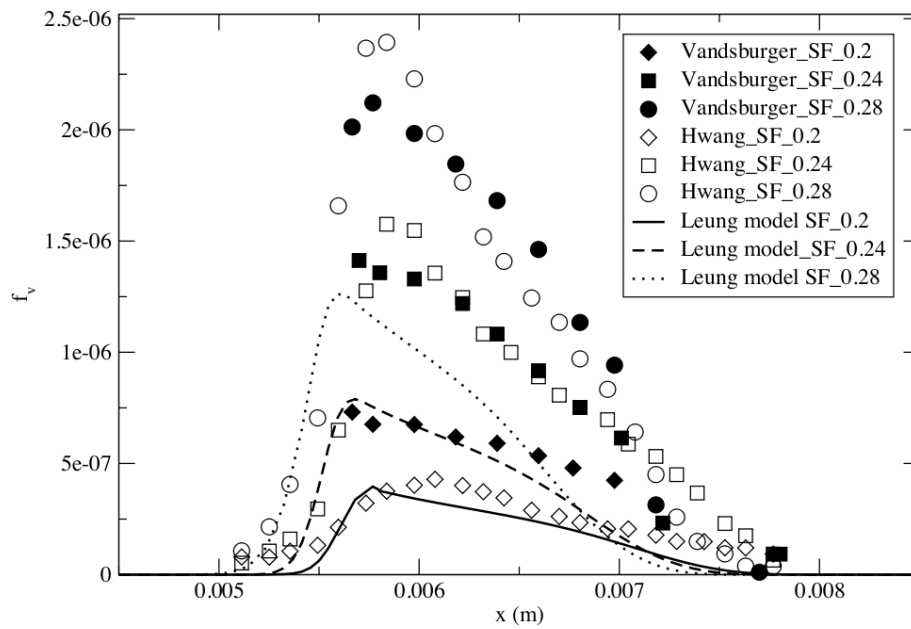


**Figure 4.2:** Comparison between measured and computed soot volume fractions on the SF flames from Hwang & Chung.

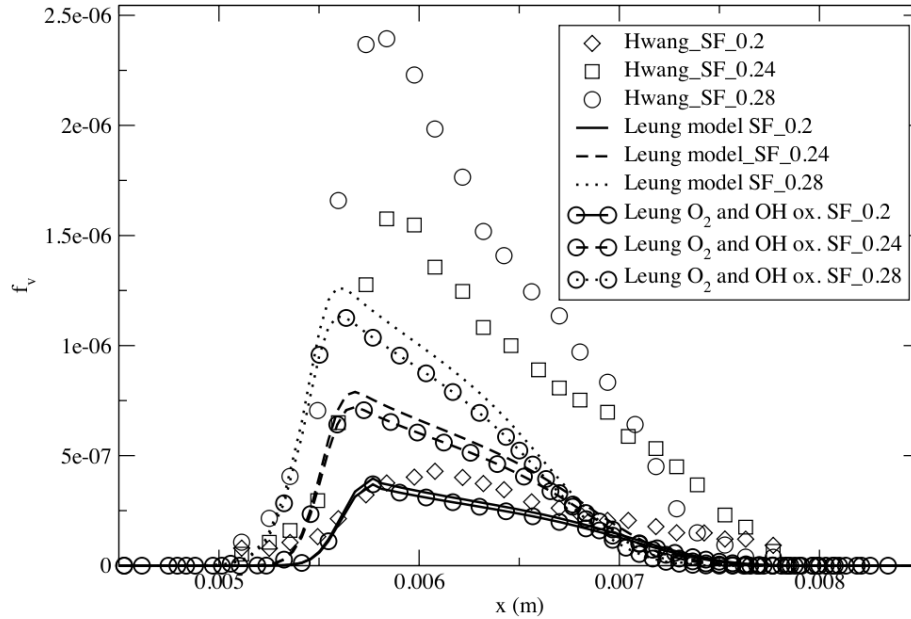
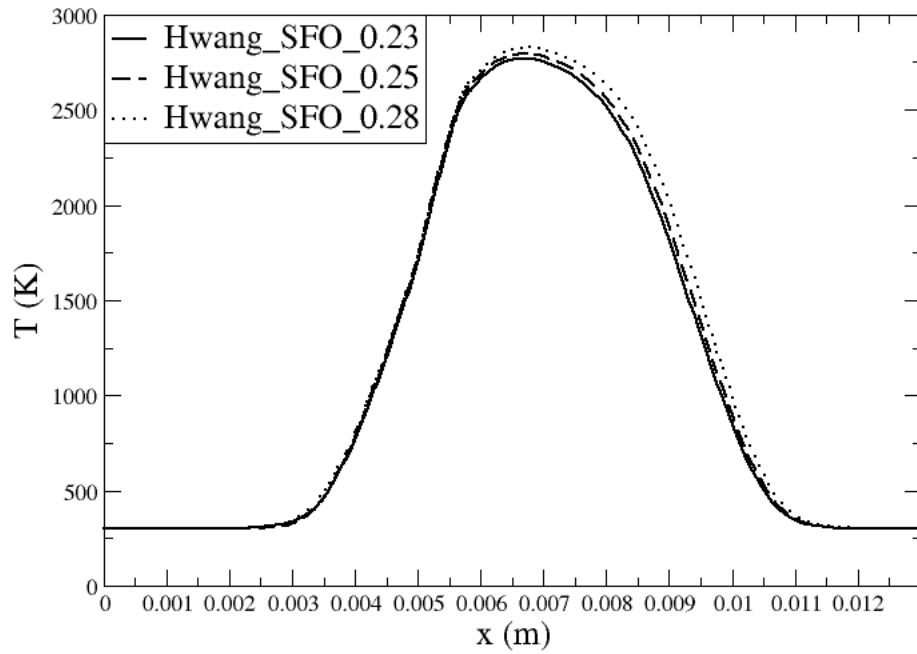
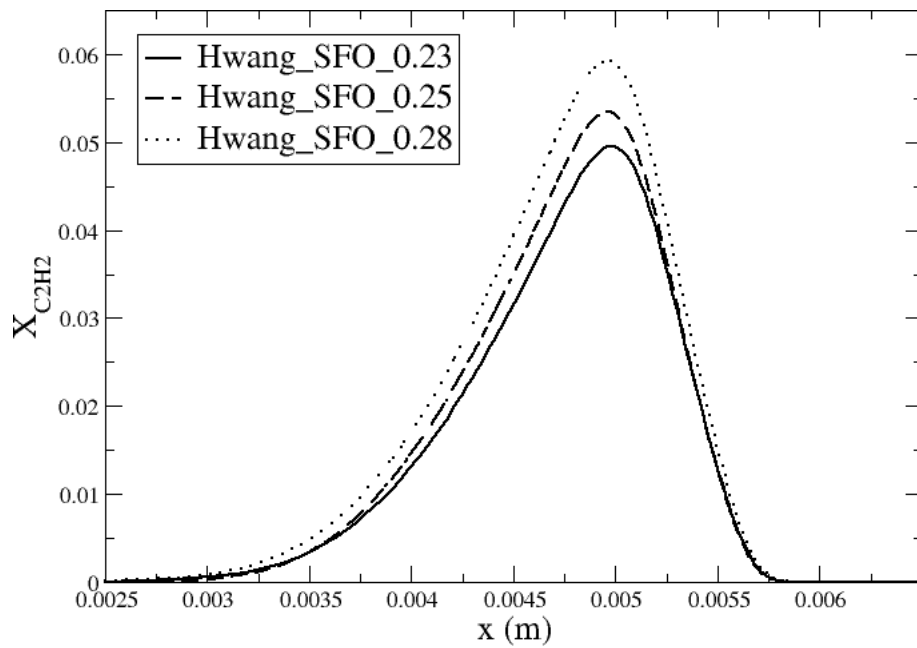


**Figure 4.3:** Comparison between measured and computed soot volume fractions on the SF flames from Hwang & Chung with soot oxidation by  $O_2$  only and with soot oxidation both by  $O_2$  and  $OH$ .



(a)



(b)

**Figure 4.4:** Calculated profiles corresponding to the SFO counterflow diffusion flames from Hwang & Chung. (a) Temperature. (b) Acetylene mole fraction.

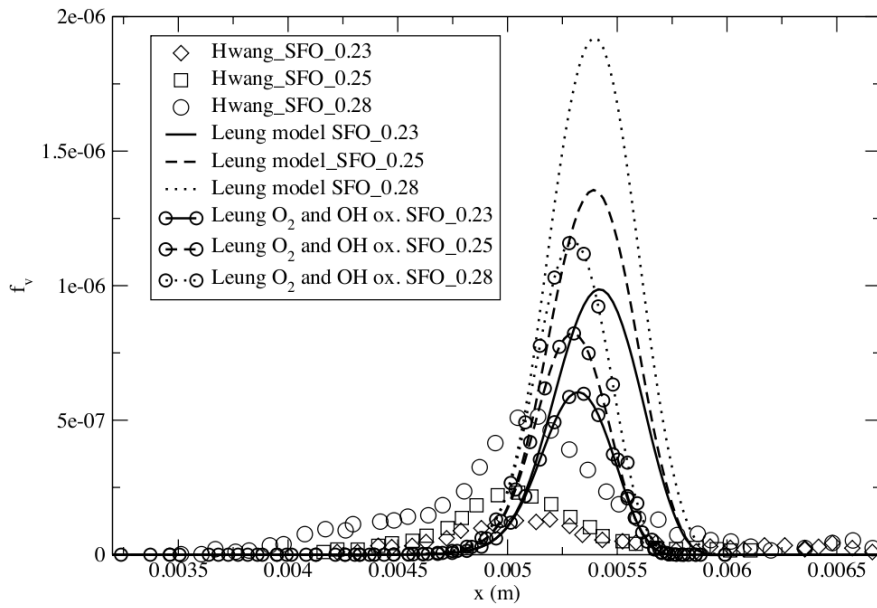


**Figure 4.5:** Comparison between measured and computed soot volume fractions in the SFO flames from Hwang & Chung.

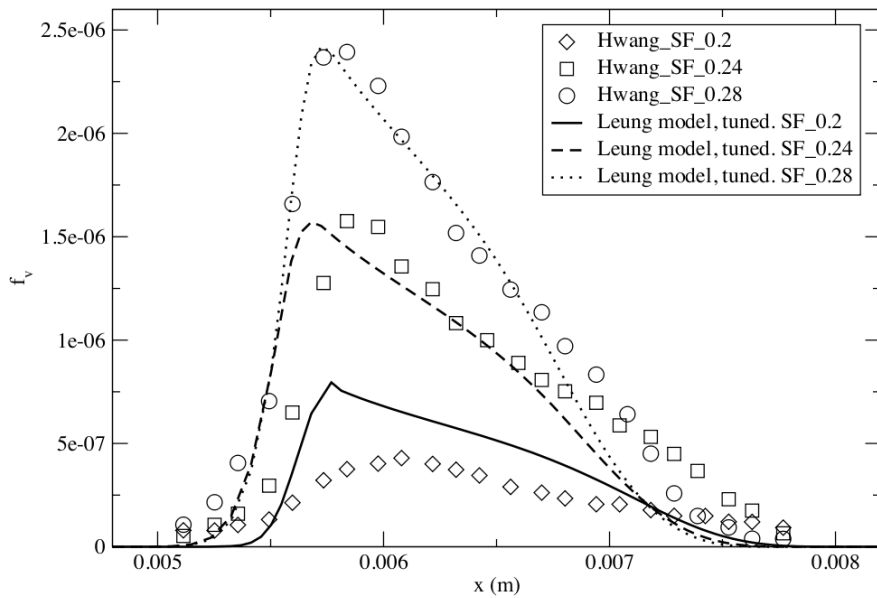


**Figure 4.6:** Computed soot volume fraction profiles in the Hwang & Chung SF flames using Leung's adjusted soot model.

Calculations corresponding to the three Hwang & Chung flames were performed where, in order to retrieve the experimental soot levels, a modification in the surface growth term pre-exponential constant is proposed. The constant has been adjusted so as to retrieve the soot volume fraction peak value in the SF\_0.28 flame including oxidation by both  $O_2$  and  $OH$  and it takes a value of  $A_2 = 1.04 \cdot 10^4$ . Results of the computations with the adjusted constant value are shown in Fig. 4.6. The fitted value of  $A_2$  leads also to fairly good predictions of  $f_v$  in the SF\_0.24 flame. Nonetheless, soot is overpredicted in the SF\_0.2 flame. This disagreement has been reported previously [95], where it is suggested that the experimental values corresponding to the SF\_0.2 flame should be taken with caution.

### 4.1.2 Premixed flames

#### First results

The laminar ethylene/air rich premixed flames from Xu *et al.* [154] were computed. As commonly done when computing burner stabilised flames [154], the experimental temperature profiles were imposed in the calculations to account for the heat losses due to conduction and radiation, and are shown in Fig. 4.7. Figure 4.8 shows the computed and experimentally measured  $C_2H_2$  mole fraction profiles for these flames: the agreement between computations and experiments is satisfactory. Acetylene concentration reaches a peak at the reaction region and then stabilizes at a somewhat lower value. The remaining acetylene downstream of the flame fronts is a consequence of the high equivalence ratio of the flames, which leads to an incomplete combustion. More acetylene is produced for rich flames.

Computed soot profiles corresponding to these flames are compared in Fig. 4.9 to measured soot volume fractions. It is seen that  $f_v$  grows continuously throughout the flame, which is in agreement with the experiment (at least in the region studied). As in the experiment, richer flames yield more soot. However, the soot levels are highly overpredicted in the burnt gases region.

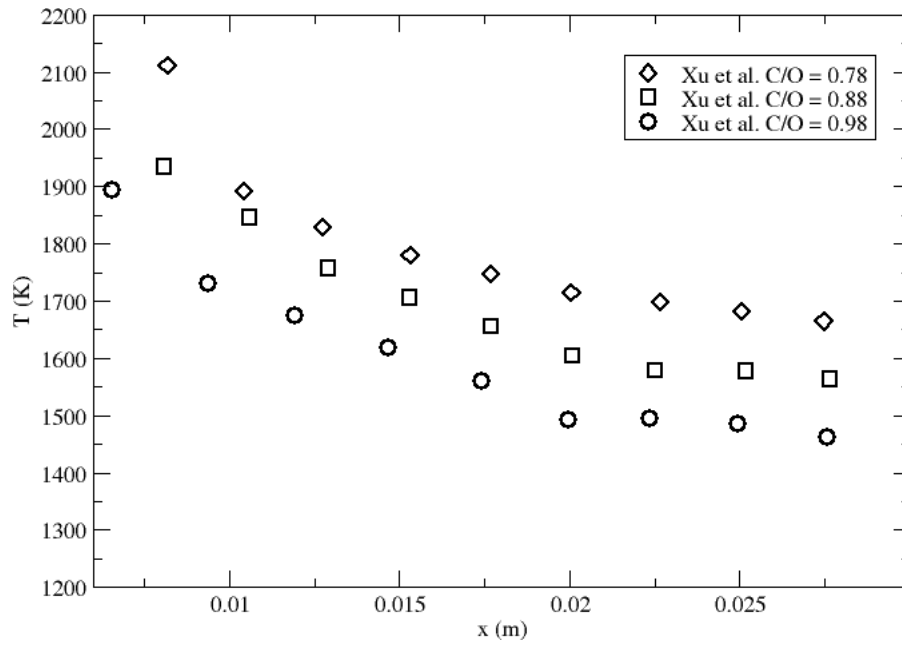


**Figure 4.7:** Experimental temperature profiles in the ethylene/air premixed flames from Xu *et al.* imposed in the computations.

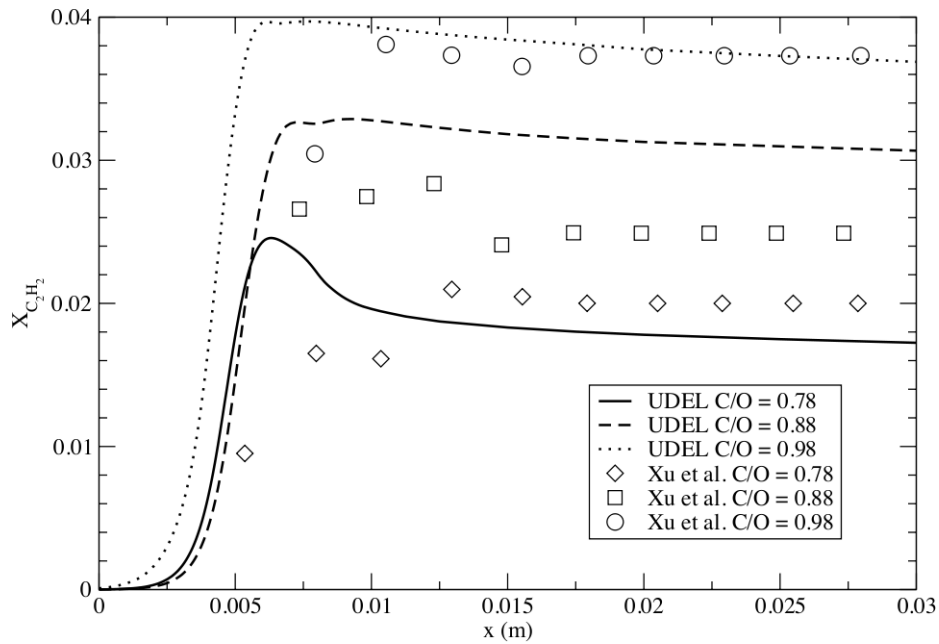


**Figure 4.8:** Comparison between measured and computed acetylene mole fractions on the premixed flames from Xu *et al.*

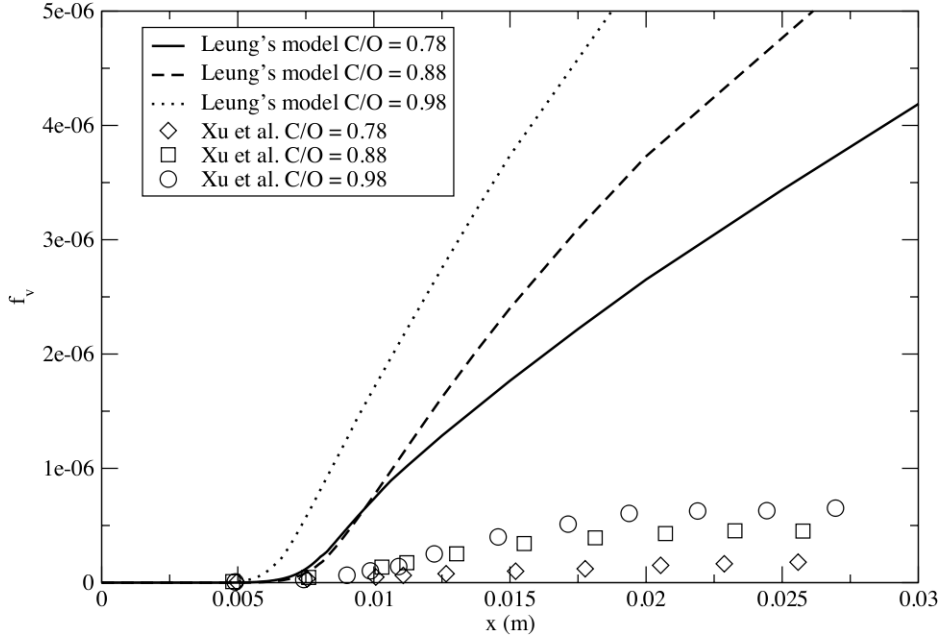


**Figure 4.9:** Comparison between measured and computed soot volume fractions on the ethylene/air premixed flames from Xu *et al.*

### Analysis

In order to understand the overestimations mentioned above, some quantities are watched closely for the flame  $C/O=0.78$ . The good agreement between the computed and the measured soot surface growth rate per unit soot surface area is noticeable (Fig. 4.10), since the surface growth term per unit soot surface area in the model only depends on the acetylene mole fraction and the temperature and, as already mentioned,  $X_{C_2H_2}$  is well predicted and the temperature profile is the one from the experiment.

Even though soot surface growth rate per unit soot surface area is well predicted, the soot surface area itself is overpredicted, as shown in Fig. 4.11. This leads to a larger surface growth term than in the experiment, which explains the high soot levels obtained in the computation. This disagreement seems then to come from the prediction of the soot surface area,  $S$ , calculated as:

$$S = \left( \frac{36\pi}{\rho_s^2} \right)^{1/3} (\rho n)^{1/3} (\rho Y_s)^{2/3} \quad (4.1)$$

According to Eq. (4.1), the soot surface area depends both on the soot mass fraction and the number of particles density. Fig. 4.12 shows the computed and measured soot particle number density, which is overpredicted in the region

$x < 15\text{mm}$ . Beyond that point, the predictions are fairly reasonable. This may explain the overprediction in soot surface area in the first half of the domain. This initial overprediction of  $S$  leads to a larger soot surface growth term, leading to higher soot mass fractions with respect to the experiment and hence to the subsequent overprediction of soot surface area through Eq. (4.1).

Soot particles aging (see Section 3.1) is not properly accounted for in Leung's model. This is the reason why large soot yields were found in the premixed flames studied. Further studies are carried out dealing with this phenomenon and its modeling in the next section.

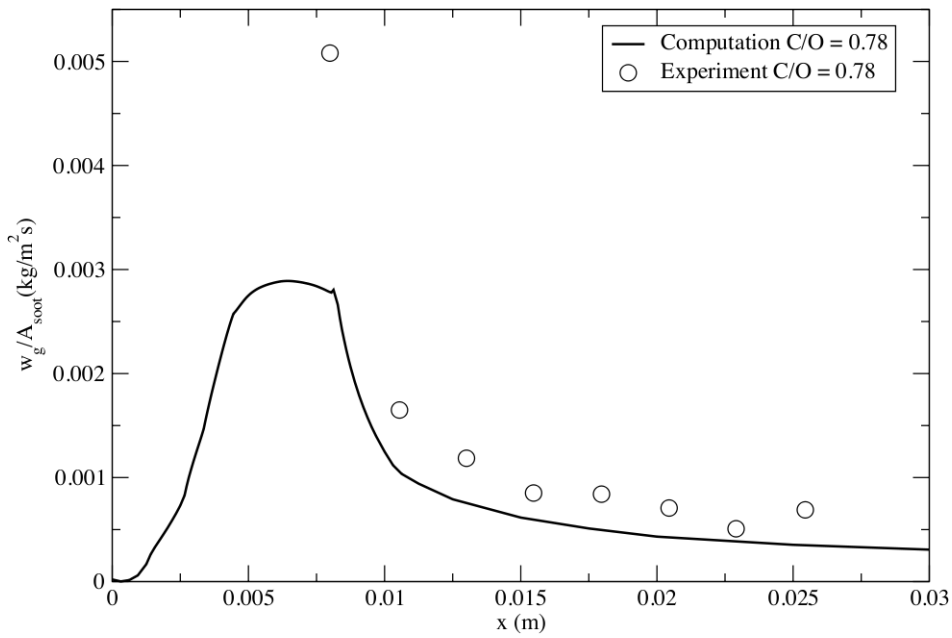


**Figure 4.10:** Comparison between measured and computed soot surface growth rate per unit soot surface area on the  $C/O = 0.78$  ethylene/air premixed flame from Xu *et al.*

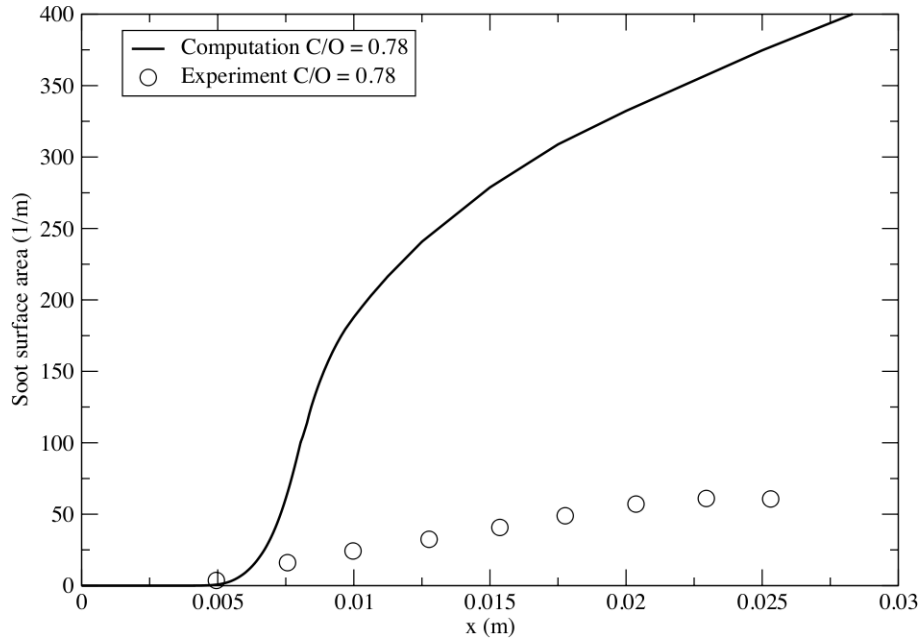


**Figure 4.11:** Comparison between measured and computed soot surface area on the  $C/O = 0.78$  ethylene/air premixed flame from Xu *et al.*

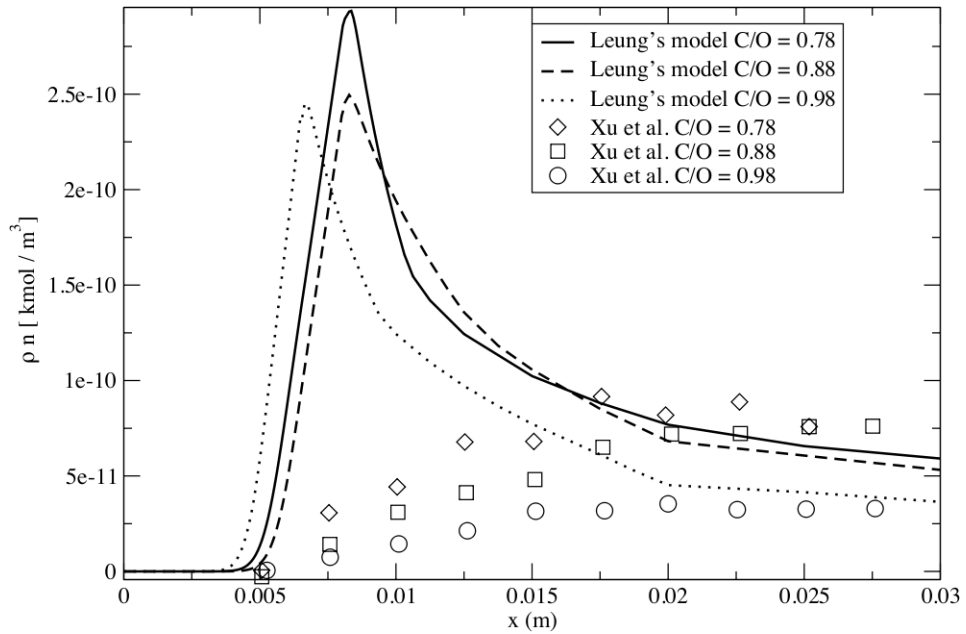


**Figure 4.12:** Comparison between measured and computed soot particle number density  $\rho n/N_A$  on the ethylene/air premixed flames from Xu *et al.*

### Surface growth model

Soot formation is dominated by surface growth. In this sense, a model that takes this phenomenon into account correctly is essential to describe soot formation in premixed flames. As shown in Fig. 4.9, Leung's simple model based on the acetylene mass fraction is not capable of describing soot surface growth in the burnt gases region. Remaining acetylene along the burnt gases region will, accordingly to Leung's model, lead to a continuous production of soot. In reality, soot is not produced all along the burnt gases region but rather in a short region close to the flame front because, as soot particles travel downstream of the flame front they experience a reduction in reactivity (see Section 3.1).

The soot surface growth term in Leung's model has been replaced by an expression for soot surface growth rate proposed originally by Frenklach & Wang [56], which writes:

$$w_{sg} = \alpha \cdot R \cdot S \quad (4.2)$$

where  $\alpha = (\tanh(8168/T_{max} - 4.157) + 1) / 2$  is a steric factor of order unity,  $T_{max}$  is the maximum flame temperature and the reaction rate  $R$  is written as follows:

$$R = \frac{C_{HACA} k_{1f} k_{3f} [H] [C_2H_2] [C_s - H]}{k_{1b} [H_2] + k_{2f} [H] + k_{3f} [C_2H_2]} \quad (4.3)$$

with  $C_{HACA} = 2M_s/N_A$  and  $[C_s - H] = 2.3 \cdot 10^{19}$  sites/ $m^2$ . Reaction rates coefficients are defined as  $k_i = A_i T^{n_i} \exp(-T_{a_i}/T)$ .

The expression from Eq. (4.3) is issued from a quasi-steady-state analysis of a reduced chemical scheme based on the HACA mechanism, whereby soot growth is not only dependent on the acetylene concentration  $[C_2H_2]$ , but also on the hydrogen radical concentration  $[H]$ . Table 4.2 shows the soot surface growth mechanism as summarized in [154] and originally presented in [74].

Index	Reaction	A(m, kmol, s)	n	$T_a(K)$
1f	$C_s - H + H \rightarrow C_s \cdot + H_2$	$2.5 \cdot 10^5$	—	8046.2
1b	$C_s \cdot + H_2 \rightarrow C_s - H + H$	$3.9 \cdot 10^9$	—	4690.6
2f	$C_s \cdot + H \rightarrow C_s - H$	$1.9 \cdot 10^{11}$	—	0
3f	$C_s \cdot + C_2H_2 \rightarrow C_s - H + H$	$8.4 \cdot 10^8$	0.4	4221.6

**Table 4.2:** Summary of reaction mechanism for soot surface growth (from Kazakov *et al.* [74]).

Figure 4.13 shows a comparison between experimental and computed soot volume fraction profiles on Xu *et al.* flames with the new surface growth term. The results are qualitatively satisfactory in the sense that soot grows in the region close to the injector and it reaches a plateau far downstream, as observed in

the experiments. This is explained by the shape of the surface growth reaction rate  $R$  profiles, shown in Fig. 4.14. A peak is attained near the flame front, but further growth is inhibited in the burnt gases region due to particle aging. This behaviour is explained in turn by the computed  $H$  radical profiles, shown in Fig. 4.15, decreasing in the downstream burnt gases.

Even though the computed soot yields corresponding to the  $C/O = 0.78$  are quantitatively in agreement with the experiment, soot is underpredicted in the other two flames. Moreover, less soot is produced for richer flames, which is contradictory with the observed tendency where richer flames produce more soot. This is readily explained by the computed surface growth reaction rates in Fig. 4.14, which are decreasingly lower for richer flames. The soot surface growth reaction rate of Eq. (4.3) mirrors the behaviour of the computed  $H$  radical profiles in Fig. 4.15. Variations in  $H$  radical mole fractions being proportional to temperature,  $H$  mole fractions are largest for lower  $C/O$  ratios, where larger temperatures are found (see Fig. 4.7).

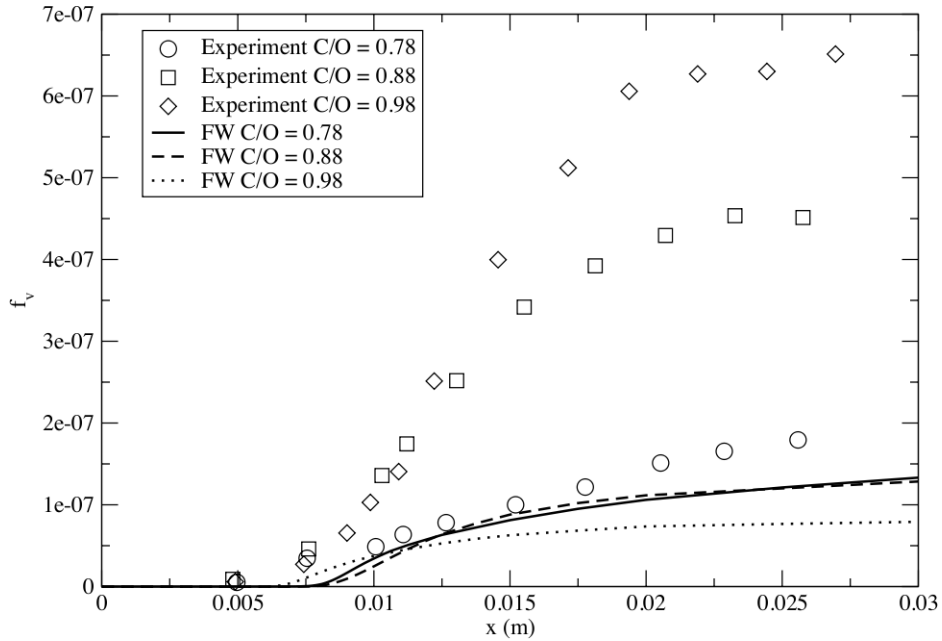


**Figure 4.13:** Comparison between measured and computed soot volume fraction  $f_v$  on the ethylene/air premixed flames from Xu *et al.* using the soot surface growth term by Frenklach *et al.*

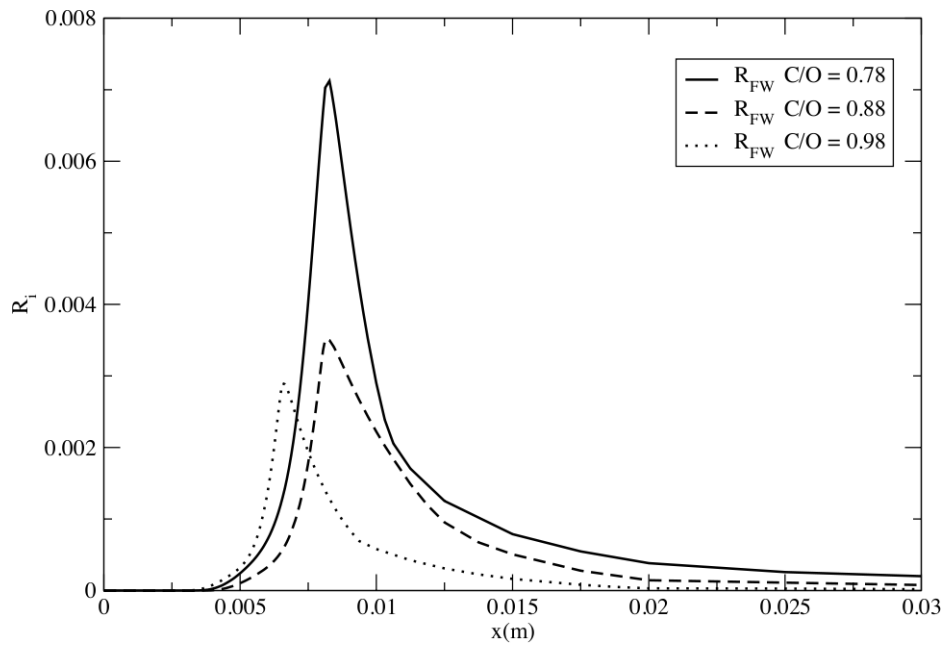


**Figure 4.14:** Computed soot surface growth reaction rates on the ethylene/air premixed flames from Xu *et al.* using expression by Frenklach *et al.*

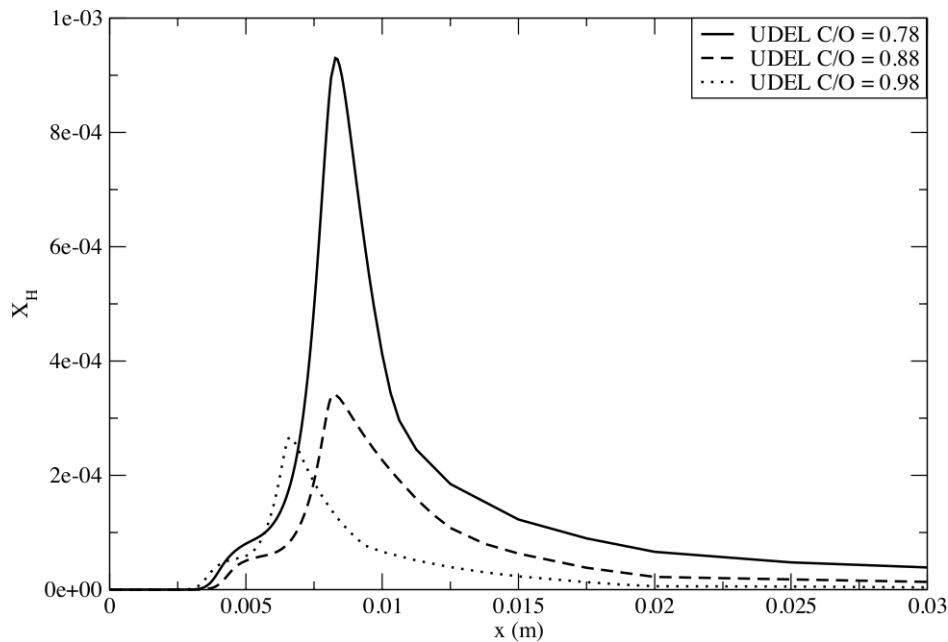


**Figure 4.15:** Computed  $H$  radical mole fractions using UDEL mechanism on the ethylene/air premixed flames from Xu *et al.*

To keep the correct dependence of soot with equivalence ratio, another attempt to improve the model is proposed. Leung's original surface growth term is retrieved, where the value of the surface growth term pre-exponential constant  $A_2$  is adjusted to match the experimental data.

Fig. 4.16 shows  $f_v$  profiles corresponding to predictions using different values for  $A_2$  on the  $C/O = 0.78$  flame by Xu *et al.*, along with the experimental profile. It is seen that the original value of  $A_2$  had to be divided by a factor of 6 in order to retrieve the correct soot levels for the computed flame. Using the same adjusted value of the pre-exponential constant for soot surface growth ( $A_2 = 0.1 \cdot 10^4$ ), the three Xu *et al.* flames were computed and results are shown in Fig. 4.17. As expected, the correct sooting dependence with equivalence ratio is recovered. However, soot is still underpredicted, the computations yielding values of  $f_v \sim 50\%$  of the experimental ones. The order of magnitude is correct on the burnt gas region. The fact no plateau is reached and soot continues to increase may be compensated in applied calculations by dilution with cold air. However, further improvements of the model are needed in order to correctly predict soot in burners.

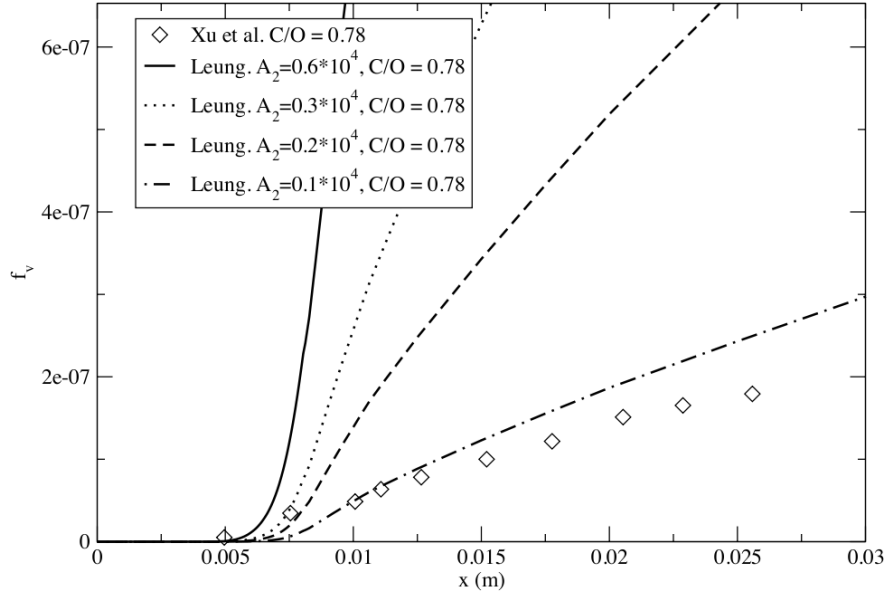


**Figure 4.16:** Experimental and computed soot volume fraction profiles on the  $C/O = 0.78$  ethylene/air premixed flame from Xu *et al.* using Leung's model with modified values of the surface growth term pre-exponential constant  $A_2$ .

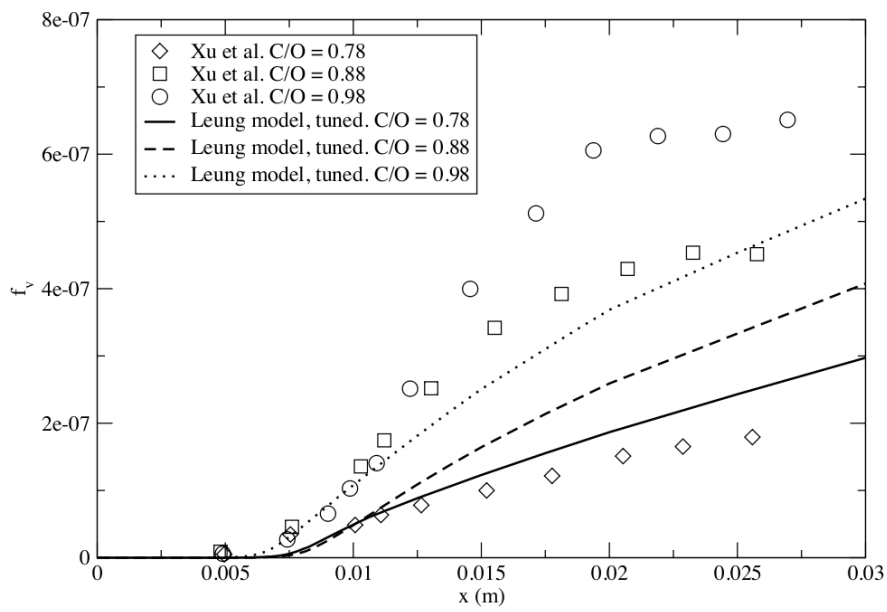


**Figure 4.17:** Experimental and computed soot volume fraction profiles on the ethylene/air premixed flames from Xu *et al.* using Leung's model with and adjusted value of the surface growth term pre-exponential constant  $A_2 = 0.1 \cdot 10^4$ .

## 4.2 Soot/gas/radiation coupling

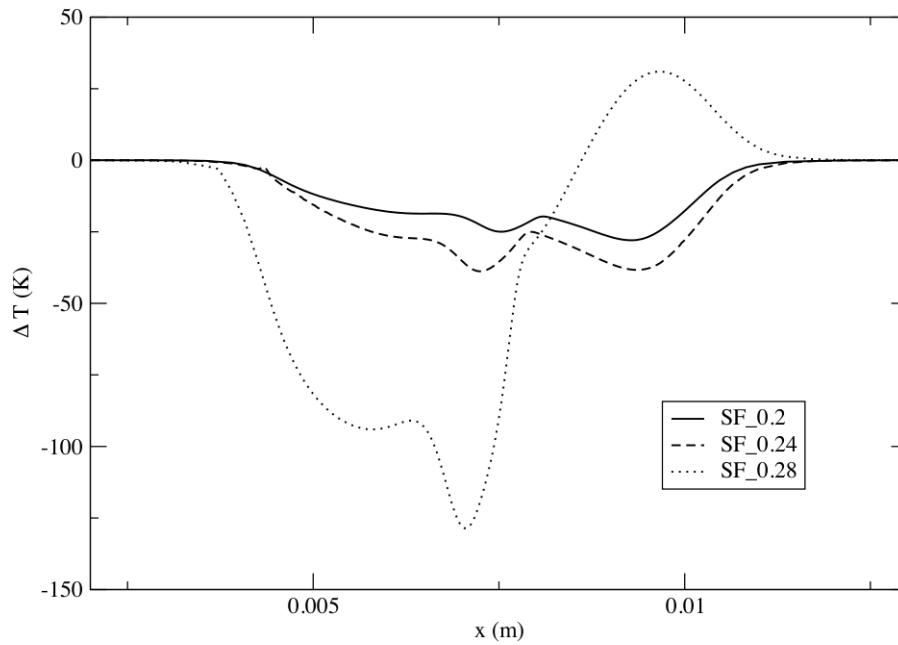
Radiation was included in the computation of the SF flames from Hwang & Chung.

Figure 4.18 shows the computed temperature difference profiles for the Hwang & Chung SF flames with and without radiation ( $\Delta T(x) = T(x)_{rad} - T(x)_{no.rad}$ ). When gas and soot radiation contributions are included in the calculation, temperature drops of up to 20K, 25K and 120K in the SF\_0.2, SF\_0.24 and SF\_0.28 flames respectively are observed. The flames peak temperature drops by  $\approx 1\%$  of their values. The temperature difference is higher in the sooting region due to the higher radiative losses induced by soot. Also, it is observed that there is a slight local temperature increase for the SF\_0.28 flame due to radiation absorption. The impact of radiation in these flames is not very important due to their reduced size. However, this effect may increase significantly in larger systems.

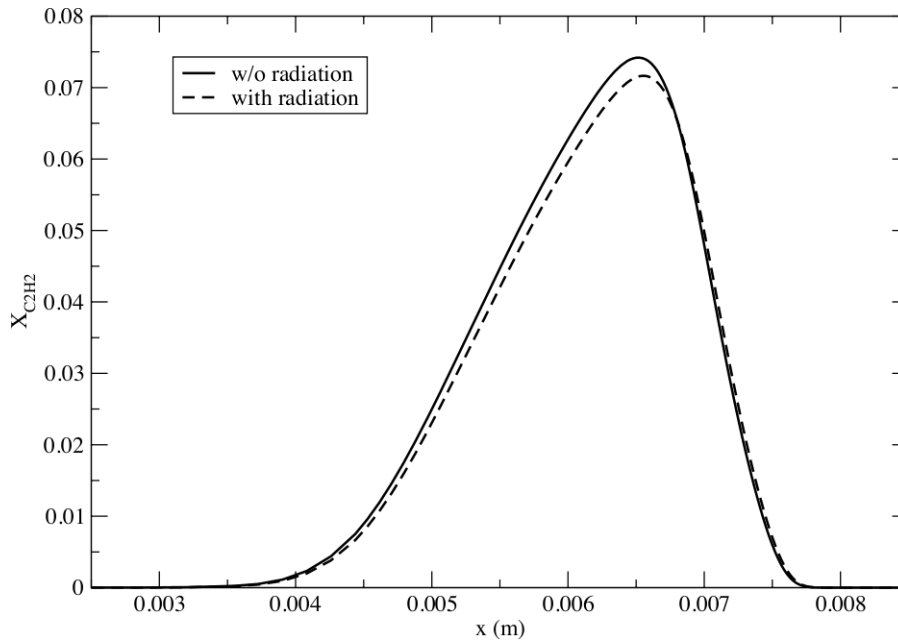
Figure 4.20 shows the computed  $S_r$  profiles in the SF\_0.28 flame for three different cases. The first one corresponds to a calculation where no soot was included. The single bump corresponds then to the radiation emitted by the hot gases, mainly due to  $H_2O$ ,  $CO_2$  and  $CO$ . Positive values of  $S_r$  correspond to a power loss of the flame. A second calculation has been performed, in which the soot profile has been computed without closing the loop from Fig. 3.6. This allows to compute the corresponding  $S_r$  profile, where no radiation feedback on the flame is accounted for. In addition to the radiation due to the hot burnt gases, a second bump appears, due to the presence of soot. The third profile shows the  $S_r$  corresponding to the coupled solution procedure. It is observed that the soot-driven radiation bump is decreased. The effect that radiation has on soot is to decrease the amount of soot produced, due to the temperature drop induced by the radiative heat loss.

Figure 4.21 shows the computed soot volume fraction profiles in the SF flames, with and without radiation. As mentioned above, it is observed that when gas and soot radiative losses are introduced, less soot is produced. This effect is more important in more sooting flames. However the difference is minor and does not exceed 6% of the soot volume fraction peak values, far below the uncertainties in both soot measurements and modeling. This is due to the fact these test flames are small and radiation has a small effect for such small volumes of gases. However, in larger systems the effect may increase significantly.

Figure 4.19 shows the computed soot volume fraction profiles in the SF\_0.28 flame, with and without radiation. Radiative losses induce a decrease in the acetylene mole fraction peak of 4% in the SF\_0.28 flame (and even lower in the other two). The decrease in acetylene will also decrease the soot production.



**Figure 4.18:** Computed temperature profiles in the Hwang & Chung SF flames with and without radiation using Leung's adjusted soot model.



**Figure 4.19:** Computed acetylene mole fraction in the Hwang & Chung SF.0.28 flame with and without radiation.

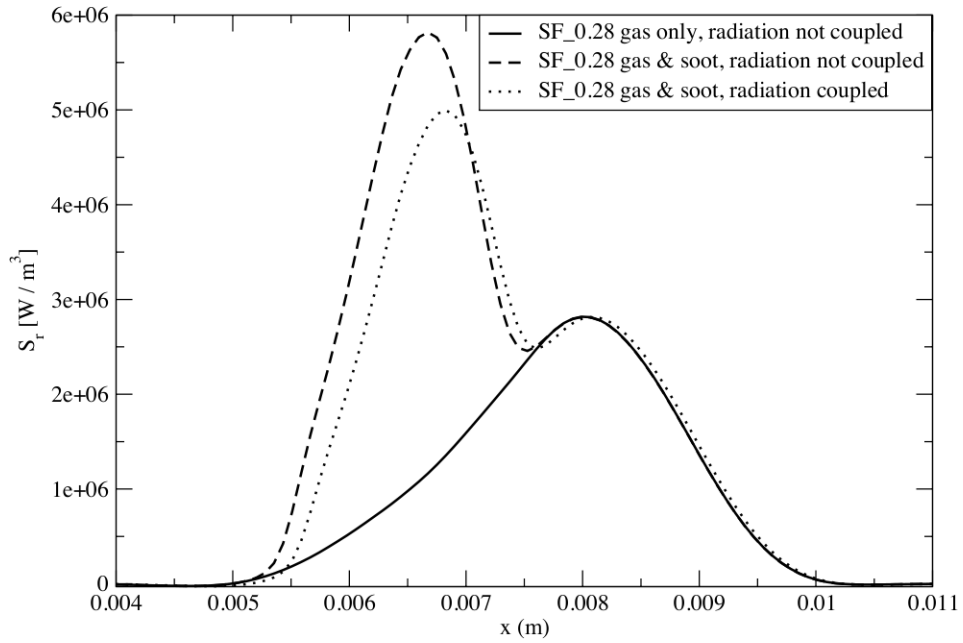


**Figure 4.20:** Computed radiative source term in the Hwang & Chung SF flames with and without soot using Leung's adjusted soot model.

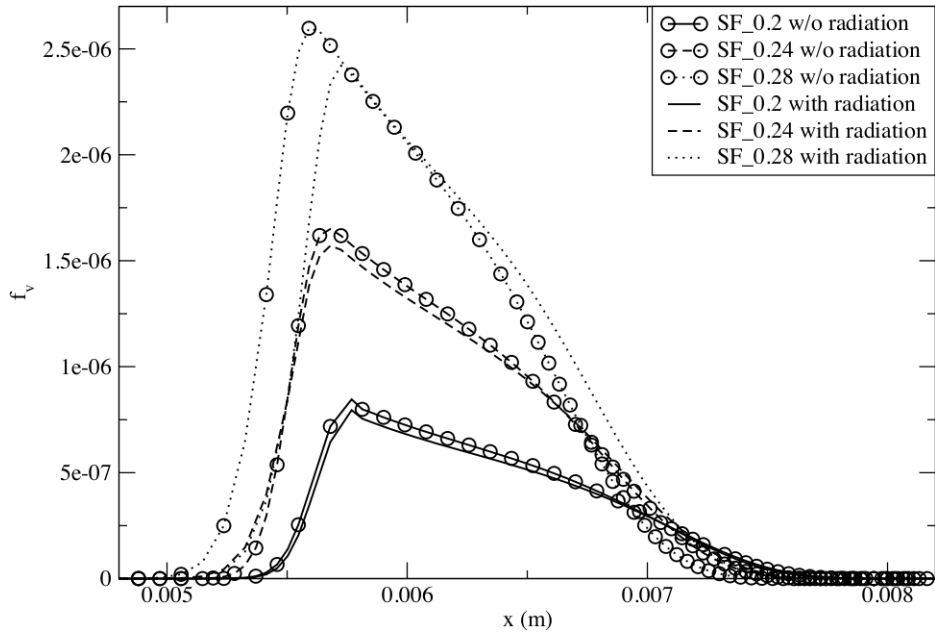


**Figure 4.21:** Computed soot volume fraction profiles in the Hwang & Chung SF flames with and without radiation using Leung's adjusted soot model.

## Chapter 5

# Conclusions and perspectives I

### 5.1 Conclusions on soot modeling

A semi-empirical model for soot was implemented and tested in several ethylene/air laminar counterflow diffusion and premixed flames. Two-way coupling between the gas phase and soot was included, through the inclusion of a radiative source term, accounting for the emission and reabsorption of radiation within the flames. The conclusions of this study are as follows:

1. The original version of Leung's model is capable of predicting the soot formation in counterflow diffusion flames. All the important phenomenology is included: nucleation, agglomeration, surface growth and oxidation.
2. Soot oxidation by  $OH$  is important and must be taken into account if accurate soot yields are to be predicted.
3. In order to predict soot in premixed flames with Leung's model it is necessary, however, to account for the effect of soot particles aging throughout the flames. Alternative expressions are used for the soot surface growth term, which are based on the HACA mechanism. This mechanism was originally developed to explain the surface growth of PAH, but it can also describe the soot surface growth. An expression for the soot surface growth by Frenklach et al. is used, which links the reaction rates to the availability in  $C_2H_2$ ,  $H$  and  $H_2$  species to account for soot particles aging. Reasonable results are found for the less rich flame from Xu et al., however, less soot is predicted for richer flames, contrarily to the experiments. This wrong trend is readily explained by the decreasing  $H$  radical concentration predictions, which diminishes with equivalence ratio.
4. Leung's model is capable of reproducing the correct dependence of soot formation on equivalence ratio. However, particle aging is not correctly

accounted for, leading to overpredictions of soot volume fraction far downstream of the flame. This effect can be in part controlled by the adjustment of the surface growth term pre-exponential constant.

5. Radiative heat losses in the counterflow diffusion flames studied are due to both gas and soot. Radiation-driven heat losses lead to a decrease in flame temperature and, consequently, to a decrease in soot levels. The temperature drops induced by radiative losses in the flames studied are small due to their reduced size.

The conclusions drawn from the present work have implications for the thermal behaviour of industrial burners: the contribution of soot-induced radiation with respect to that due to the gas phase is important and must be accounted for when accurate predictions of the gases temperature or the heat flux to the surroundings are sought. This effect is more important as the size of the system increases, hence soot/radiation predictions would find a good field of application in the flames typically encountered in the petro-chemical [113] or glass industries, spanning up to several meters.

## 5.2 Perspectives

The methodology presented herein allows to perform computations of soot and radiation in one-dimensional premixed and counterflow diffusion flames. The flexibility and modularity of the methodology allows for the testing of a wide range of soot models and chemical mechanisms. A simple soot model was used throughout this work with the idea of a future implementation in a 3D solver for the application of soot predictions in complex geometries of industrial interest. Some ideas are proposed for future studies:

- The utilization of more advanced soot models seems compatible with the presented methodology. In particular, soot formation and growth by PAH's seems interesting, as it is the natural extension to the model used in this work, where acetylene was used as the sole soot precursor. Existing soot models from Di Domenico & Blacha [15, 16, 42] propose a semi-empirical soot model for soot formation and growth based on a sectional approach for the PAH's, which could be easily implemented in the present methodology.
- Complex soot formation models [23] are also compatible with this methodology, although more detailed chemical mechanisms would be needed.
- The validation of a soot model on academic one-dimensional flames was a first step towards the passage to more complex configurations. Once a soot model has shown to yield good predictions of soot in such simple cases, and to reproduce well the dependence on parameters such as pressure or equivalence ratio, the next step would be its implementation on a 3D

solver for its application on complex geometries. Usually, reduced chemical mechanisms are used in such solvers, thus the chemical species needed by the soot model are not directly accessible by the code. Tabulated chemistry seems to be a good approach to address this issue. As a matter of fact, attempts have been made in this sense, the soot model was implemented in a LES solver to predict soot formation in an industrial burner [84]. However, the prediction of soot in such configurations seems to demand a more complete soot model capable of performing well both for premixed and diffusion flames revealing that more realistic models accounting for soot surface growth and particle aging are needed.



## Part II

# LES of thermo-acoustic instabilities



# Chapter 6

## Introduction

### 6.1 Theory and phenomenology of CI

Combustion-driven thermo-acoustic instabilities are a well known type of combustion instabilities (CI) arising in industrial combustion devices when the flame is confined in space, as is the case in combustion chambers found in power generation or aircraft propulsion gas turbine engines [9, 92, 123]. They are characterized by large amplitude pressure and heat release fluctuations, and its appearance is often unwanted. The oscillating pressure is responsible for the generation of mechanical vibrations that can lead to premature failure of the device, with its associated economic and human costs. The oscillating heat transfer rate to the liner walls of the burners is also dangerous for the structural integrity, since cracks can appear due to thermo-mechanical fatigue of the materials [30, 78, 136].

CI are the result of an interaction between a heat source (combustion in this case), pressure waves and flow characteristics [44]. These phenomena are strongly interrelated, as shown in Fig. 6.1.

Gases traversing a flame are heated up proportionally to heat release rate and, consequently, experience time-varying dilatation rates if this heat release fluctuates. Gases being heated up push the surrounding gases outwards as they expand, leading to a local pressure increase that propagates in the form of acoustic waves. In this regard the flame behaves locally as a balloon being inflated and deflated and therefore radiating sound in all directions, i.e., an acoustic monopole [61, 66, 147].

The pressure waves created by unsteady combustion travel through the combustor and, as they reach the inlet or outlet, they leave the domain or reflect back to the combustion chamber depending on the boundary impedance, where they can induce perturbations in the flow features. These perturbations can

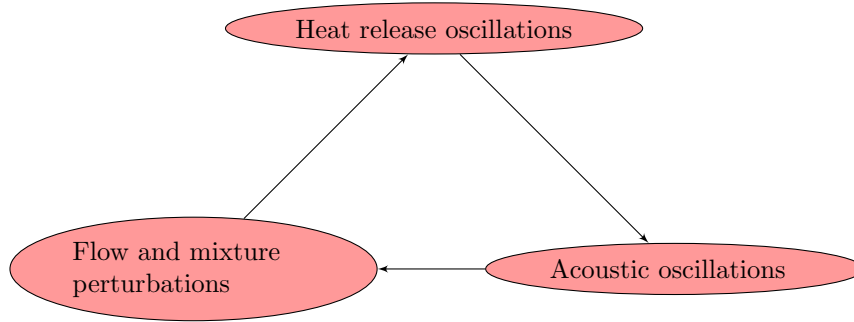


**Figure 6.1:** Feedback mechanism responsible for combustion instabilities, from Lieuwen [92].

lead to heat release rate oscillations in two ways [92]:

- Flame surface area fluctuations: Acoustic oscillations induce velocity oscillations at the same frequency as pressure oscillations. As the fresh gases flowing towards the flame front are accelerated or decelerated, the flame shape changes accordingly, leading to variations in the total flame surface area and hence to oscillations in the total heat release.
- Heat of reaction fluctuations: The power released by unit of total mass depends on the equivalence ratio  $\phi$  of the fuel/oxidizer mixture. Equivalence ratio fluctuations can be due to oscillating air and fuel inlet mass flow rates induced by acoustics.

These mechanisms make lean-premixed flames particularly sensible to the appearance of CI.

It has been explained how heat release fluctuations can drive acoustic oscillations, thus closing the loop of Fig. 6.1. However, for this chain of phenomena to become unstable, a condition must be fulfilled. The criterion to be satisfied for the existence of CI is referred to as the Rayleigh criterion [109, 125]:

$$\int_V \int_T p' q' dV dt > 0 \quad (6.1)$$

where  $p'$  and  $q'$  are the pressure and heat release rate fluctuations respectively,  $V$  is the volume of the domain and  $T$  is the period of the oscillations.

According to the Rayleigh criterion, pressure and heat release oscillations must be in phase in order for the instability to grow in amplitude or, equivalently, local pressure and heat release rate must increase or decrease simultaneously. From the point of view of thermodynamics, as gases expand against an increasing pressure field, work is done. As a result, energy from combustion is fed into the acoustic field, leading to an even higher pressure change. This phenomenon can also be seen as if the interface between expanding gases and the surroundings was moving as a solid wall. Thus, as an acoustic overpressure

arrives at the interface, it is reflected back and amplified. For this to happen, the phase shift between heat release rate and pressure oscillations must be between  $-\pi/2$  and  $\pi/2$  rad.

The Rayleigh criterion must be averaged over the whole domain to account for the net energy exchange: heat release rate and pressure oscillations might be in locally in phase at some parts of the domain while they could be out of phase elsewhere. The energy exchanges would then cancel out to yield a less effective energy exchange rate or even negative values, leading then to the suppression of the CI.

The coupling between combustion and acoustics leads to two different classes of problem: (1) since a flame can be described as a distribution of acoustic monopoles which radiate sound, it is the source of combustion noise [90, 146]. If this noise is only due to turbulence it will yield a broad-band spectrum signal (known as combustion roar), with no particular frequency being excited. (2) On the other hand, if the Rayleigh criterion is fulfilled, discrete tones will be added to the combustion roar because CI will appear.

CI are characterised by a rapid growth in pressure and heat release rate oscillations [37, 121]. The amplitude of the driving mechanism (combustion) is proportional to the amplitude in pressure oscillations. This dependence is linear for low to medium amplitude values, but non-linear effects become important for sufficiently large values of the pressure oscillations amplitude. Due to these non-linearities, heat release rate oscillations cannot grow beyond a certain point, leading to saturation. Likewise, energy losses (due to viscosity or sound radiated to the atmosphere) are also proportional to the amplitude of the pressure oscillations and linear as a first approximation (even though non-linearities are present too).

During the development of CI, the amplitude of the oscillations grows in time until losses match the energy delivered by combustion to the CI, as depicted in Fig. 6.2(a). At that point, the amplitude of the oscillations will reach a plateau, at a frequency  $A_{LC}$ . The resulting steady-state oscillatory behaviour is referred to as limit-cycle, as shown in Fig. 6.2(b).

This chapter focuses on combustion instabilities (CI) and especially on the definition of the conditions to fulfill for LES to perform a reliable prediction of instability modes. This is, in the most general case, a very difficult question [138]. Combustion instabilities are known to depend on many factors and experiments point out that the following parameters can play important roles:

- The air temperature and composition (humidity for example). Experimentalists know that combustors can be stable or unstable depending on weather conditions.
- Structure leaks: any small leak in an experiment will lead to a change of local pressure perturbation and possibly to a variation of CI. Dismounting and reinstalling a combustion chamber can lead to a change of its stability

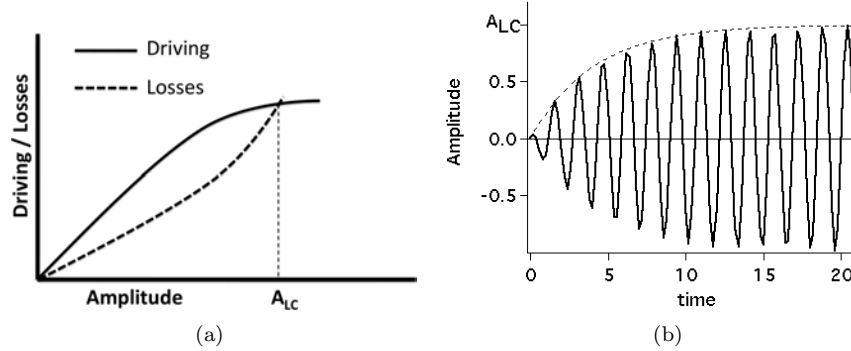


**Figure 6.2:** Features of the growth of thermo-acoustic instabilities and establishment of limi-cycle oscillations (LCO), from Lieuwen [92].

map.

- Chemistry: very small changes in equivalence ratio or in fuel composition can lead to drastic stability changes [116], an important fact in lean premixed flames.
- Heat losses at walls: taking into account heat losses changes not only the sound speed field but also the flame response to acoustic perturbations so that a combustor computed with or without heat losses exhibits different unstable modes as shown in 2007 by U. Twente and CERFACS [139] or by Alstom and CERFACS [133].
- Acoustic impedances: the reflection of acoustic waves at the inlet and outlet of the combustor directly controls the amplification of the unstable modes. In a gas turbine for example, identifying the impedances of the compressor seen by the chamber or of the turbine seen by the chamber is a challenge in itself.
- External forcing: many chambers are submitted to forcing. In most cases, this forcing is produced by upstream conditions, typically by the compressor in a gas turbine but downstream forcing can also be found.
- Forcing levels: not all combustors are linearly stable. In certain cases, a strong perturbation can initiate an instability in a system which is otherwise stable (typically in rocket engines).
- Construction tolerances: industry experts reckon that two engines built on the same specifications can exhibit different stability maps. This shows that small geometry changes can lead to different stability.

This list is not exhaustive and obviously constitutes a sobering description of the challenges to overcome for LES to be used at the design level for CI. In the present work, attention is limited to a few factors. First, the experiment is installed in a clean and controlled environment within the LIMOUSINE project at University Twente. It is a simple chamber without compressor or turbine and impedances can be reasonably well defined at inlet and outlet. No external

forcing is used. The injection of fuel is performed just upstream of the combustion chamber, leading to partially premixed flames regimes, typical of what is found in many aeronautical or ground gas turbines. Studying these phenomena in a simplified configuration as the LIMOUSINE test rig is a very useful step of validation before addressing real aero or industrial burners. This configuration is also unswirled and uses gaseous fuel to eliminate uncertainties during validation. Similarly, the air temperature and composition is very well controlled. The fuel itself is well characterized and submitted to limited changes. Therefore the study will focus on a limited set of parameters: the effects of heat losses (by radiation or by convection at walls) and the effects of acoustic impedances at the outlet and inlet. Of course, the effects of the parameters involved in the LES itself (description of chemistry, number of points) will also be considered.

The work performed on this topic is organized as follows: first, a brief description is given on the numerical tools employed for throughout this work in Section 6.2 of the present chapter. Then the geometrical features, operating points, measuring devices and experiments performed are described in Chapter 7. Finally, Chapter 8 is devoted to the presentation of the different simulations performed, where the methods employed and the results obtained are shown. Comparisons between different simulations and experimental results are presented and discussed.

## 6.2 Numerical tools for CI

### 6.2.1 Large Eddy Simulation for CI

The code used for LES in the present work is AVBP. Since this code has been described multiple times before [103, 127, 133, 139] and since limited specific developments related to CI have been performed during the present work, it will be presented rapidly here.

The code AVBP is a parallel LES code solving the filtered, compressible, reacting Navier-Stokes equations on three-dimensional unstructured grids [33, 129, 135]. Discretization of the equations is done using the finite-volumes technique with a cell-vertex approach [130]. Several numerical schemes, turbulence and combustion models and boundary conditions are available.

#### Governing equations for laminar flow

The set of equations describing the evolution of a compressible, multispecies, reacting flow reads (using Einstein's summation convention):

$$\frac{\partial \rho u_i}{\partial t} + \frac{\partial \rho u_i u_j}{\partial x_j} = -\frac{\partial}{\partial x_j} [P \delta_{ij} - \tau_{ij}] \quad (6.2)$$

$$\frac{\partial \rho E}{\partial t} + \frac{\partial \rho E u_j}{\partial x_j} = - \frac{\partial}{\partial x_j} [u_i (P \delta_{ij} - \tau_{ij}) + q_{ij}] + \dot{\omega}_T \quad (6.3)$$

$$\frac{\partial \rho Y_k}{\partial t} + \frac{\partial \rho u_j Y_k}{\partial x_j} = - \frac{\partial}{\partial x_j} [J_{j,k}] + \dot{\omega}_k \quad (6.4)$$

Equations (6.2), (6.3) and (6.4) describe the conservation of momentum, energy and chemical species respectively, where  $\rho$ ,  $u_i$ ,  $P$ ,  $\tau_{ij}$ ,  $E$ ,  $q_j$ ,  $\dot{\omega}_T$ ,  $J_{j,k}$  and  $\dot{\omega}_k$  denote, respectively, density, velocity, pressure, stress tensor, total energy, heat flux vector, heat release rate, species flux vector and chemical reaction rate.

$E$  is the total, non-chemical energy per unit mass calculated as  $E = H - P/\rho$ .  $H$  represents the total enthalpy calculated as  $H = h_s + \frac{1}{2} u_i u_i$ , where  $\frac{1}{2} u_i u_i$  is the kinetic energy of the gases and  $h_s = \int_{T_0}^T C_p dT$  is the sensible enthalpy,  $C_p$  and  $T$  being the heat capacity and temperature of the mixture respectively.

An additional expression is needed to calculate the pressure  $P$ . The ideal gas law, as shown in Eq.(6.5), is used as equation of state, where  $R^0$  is the universal gas constant and  $\bar{W}$  is the mean molecular weight of the gas mixture.

$$P = \rho T \frac{R^0}{\bar{W}} \quad (6.5)$$

### Species transport

For a multi-species flow Eq.(6.6) must be satisfied, where  $V_i^k$  is the diffusion velocity of species  $k$  in directions  $i = 1, 2, 3$  and  $N$  is the number of species. Finding the diffusion velocities of all species is, in general, a difficult task that requires solving a complex non-linear system of equations accounting for the binary diffusion of each species into each other [14, 51, 117, 153]. This is costly in terms of computing time and constitutes a problem in itself.

$$\sum_{k=1}^N Y_k V_i^k = 0 \quad (6.6)$$

Simplified approaches are often employed for the resolution of the chemical species transport term. Here the Hirschfelder & Curtiss approximation [63] is adopted, whereby the diffusion velocity is calculated using Eq.(6.7).  $D_k$ ,  $W_k$  and  $X_k$  denote, for species  $k$ , the averaged diffusion coefficient into the rest of the mixture, the molar weight and the molar fraction, respectively.

$$Y_k V_i^k = -D_k \frac{W_k}{\bar{W}} \frac{\partial X_k}{\partial x_i} \quad (6.7)$$

Summing Eq.(6.7) for all species as in Eq.(6.6) yields a non-null value, indicating that the approximation used is not conservative. To ensure mass conservation, a correction velocity  $V_i^c$  must be added in the conservation equation of each species. The species diffusion flux for species  $k$  reads then:

$$J_{i,k} = -\rho \left( D_k \frac{W_k}{\bar{W}} \frac{\partial X_k}{\partial x_i} - Y_k V_i^c \right) \quad (6.8)$$

The diffusion coefficients are simply calculated as  $D_k = D_{th}/Le_k$ , where  $D_{th}$  is the thermal diffusivity of the mixture and  $Le_k$  is the Lewis number of species  $k$ , which is assumed to be constant, since only small variations of  $Le_k$  have been reported to occur across flame fronts [117].

### Chemistry modeling

The description of the chemistry is done using Eq.(6.9) written for  $M$  reactions and  $N$  reactants  $\mathcal{M}_k$ , where  $\nu'_{kj}$  and  $\nu''_{kj}$  are the stoichiometric coefficients.

$$\sum_{k=1}^N \nu'_{kj} \mathcal{M}_k = \sum_{k=1}^N \nu''_{kj} \mathcal{M}_k, \quad j = 1, M \quad (6.9)$$

The expression for the rate progress  $\mathcal{Q}_j$  of reaction  $j$  is written in Eq.(6.10), where  $K_{f,j}$  and  $K_{r,j}$  are the forward and reverse rates of reaction  $j$  respectively.

$$\mathcal{Q}_j = K_{f,j} \prod_{k=1}^N \left( \frac{\rho Y_k}{W_k} \right)^{\nu'_{kj}} - K_{r,j} \prod_{k=1}^N \left( \frac{\rho Y_k}{W_k} \right)^{\nu''_{kj}} \quad (6.10)$$

Arrhenius expressions are used to compute the reaction rates, as expressed in Eq.(6.11), where  $A_{f,j}$  and  $E_{a,j}$  denote the pre-exponential constant and the activation energy of reaction  $j$  respectively.

$$K_{f,j} = A_{f,j} \exp \left( -\frac{E_{a,j}}{R^0 T} \right) \quad (6.11)$$

The reverse rate is calculated making use of the equilibrium constant  $K_{eq}$  [79]:

$$K_{r,j} = K_{f,j} / K_{eq} \quad (6.12)$$

Finally, the reaction rate of species  $k$  is computed as:

$$\dot{\omega}_k = W_k \sum_{j=1}^M (\nu'_{kj} - \nu''_{kj}) \mathcal{Q}_j \quad (6.13)$$

The computation of the heat release rate is straightforward using Eq.(6.13) and the enthalpy of formation of species  $k$ ,  $\Delta h_{f,k}^0$ :

$$\dot{\omega}_T = - \sum_{k=1}^N \dot{\omega}_k \Delta h_{f,k}^0 \quad (6.14)$$

### Governing equations for turbulent flow

Equations (6.2), (6.3) and (6.4) can be solved directly to describe the evolution of a laminar, unsteady flow. However, they must be handled with care if turbulence arises. LES aims at computing only the large turbulent scales of the flow, whereas the effects of the small ones (smaller than the cell size of the computational grid) are modeled through appropriate closure terms [117, 120].

In order to derive the LES equations, first a spatial filtering operator is defined as [117]:

$$\bar{f}(\mathbf{x}) = \int f(\mathbf{x}')F(\mathbf{x} - \mathbf{x}')d\mathbf{x}' \quad (6.15)$$

where  $F$  is the LES filter. Similarly, for variable density flows a Favre filtered variable  $\tilde{f}$  can be defined as:

$$\bar{\rho}\tilde{f} = \overline{\rho f} \quad (6.16)$$

According to these definitions, variables can be decomposed in a Favre averaged part  $\tilde{f}$  and a fluctuating part  $f''$  so that:

$$f = \tilde{f} + f'' \quad (6.17)$$

Applying the filtering operator to Eqs.(6.2), (6.3) and (6.4) and re-arranging, the following set of conservation equations is produced, which are suitable for LES:

$$\frac{\partial \bar{\rho}\tilde{u}_i}{\partial t} + \frac{\partial \bar{\rho}\tilde{u}_i\tilde{u}_j}{\partial x_j} = -\frac{\partial}{\partial x_j} \left[ \bar{P}\delta_{ij} - \bar{\tau}_{ij} + \underbrace{\bar{\rho}(\tilde{u}_i\tilde{u}_j - \tilde{u}_i\tilde{u}_j)}_{SGS \text{ term}} \right] \quad (6.18)$$

$$\frac{\partial \bar{\rho}\tilde{E}}{\partial t} + \frac{\partial \bar{\rho}\tilde{E}\tilde{u}_j}{\partial x_j} = -\frac{\partial}{\partial x_j} \left[ \overline{u_i(P\delta_{ij} - \tau_{ij})} + \bar{q}_{ij} + \underbrace{\bar{\rho}(\tilde{u}_j\tilde{E} - \tilde{u}_j\tilde{E})}_{SGS \text{ term}} \right] + \bar{\dot{\omega}}_T \quad (6.19)$$

$$\frac{\partial \bar{\rho}\tilde{Y}_k}{\partial t} + \frac{\partial \bar{\rho}\tilde{u}_j\tilde{Y}_k}{\partial x_j} = -\frac{\partial}{\partial x_j} \left[ \bar{J}_{j,k} + \underbrace{\bar{\rho}(\tilde{u}_j\tilde{Y}_k - \tilde{u}_j\tilde{Y}_k)}_{SGS \text{ term}} \right] + \bar{\dot{\omega}}_k \quad (6.20)$$

Equations (6.18), (6.19) and (6.20) are the equations actually resolved by the LES code, which transports and operates with filtered variables. The three contributions to the total flux are:

– **Inviscid flux**

The expressions for the inviscid flux components in the LES equations are the same as in the DNS equations, but based on filtered variables.

$$\begin{pmatrix} \overline{\rho} \widetilde{u}_i \widetilde{u}_j + \overline{P} \delta_{ij} \\ \overline{\rho} \widetilde{E} \widetilde{u}_j + \overline{u}_i \overline{P} \delta_{ij} \\ \overline{\rho} \widetilde{u}_j \widetilde{Y}_k \end{pmatrix} \quad (6.21)$$

– **Viscous flux**

The filtering process leads to unclosed expressions, which need additional assumptions for their modeling.

$$\begin{pmatrix} -\overline{\tau}_{ij} \\ -(\overline{u}_i \overline{\tau}_{ij}) + \overline{q}_{ij} \\ \overline{J}_{j,k} \end{pmatrix} \quad (6.22)$$

– **Sub-grid scale terms**

The non-linear character of the convective terms introduces some additional terms in the conservation equations when the filtering is performed.

$$\begin{pmatrix} -\overline{\tau}_{ij}^t \\ \overline{q}_{ij}^t \\ \overline{J}_{j,k}^t \end{pmatrix} = \begin{pmatrix} \overline{\rho} (\widetilde{u}_i \widetilde{u}_j - \widetilde{u}_i \widetilde{u}_j) \\ \overline{\rho} (\widetilde{u}_j \widetilde{E} - \widetilde{u}_j \widetilde{E}) \\ \overline{\rho} (\widetilde{u}_j \widetilde{Y}_k - \widetilde{u}_j \widetilde{Y}_k) \end{pmatrix} \quad (6.23)$$

These new terms represent the contribution of the non-resolved turbulent scales (scales whose size is inferior to the mesh size), and must be modeled. A model is proposed based on Boussinesq's hypothesis [19], whereby the sub-grid scale (SGS) terms are modeled as their laminar counterparts, except for the use of a turbulent viscosity  $\nu_t$  instead of the viscosity of the gases. The eddy viscosity is in turn calculated using an appropriate turbulence model. The AVBP code allows to choose among several turbulence models, the one used in the present document is presented in section 8.1. For the heat and species turbulent flux terms, the turbulent thermal and species diffusivities are computed assuming constant turbulent Prandtl and Schmidt numbers respectively.

Details on the closure of the LES equations terms are given in [29, 69].

### 6.2.2 Acoustic solver for CI

The code used for acoustic simulations in the present work is AVSP. It is a 3D parallel Helmholtz solver in the frequency domain which is used to predict eigenfrequencies and mode structure assuming that the mean flow is frozen and that the flames effect on the acoustic field can be represented through a transfer function between velocity and heat release fluctuations [36]. It solves the

eigenvalues problem issued from a discretization on unstructured meshes of a Helmholtz equation with a source term due to the flames [108].

Starting from the linearized conservation equations for mass and momentum in a reactive non-viscous low-Mach flow, one obtains [117]:

$$\frac{1}{c_0^2} \frac{\partial p_1(\mathbf{x})}{\partial t} + \rho_0 \nabla \mathbf{u}_1(\mathbf{x}) = \frac{\gamma - 1}{c_0^2} \dot{\omega}_{1T} \quad (6.24)$$

$$\frac{\partial \mathbf{u}_1(\mathbf{x})}{\partial t} + \frac{1}{\rho_0} \nabla p_1(\mathbf{x}) = 0 \quad (6.25)$$

Assuming harmonic fluctuations for the quantity  $f$  reads:  $f_1 = f' e^{-j\omega t}$ . Combining Eq. 6.24 and Eq. 6.25 yields the Helmholtz equation, solved in the frequency domain for the pressure oscillation amplitude  $p'$  at  $\omega = 2\pi f$ :

$$\nabla \cdot c_0^2(\mathbf{x}) \nabla p'(\mathbf{x}) + \omega^2 p'(\mathbf{x}) = j\omega(\gamma - 1) \dot{\omega}'_T \quad (6.26)$$

At this point, the problem can not be closed without additional assumption allowing to express the unsteady reaction rate  $\dot{\omega}'_T$  as a function of the unsteady pressure. Here, no active flame effects are considered, and the final Helmholtz equation solved for the pressure fluctuation is reduced to:

$$\nabla \cdot c_0^2(\mathbf{x}) \nabla p'(\mathbf{x}) + \omega^2 p'(\mathbf{x}) = 0 \quad (6.27)$$

Appropriate boundary conditions are needed in order for the problem to be well-posed. The eigenvalues problem is solved using the iterative Arnoldi method [88]. Further details on the equations, the hypothesis assumed and the solving algorithms are found in [140].

Using Eq. 6.27 with no RHS term cannot give information on the modes which are actually amplified or damped with combustion. However it can give the list of all acoustic modes of the burner, taking into account all geometrical details and sound speed variations since  $c_0(\mathbf{x})$  is obtained from an averaged reacting LES. Determining with AVSP which of these acoustic modes will be amplified is possible [99, 107], but was not done here.

## Chapter 7

# Configuration: the LIMOUSINE test rig

### 7.1 Objectives

The LIMOUSINE project focuses on the study of thermo-acoustic instabilities in gas turbine combustion chambers. The problem is tackled by the LIMOUSINE project partners with a multidisciplinary approach, carrying out studies ranging from experiments, to numerical simulations and analytical methods. Research is performed not only on CI themselves, but also on their consequences, namely material damage due to thermo-mechanical fatigue, arising when CI occur. Several versions of the burner were built at the Imperial College (London, UK), University of Twente (Enschede, The Netherlands), IfTA (Munich, Germany), and DLR (Stuttgart, Germany) to perform different diagnostics. The burner was designed in order to be unstable, since CI are the object of the study.

An important part of the present study is devoted to a simple 'UQ (uncertainty quantification)' analysis of LES for CI. LES is widely used today to study CI's in multiple combustors but very few authors discuss the precision of these methods and their sensitivity to multiple parameters (some of which are often not even discussed): influence of mesh, of numerical scheme, of outlet/inlet boundary conditions, of wall models, etc. Thanks to the relative simplicity of the LIMOUSINE set-up, it was possible here to investigate these questions by changing these parameters one by one and verifying the LES sensitivity to these input data. This is a critical issue for LES of self-excited CI's: if a given LES case becomes stable or unstable when the grid changes or when a submodels (at the walls for example) is replaced, it is difficult to claim that LES can be used to discriminate between a stable or an unstable case in the real world. Such questions begin to be raised in the combustion LES community today [53] and this thesis tries to contribute to this discussion in addition to studying the LIMOUSINE set-up.

The configuration described hereafter corresponds to the burner computed with LES, referred to as V.3.

## 7.2 Geometry and operating characteristics

The burner was originally conceived as a Rijke-tube like burner, with rectangular ducts open to the atmosphere at both ends. Later on, the burner was modified to a closed-open configuration. It consists of two rectangular ducts of different widths welded together. A triangular bluff body is located at the interface between both ducts and its main purpose is to stabilize the flame. The burner is oriented vertically, with gases flowing upwards. Fig. 7.1 shows the test rig as it is mounted in the laboratory at the University of Twente. An aluminum frame is used to provide structural support to the combustor and the auxiliary hardware. A chimney is placed right above the burner so as to evacuate the burnt gases from the laboratory. The full burner geometry is shown in Fig. 7.2.



**Figure 7.1:** Picture of the LIMOUSINE test rig installed at the University of Twente.

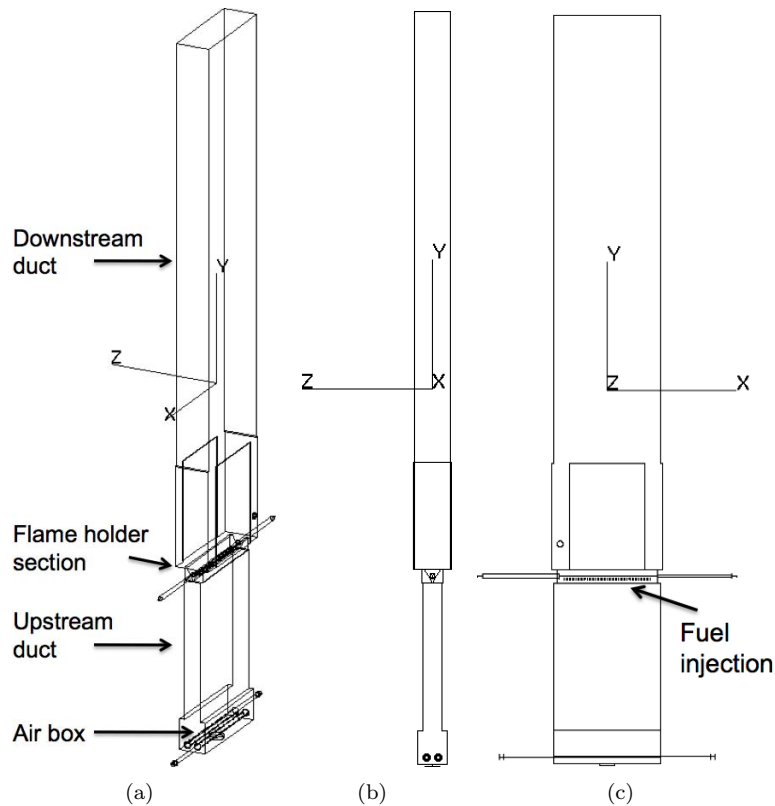


**Figure 7.2:** Full burner geometry views. (a) Global view. (b) Front view. (c) Side view. Drawings provided by the University of Twente.

A cavity is present at the bottom end (referred to as air box in Fig.(7.2(a))), where air is injected through holes drilled on the sides of two pipes crossing the cavity. The air box allows to obtain an acoustically closed boundary condition at the bottom end.

Methane is injected in cross flow with respect to the air stream in order to improve the fuel/air mixing. Fuel injection is done through two rows of holes evenly distributed on both sides of the triangular bluff body. Details of the fuel injection and the flame stabilization wedge are shown in Fig. 7.3.

Full optical access to the flame is granted due to glass windows mounted on the burner walls above the wedge. Stainless steel 310 and 316 are used for the burner walls and most of the structural elements and the wedge is made of brass. The windows are made of quartz glass and graphite is used for the gaskets that seal the junctions between the windows and the steel frame.

Geometrical dimensions of the burner parts are summarized in Table 7.1.

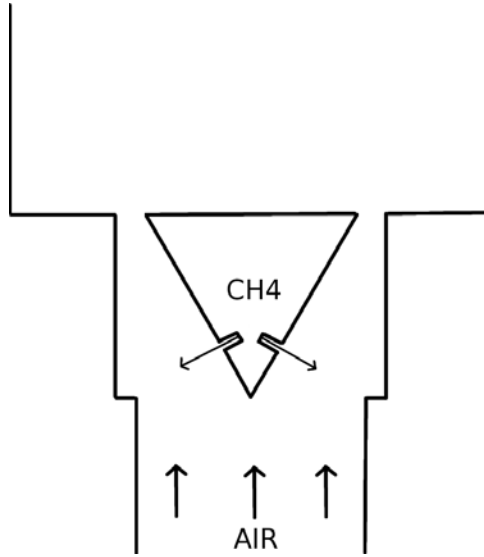


**Figure 7.3:** Detailed view of the fuel injection and wedge zones.

Part	Length	Width	Diameter	Side
Upstream duct	210	25	—	—
Downstream duct	780	50	—	—
Air holes	—	—	2	—
Fuel holes	—	—	1	—
Wedge	—	—	—	22

**Table 7.1:** Burner geometry dimensions indicated in *mm*.

Fuel and air are injected at ambient temperature and the burner operates at atmospheric pressure, as it is open to the atmosphere at the top end. The test rig works under fuel-lean premixed conditions and is capable of delivering up to 80 kW of power.

### 7.3 Measurement devices

Pressure is recorded over time using six pressure probes mounted on the walls at different locations along the combustor. Temperature of the gases is measured using four thermocouples mounted on the burner walls as well, but their tip is separated 4 cm from them so as to measure the temperature of the gases stream away from the thermal boundary layers. The location of the

pressure probes and the thermocouples is sketched in Fig. 7.4 and summarized in Table 7.2.

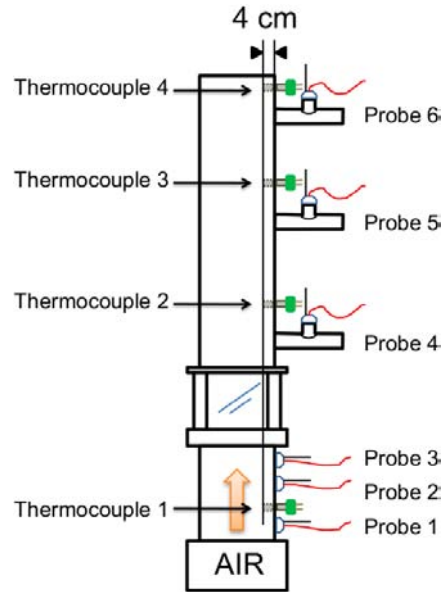


**Figure 7.4:** Location of the six pressure probes and the four thermocouples on the test rig. Drawing provided by the University of Twente.

Sensor \ Number	1	2	3	4	5	6
Pressure probes	-17.9	-11.9	-5.9	20.4	45.4	70.4
Thermocouples	-14.9	23.9	49.4	74.9	—	—

**Table 7.2:** Pressure probes and thermocouples location along the  $y$  axis indicated in  $cm$  with respect to the upper wall of the triangular bluff body.

A photomultiplier with a  $OH$  radical filter faces the front window of the test rig to measure the global heat release variations within the burner.

Finally a camera with a  $CH$  radical filter is placed facing the rear window of the burner. It records the flame movement at a frequency of 500 Hz and gives information about the flame location and shape.

## 7.4 Experiments

In order to define the stability range of the combustor, a series of experiments was conducted. Power (or equivalently fuel inlet mass flow rate) was fixed at 20 kW, 40 kW and 60 kW and the air factor  $\lambda$  was varied (or equivalently air inlet mass flow rate). First,  $\lambda$  was increased until the burner switches from unstable

to stable regime, and further increased until the flame is blown out. The same experiment was repeated, starting from a stable regime and decreasing  $\lambda$  until switch to instability occurs. The unstable behaviour was readily identified by the high sound levels registered during operation.

Fig. 7.5 shows curves delimiting the stability regions as a function of power and  $\lambda$ , as well as the blow-out limit. The combustion regime (i.e., stable or unstable) was easily identifiable: a silent flame was observed for the case referred to as “stable”, except for some low-amplitude background noise. On the other hand, a very high-amplitude pure tone was heard when the system entered the region referred to as “unstable”. Hearing protection had to be worn by the operators during unstable combustion, since noise up to 130 dB was registered in the laboratory during such regime. Hysteresis was observed in the passage from stable to unstable behaviour and viceversa. Hence, when  $\lambda$  was decreased towards the unstable region, in order to reach instability it had to be decreased below the value marking the transition to stability in the ascending  $\lambda$  experiment. This is a phenomenon commonly observed during thermo-acoustic instabilities [65] and the responsible mechanism is discussed later on in the present document.

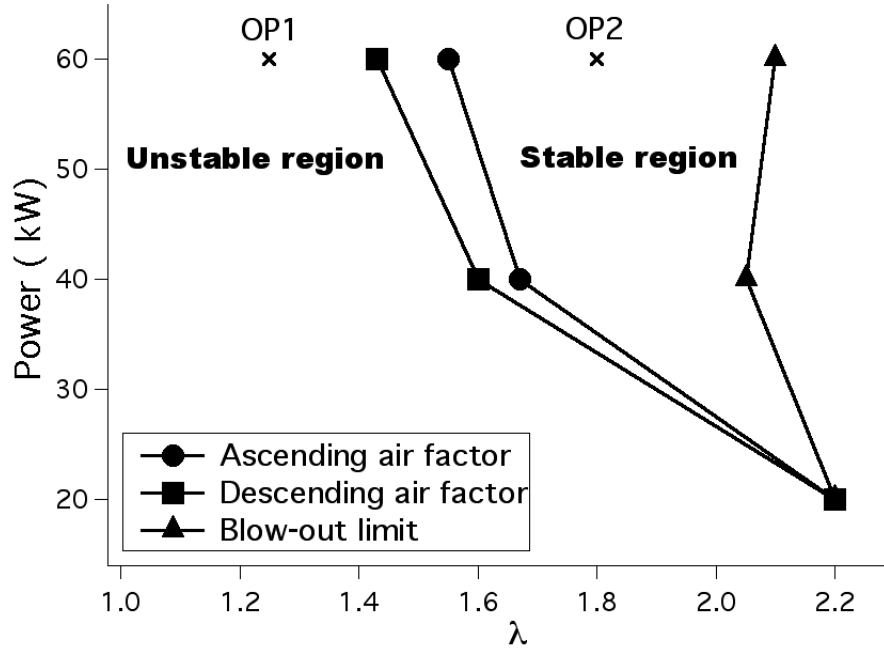


Figure 7.5: Stability map of the V.3 LIMOUSINE burner.

Detailed measurements were performed for two particular operating points (OP), the characteristics of which are summarized in Table 7.3. As seen in

Fig. 7.5, points 1 and 2 correspond to unstable and stable behaviour of the combustor, respectively. The points were chosen to check that LES would be able to reproduce the stability characteristics, i.e., “stable” or “unstable” . At this point, no attempt was made to track the stability limits, i.e., the values at which the combustor transitions from “stable” to “unstable” or viceversa. This is left for further studies. Measurements of both OP and comparisons with the numerical simulations are shown in Section 8.11.

Operating point	Power (kW)	$\lambda$
OP1	60	1.25
OP2	60	1.8

**Table 7.3:** Characteristics of the operating points (OP) for which detailed measurements were taken.



## Chapter 8

# LES of the LIMOUSINE test rig

### 8.1 Computational parameters

Several numerical simulations of the flow and combustion dynamics on the LIMOUSINE test rig were performed using the LES tool AVBP. A baseline simulation is taken as a reference, with respect to which several parameters are changed in order to assess their influence on the flow and combustion characteristics.

The reference simulation, hereafter referred to as Simulation 1, corresponds to the version V.3 of the LIMOUSINE test rig at OP1, and the numerical parameters employed are as follows:

- **Computational domain and mesh:** Two observations were made prior to the definition of the computational domain. Firstly, the fuel holes are arranged along two rows on both sides of the wedge and evenly distributed. Hence, two consecutive pairs of holes are located on planes perpendicular to the length of the wedge at a distance of 4 mm. The second observation is that the burner is slender, its vertical length being much larger than the other characteristic distances. Consequently, the vertical axis is a privileged direction and longitudinal acoustic modes are most likely to appear. Due to these two facts, a reduced spatial domain was defined for the simulations, where only a slice of the whole burner is considered (see Fig. 8.1(b)). The slice is 4 mm deep and corresponds to the space confined by two planes parallel to the vertical axis, so that only one pair of holes is included. The choice of the computational domain implies that interaction between adjacent pairs of fuel inlets is neglected. A semicircular atmosphere was included in the computational domain (see Fig. 8.1(a)) for computational reasons explained below.

The domain is discretized using an unstructured mesh composed of 1.1 M

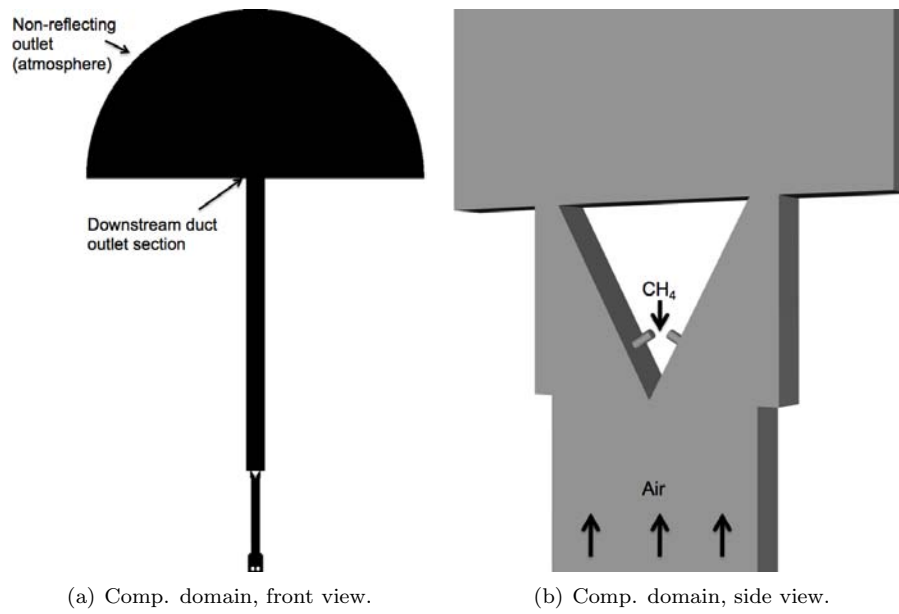


**Figure 8.1:** (a) Front and (b) side views of the computational domain.

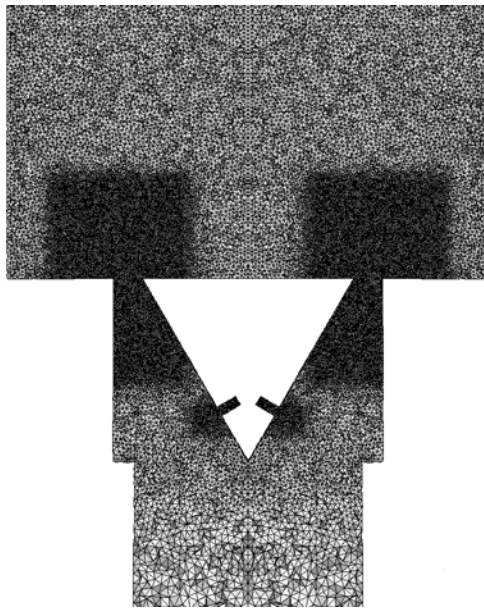


**Figure 8.2:** Detail of the mesh around the fuel injection and wedge zone.

nodes using tetrahedral elements for the standard mesh (finer grids will also be tested to verify mesh independency). A characteristic size of 1.5 mm is imposed everywhere except in certain regions, where the mesh was refined on purpose. These critical regions correspond to the fuel injection and mixing, and flame zone areas, where a mesh size of 0.18 mm and 0.4 mm was imposed, respectively. Details of the mesh size distribution around these areas are seen in Fig. 8.2.

- **Numerical method:** A one-step explicit temporal integration, second-order in space and time numerical scheme was employed. It is an adaptation of the Lax-Wendroff (LW) scheme [83] to the cell-vertex formulation. It presents reasonable diffusive and dispersive properties at a fairly low computational cost.
- **Boundary conditions:** On solid walls, the normal velocity component with respect to the wall normal is set to zero, while the no-slip condition is relaxed to allow for a non-null velocity component parallel to the walls. Resolving the boundary layer in the context of LES for industrial applications is beyond the computational resources available nowadays [58, 114]. Here, the fluid friction on solid walls is modeled with a law of the wall boundary condition, as turbulence is supposed to be in equilibrium near walls in the absence of big flow separation.

All solid walls are adiabatic, except for the downstream duct walls and the wedge walls, where heat losses are taken into account. These parts will be in contact with the hot gases resulting from combustion: it is important to model the heat losses since they might have an impact on the flame and flow features [138]. Heat losses are modeled by using a simple dual method where the wall temperature is not imposed (nor the heat flux) but is the result of an energy balance between the flux reaching the wall (given by LES) and the flux crossing the wall and convected outside. The approach used in AVBP [133] is to introduce a thermal resistance of the wall  $R_t$ , so that the heat flux  $q_w$  to the walls can be calculated with Eq. 8.1.

$$q_w = \frac{T_{ext} - T_{w1}}{R_t} \quad (8.1)$$

Heat losses through the walls are sketched in Fig.(8.3), where  $T_{ext}$ ,  $T_{w2}$ ,  $T_{w1}$  and  $T_{fluid}$  represent the temperatures of the exterior (the laboratory room in this case), of the wall in contact with the exterior, of the wall in contact with the LES domain and of the first point off the wall and within the LES domain, respectively.  $T_{ext}$  is specified and  $T_{w1}$  is calculated iteratively to ensure heat flux continuity at the wall using  $T_{fluid}$  and a wall function from Kader [71] for turbulent thermal boundary layers.

Here, both conductive and convective heat transfer modes are considered. Empirical correlations found in [68] were employed to estimate the convection coefficient on the walls. Different coefficients are used for the wedge and for the walls: the wedge walls were supposed to be internally cooled

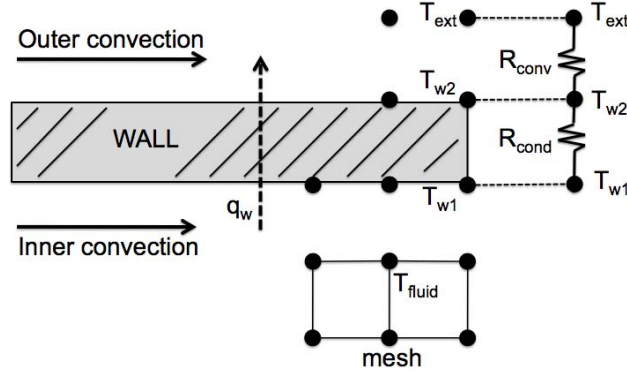


**Figure 8.3:** Sketch of the heat loss boundary condition and the associated thermal circuit representing the conductive and convective heat losses.

by the fresh fuel flowing along its inner tube, the Gnielinski correlation for internal convection was used. Natural convection outside of the burner was supposed to be the heat transfer mechanism along the liner walls, the Churchill & Chu correlation for natural convection over a vertical flat plate was employed to estimate the outer convection coefficient. Given the series configuration of the thermal circuit on the right side of Fig.(8.3), the total thermal resistance  $R_t$  was calculated as the sum of both conductive ( $R_{cond}$ ) and convective ( $R_{conv}$ ) thermal resistances, as in Eq. 8.2. The estimated values of  $R_t$  are summarized in Table 8.1.

$$R_t = R_{cond} + R_{conv} \quad (8.2)$$

Location	$R_t [W/m^2 K]$
Wedge walls	$3.3 \cdot 10^{-3}$
Liner walls	$7.17 \cdot 10^{-4}$

**Table 8.1:** Estimated thermal resistances across the wedge and liner walls of the combustor.

For inlets and outlets, boundary conditions are used following the Navier Stokes Characteristic Boundary Conditions (NSCBC) formalism from Poinot & Lele [115]. Air and fuel inlet mass flow rates are set in a soft way, as a relaxation coefficient  $K_{in} = 1000$  is used to relax the inlet variables to their reference values, permitting inlet flow variations. A relaxation coefficient  $K_{out} = 10$  was used at the atmosphere outlet. This soft boundary condition allows for pressure fluctuations at the outlet, but is large enough to prevent pressure within the computational domain to drift from its reference value ( $P_{ref} = 101325$  Pa). Imposing correct acoustic boundary conditions is a crucial element in the computation of thermo-acoustic

instabilities, since the stability characteristics depend strongly on the reflection coefficient, which determines the amount of acoustic energy leaving the domain. Here, the problem of finding the correct reflection coefficient at the burner outlet is avoided by the inclusion of the atmosphere in the computational domain. Non-reflecting boundary conditions are imposed at the atmosphere outlet, while acoustics at the burner outlet is directly resolved by the LES.

- **Turbulence model:** The turbulent viscosity  $\nu_t$  is modeled here using the classical Smagorinsky model [141]. This model was originally developed for meteorological applications. In the Smagorinsky model,  $\nu_t$  is proportional to the resolved filtered strain tensor  $\widetilde{S}_{ij}$ , the mesh size  $\Delta = V_{cell}^{1/3}$  and a constant  $C_S$  which takes values typically between 0.1 and 0.18 (it is fixed to 0.18 in the code).

$$\nu_t = (C_S \Delta)^2 \sqrt{2\widetilde{S}_{ij}\widetilde{S}_{ij}} \quad (8.3)$$

This is an easy to implement model that performs sufficiently well for flows away from solid walls at low computational cost. However, it is known to be too dissipative. In particular, its use in the simulation of wall-bounded flows in combination with no-slip boundary conditions leads to an overprediction of the fluid friction on walls, as  $\nu_t$  is overpredicted since it is proportional to velocity gradients. Here, slip (with law of the wall) walls are used, thus justifying the use of the Smagorinsky model.

- **Combustion model:** Turbulent combustion is modeled using a Dynamic Thickened Flame Model (DTFM) from L egier [87]. The model stems from classical dimensional analysis of premixed flames [153] showing the dependence of the flame front thickness  $\delta$  and the laminar flame speed  $S_L$  on the reaction rate pre-exponential constant  $A$  and the diffusion coefficient  $D$ , as in Eqs. 8.4 and 8.5.

$$\delta \propto \sqrt{\frac{D}{A}} \quad (8.4)$$

$$S_L \propto D \cdot A \quad (8.5)$$

The model thickens the flame front so as to be able to resolve the flame structure with the mesh used in the LES.  $D$  and  $A$  are then multiplied and divided respectively by a thickening factor  $\mathcal{F}$ . The model has the property of thickening the flame front by a factor  $\mathcal{F}$  while preserving the flame propagation velocity  $S_L$ .

Fig. 8.4 shows how the flame front loses some of its features when thickening is applied. The thickened flame front shows a much lower flame area, which would diminish the amount of heat and radical species diffusing through it. To account for this SGS flame wrinkling an efficiency factor  $E$  from Charlette et al. [31] is employed, as shown in Eq.8.6.

$$E = \left( 1 + \min \left[ \frac{\Delta}{\delta_l^0}, \Gamma \left( \frac{\Delta}{\delta_l^0}, \frac{u'_\Delta}{s_l^0}, Re_\Delta \right) \right] \right)^\beta \quad (8.6)$$

where  $\Delta$  is the implicit filter size of the LES,  $u'_\Delta$  the SGS rms velocity and  $s_l^0$  and  $\delta_l^0$  denote respectively the propagation velocity and the thickness of the corresponding laminar flame.  $Re_\Delta$  is a Reynolds number calculated as  $Re_\Delta = s_l^0 \delta_l^0 \nu$ , with  $\nu$  being the viscosity of the fresh gases. The only model parameter is  $\beta$ . Both diffusion and reaction terms are multiplied by  $E$ .

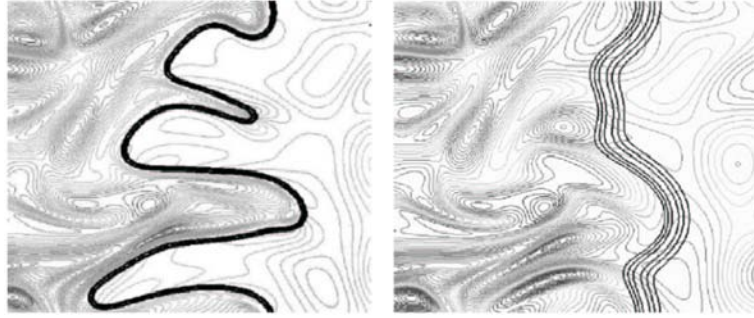


**Figure 8.4:** Direct Numerical Simulation of flame/turbulence interaction by Veynante [117]. Left: non-thickened flame. Right: thickened flame with  $\mathcal{F} = 5$ .

In the present simulations, reactants are not fully premixed and the dynamic version of the TFLES model is used [133, 138].

In this model, thickening is applied only in the reaction zone which is detected using a flame sensor. Outside reaction zone equations, standard LES equations are applied for all variables and mixing for example is computed without any effect of the thickening.

## 8.2 Presentation of simulations

### 8.2.1 Simulations performed

The previous section has described what we will call the “reference” simulation. To investigate the effects of computational parameters, multiple other cases were computed, changing parameters one at a time (highlighted in **bold**) to verify their influence. All these tests were performed on the V.3 version of the LIMOUSINE test rig for the operating point OP1 in Fig. 7.5, and presented in Table 8.2. The objective is to verify which parameters control the LES output.

Simulation	$K_{fuel}$	$K_{air}$	Mesh	Num. scheme	Heat losses
1	$10^3$	$10^3$	1.1 M nodes	LW	Cond./Conv.
1.1	<b><math>10^5</math></b>	$10^3$	1.1 M nodes	LW	Cond./Conv.
1.2	$10^3$	<b><math>10^5</math></b>	1.1 M nodes	LW	Cond./Conv.
1.3	$10^3$	$10^3$	<b>2.8 M nodes</b>	LW	Cond./Conv.
1.4	$10^3$	$10^3$	<b>4.4 M nodes</b>	LW	Cond./Conv.
1.5	$10^3$	$10^3$	1.1 M nodes	LW	<b>Adiabatic</b>
1.6	$10^3$	$10^3$	1.1 M nodes	LW	<b>Cond./Conv./Rad.</b>

**Table 8.2:** Simulations performed on version V.3 of the LIMOUSINE test rig at OP1 and their associated parameters.

In addition, other simulations were performed, corresponding to other OP and burner configuration, as summarized in Table 8.3.

Simulation	OP	Burner version	Regime
1	OP1	V.3	Unstable
2	<b>OP2</b>	V.3	Stable
3	OP1	<b>V.2</b>	Stable

**Table 8.3:** Simulations performed on the different versions of the LIMOUSINE test rig and at different operating points.

### 8.2.2 Computational resources and cost

LES demands large computational resources. For the simulations performed in this work, an IBM iDataPlex parallel computer was used. The simulations were run on 128 cores Intel Nehalem, featuring 2.67 GHz and 24 GB of memory.

The CFL condition imposes small time steps that vary slightly during the run of a simulation, oscillating around typical values of  $\Delta t = 4 \cdot 10^{-8} s$ . The time needed to compute one timestep is around 0.77 s. The total duration of a simulation would then depend on the physical time computed. For instance,

for Simulation 1, 300 ms were computed, and the computational time was 1600 hours (2,2 months), with a total computational cost of  $2 \cdot 10^5$  CPU hours.

The cost of a numerical simulation is estimated as 0.075 \$/CPU hour, accounting for the energy consumed by the computer, as well as the auxiliary systems (cooling). For Simulation 1, the total cost of the simulation is 15000 \$. This information must be surprising, and could drive the reader to think that numerical simulation is expensive. The reality is that, even if the cost associated to the computer power is not negligible, let's recall that the cost of an experimental study of an industrial combustor would be orders of magnitude higher, highlighting again the importance of numerical simulation on the design process.

### 8.3 Simulation 1: reference case for OP1

#### 8.3.1 Cold flow

Prior to a calculation of reactive flow, a cold flow simulation was performed in which the chemical reactions are frozen. This allows to isolate the dynamics of the gases within the chamber and the fuel/air mixing from the combustion process.

Figure (8.5) shows a cut of an instantaneous solution of the velocity modulus field of Simulation 1 in cold flow at the middle plane ( $x = 0$ ). The bulk velocity of the air along the upstream duct is 7 m/s, with a Reynolds number (based on the upstream duct width, 25 mm) of  $Re_{ups} \approx 11000$ . Fresh gases accelerate as they flow through the narrow gaps between the wedge and the side walls, reaching a velocity of up to 40 m/s.

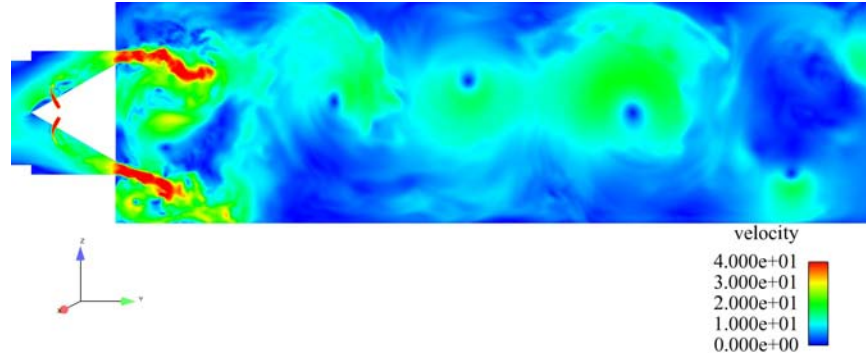


**Figure 8.5:** Cut of an instantaneous field of the velocity modulus of Simulation 1 in cold flow at the middle plane ( $x = 0$ ).

Even though the geometry is symmetrical with respect to the middle plane along the burner, the flow is not. In particular, asymmetric vortex shedding from

the wedge corners is observed. These vortices are transported downstream with the mean flow, where they coalesce and are slowly dissipated due to viscosity far downstream. The frequency of the vortex shedding gives a Strouhal number of  $St = 0.22$ . The Strouhal number was calculated as  $St = \frac{fD}{U}$ , where  $f$  is the frequency of the vortex shedding,  $D$  is the length of a the wedge side and  $U$  is the bulk velocity at the upstream duct. This value of  $St$  is somewhat lower than the one reported by Roshko [126], where he found a value of  $St = 0.28$  for the vortex shedding frequency over two-dimensional bluff bodies of arbitrary shape. The difference is ascribed to the fact that the configuration is not exactly a bluff body placed in a duct of constant section, so that the section change affects the flow features.

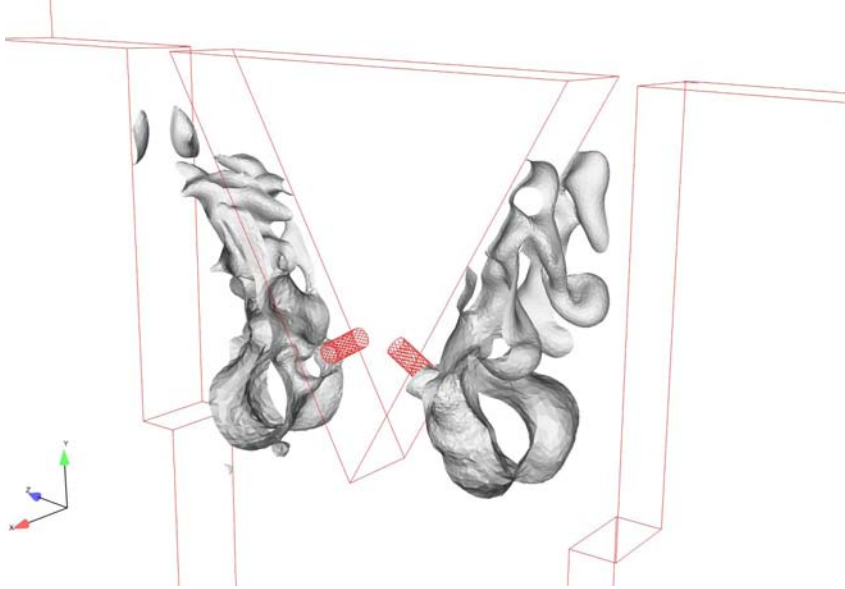


**Figure 8.6:** 3D view around the fuel injection zone of an isosurface of fuel mass fraction at the stoichiometric value ( $Y_{CH_4} = 0.055$ ) corresponding to Simulation 1 in cold flow..

Fig. 8.6 shows a 3D view of the fuel mass fraction at the stoichiometry for Simulation 1 in cold flow and reveals that three-dimensional effects are important around the jets in cross flow to correctly describe the fuel/air mixing. However, the flow remains essentially two-dimensional in a large part of the chamber. We will plot fields mainly in the injectors plane which captures most of the interesting physics.

Figure 8.7 shows an averaged solution over 100 ms of the vertical velocity component,  $v$ , as well as isocontours of  $v = 0$  of Simulation 1 in cold flow. The gases recirculate in the central recirculation zone (CRZ), which is the largest

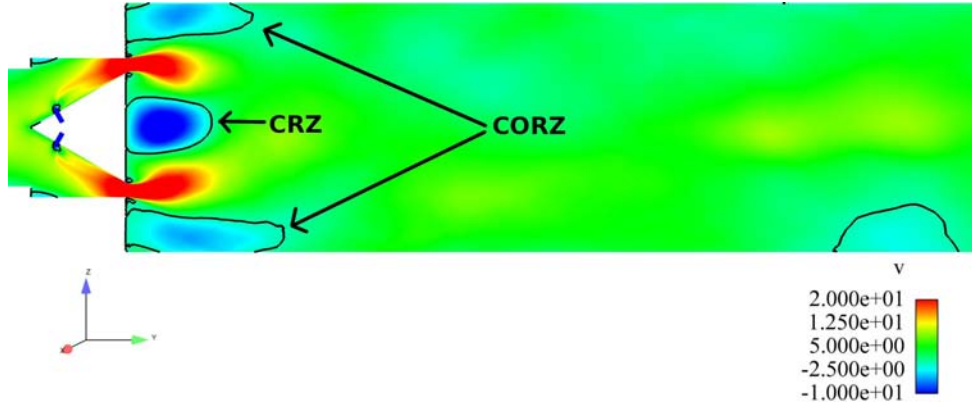
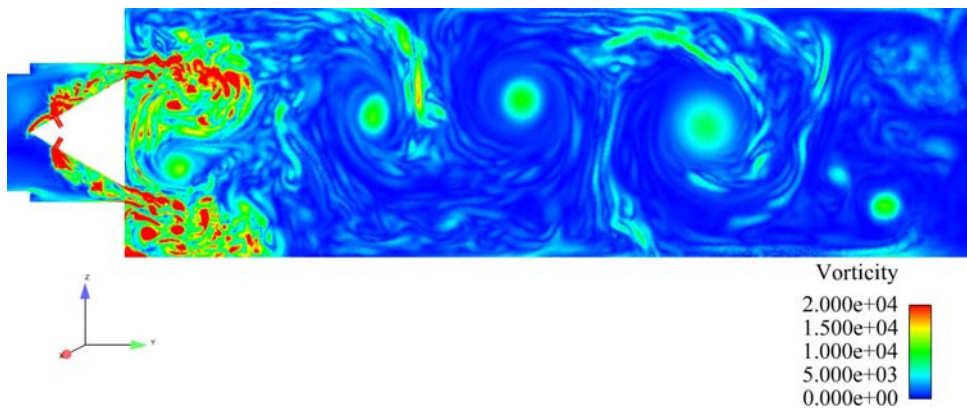


**Figure 8.7:** Cut of a mean field of the vertical velocity component  $v$  and isocontours of  $v = 0$  (solid black lines) of Simulation 1 in cold flow at the middle plane ( $x = 0$ ).

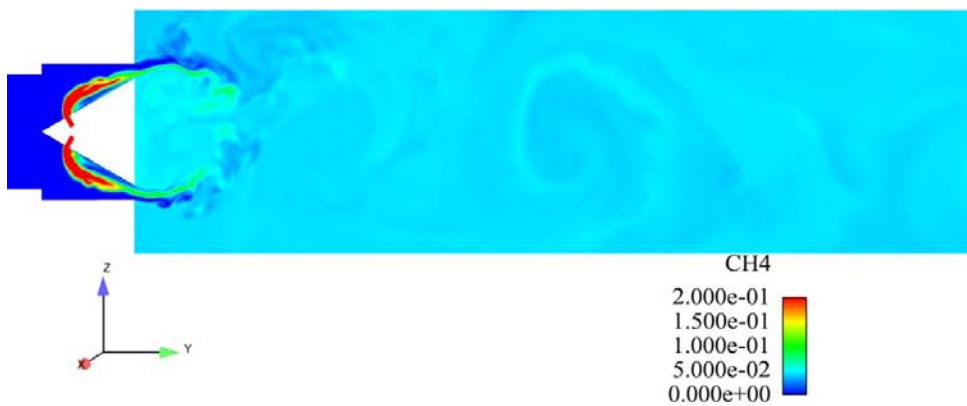
recirculation zone and stabilizes the flame. Also, recirculation occurs in the region comprised between the issuing fresh gases jets and the liner walls of the downstream duct, referred to as corner recirculation zones (CORZ), which are about 2 cm long. These regions also play an important role in the flame stabilization process and the onset of CI's, as will be explained in the next section.

Figure 8.8 shows an instantaneous solution of the vorticity field of Simulation 1 in cold flow. It is seen that a high shear is produced at the gaseous fuel jets issuing into the chamber, since they exit the holes at high velocity in cross flow with respect to the incoming air stream, thus high velocity gradients occur. Also, shear layers are observed at both sides of the fresh gases jets issuing into the downstream duct, since the flow is strongly accelerated as they traverse the narrow gaps (3 mm wide). Concentrated vorticity spots are found downstream of the wedge, indicating the vortex cores resulting from the alternative vortex shedding.

Figure 8.9 shows an instantaneous fuel mass fraction field of Simulation 1 in cold flow. Pure methane is injected through the fuel injection holes. As fuel enters the chamber it starts mixing with the air stream. Mixing is enhanced due to the cross flow configuration. However, it is seen that the fuel is not fully mixed at the entrance of the downstream duct: two separate layers of pure air and a rich fuel/air mixture are observed at that section. This mixture inhomogeneity will lead to a partially premixed combustion mode, as explained in the following section. Finally, a homogeneous mixture is observed downstream, which is not representative of the hot flow, since no methane will be found in the burnt gases region.



**Figure 8.8:** Cut of an instantaneous field of the vorticity modulus of Simulation 1 in cold flow at the middle plane ( $x = 0$ ).



**Figure 8.9:** Cut of an instantaneous field of methane mass fraction of Simulation 1 in cold flow at the middle plane ( $x = 0$ ).

### 8.3.2 Hot flow

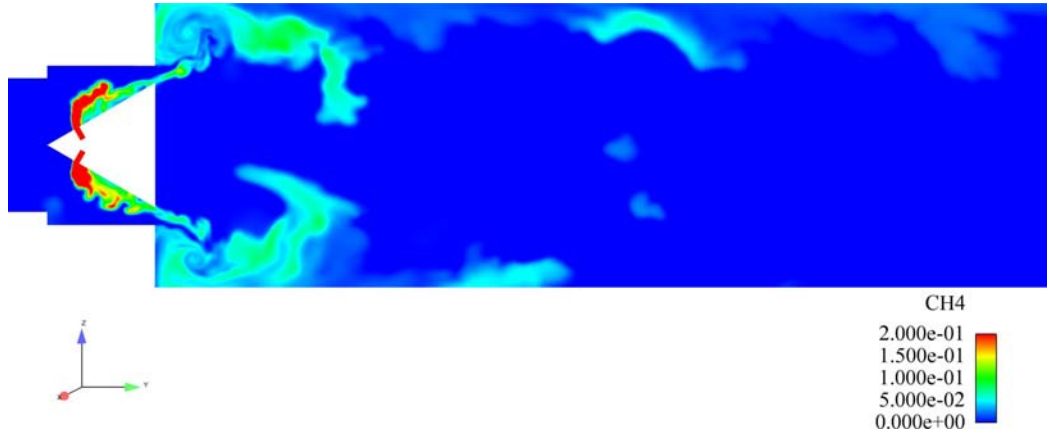
In order to ignite the mixture and reach steady state rapidly, hot burnt gases are imposed all along the downstream duct, and the chemical reactions are activated starting from a cold flow solution. This procedure is not representative of the way the burner is ignited in the experiment, which is done using a spark plug. However, ignition is not the object of study here, where we focus on the subsequent combustion process and on CI's.

### Global features of the hot flow

Figures (8.10) to (8.14) correspond to a time instant posterior to ignition, when the effects of the artificial initialization of the hot flow simulation have been forgotten.

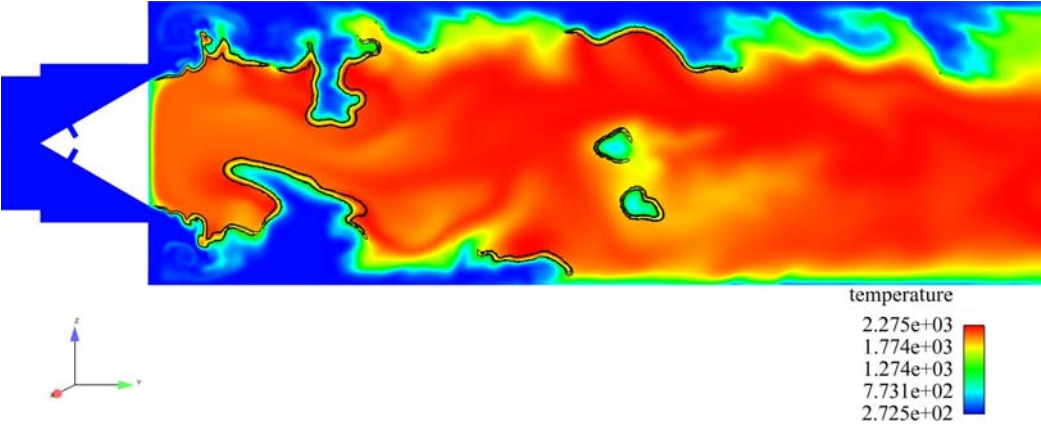
Figure (8.10) shows an instantaneous solution of the fuel mass fraction field. Unlike in Fig.(8.9), the fuel burns after entering the chamber. There is no remaining fuel far downstream, everything is consumed, as the mixture is globally lean ( $\lambda = 1.25$ ).

Figure (8.11) shows an instantaneous solution of the temperature field and isocontours of the first reaction rate, which indicates the position of the flame front. The burnt gases in the CRZ ignite the fresh gases as they enter the chamber, stabilizing the flame around the wedge. The heat losses through the wedge walls lead to a flame which is not completely attached to the bluff body, but somewhat lifted off. The liner walls on the first part of the downstream duct are shielded from the hot gases due the fresh gases, which penetrates a distance of  $\sim 5 - 10$  cm into the chamber before burning completely. Fig.(8.11) also shows that the temperature on near the walls downstream is lower than at the core of the burnt gases stream, which is due to the heat losses model through the liner walls discussed in Section 8.1.



**Figure 8.10:** Cut of an instantaneous field of methane mass fraction of Simulation 1 in hot flow at the middle plane ( $x = 0$ ).

Figure 8.12 shows a three-dimensional view of a reaction rate isosurface coloured by temperature. It is seen that the flame is essentially two-dimensional, presenting some wrinkling in the span-wise direction due to small turbulent scales. In the following, only cuts of the LES solutions on the middle plane of the computational domain will be shown, since they show all the physical features of the flow in most part of the chamber.



**Figure 8.11:** Cut of an instantaneous temperature field and isocontours of reaction rate (solid black lines) of Simulation 1 in hot flow at the middle plane ( $x = 0$ ).

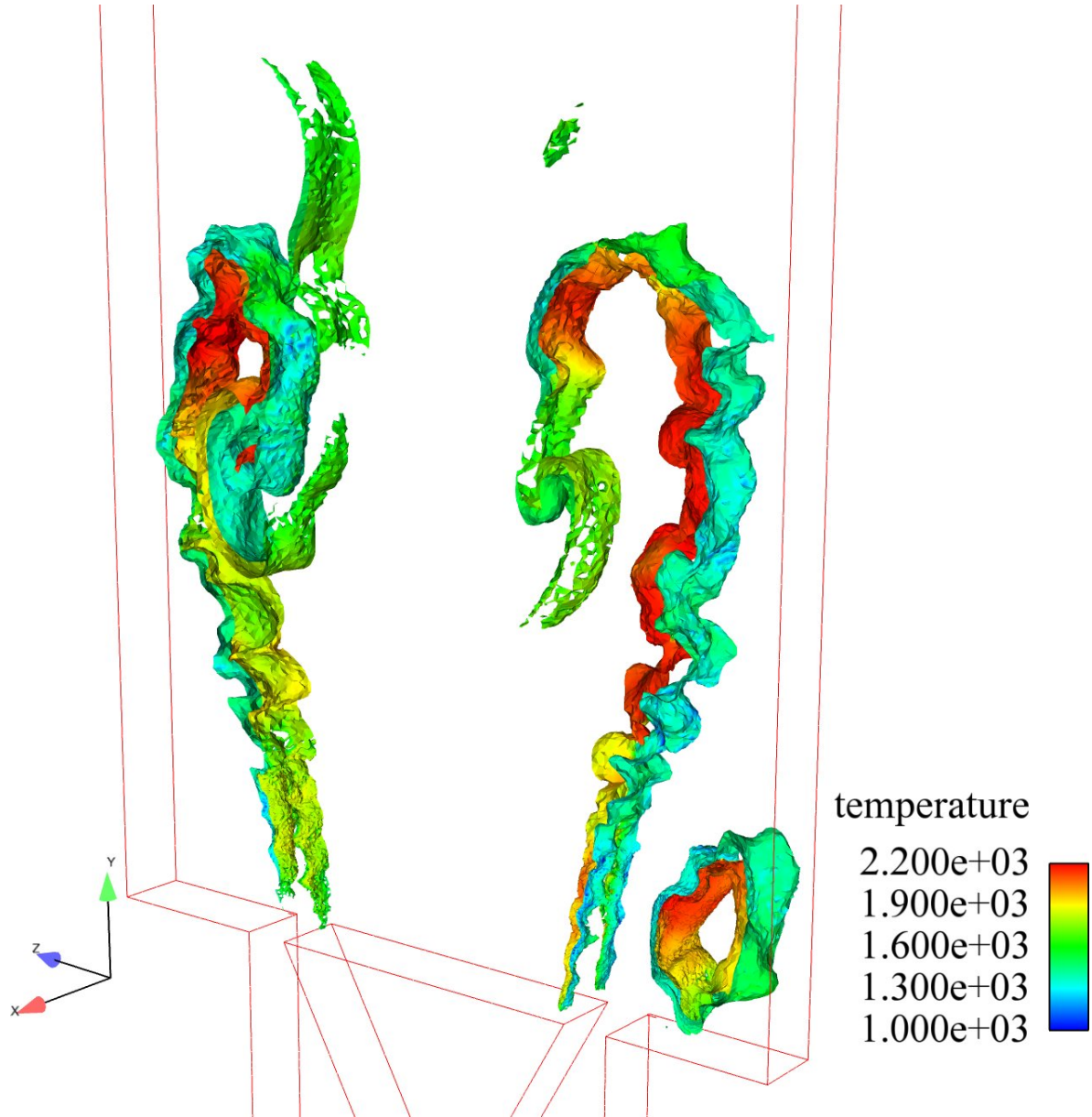


**Figure 8.12:** 3D view of an isosurface of reaction rate coloured by temperature depicting the flame shape and position corresponding to an instantaneous solution of Simulation 1.

As to the flame structure, Fig. 8.13 shows a scatterplot of the heat release versus the mixture fraction  $Z$ , which is a conserved scalar based on the number of carbon atoms [81] and conveniently normalized, as shown in Eq.(8.7):

$$Z = W_{CH_4} \left( \frac{Y_{CH_4}}{W_{CH_4}} + \frac{Y_{CO_2}}{W_{CO_2}} + \frac{Y_{CO}}{W_{CO}} \right) \quad (8.7)$$

where  $W_C$  is the molar mass of carbon. The scatterplot contains all the points of the simulation. It reveals that combustion takes place over a wide range of mixtures and not only at the mean mixture fraction of the burner ( $Z_{mean} = 0.045$ ). The regime is clearly “partially premixed”. The maximum heat release is found at the stoichiometric mixture fraction for a methane/air mixture ( $Z_{st} = 0.055$ ) as expected from theory [117]. This partially premixed mode of combustion is a direct consequence of the fuel/air mixing process, which does not have enough time to reach completion before the fresh gases arrive at the flame front.

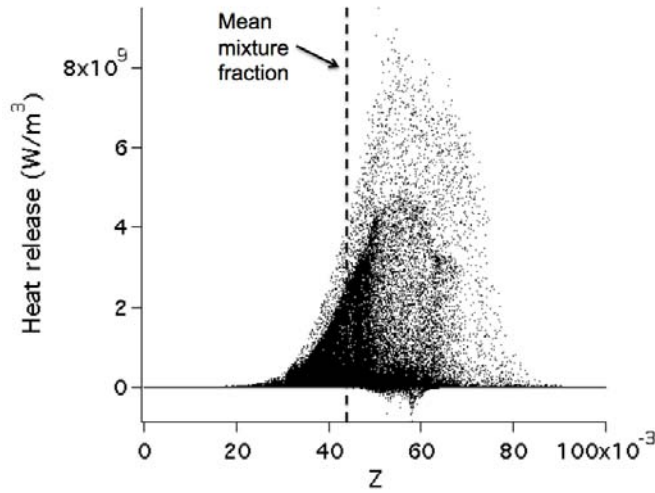


**Figure 8.13:** Scatterplot of heat release versus mixture fraction of an instantaneous solution of Simulation 1. The distributed shape indicates that combustion occurs in a partially premixed mode.

The Thickened Flame LES (TFLES) model was designed initially for perfectly premixed flames [32]. It has been extended and used for multiple diffusion flames [134, 139] even though it is not supposed to be strictly valid for pure diffusion flames. In practice, most flames computed recently with TFLES have been real diffusion flames but partially premixed situations where mixing is fast and the local flame / turbulence interactions correspond to locally premixed flames interacting with turbulence. For such cases, locally, the interaction is still correctly captured by the TFLES model if the local flame parameters (flame thickness and speed) are adjusted dynamically to the local conditions (controlled by

the equivalence ratio which is measured in AVBP using the mixture fraction). In other words, the TFLES model works correctly if the regime of the flame corresponds to a collection of individual premixed flames (at various equivalence ratios but all in the premixed mode). The scatter plots of reaction rate versus mixture fraction do not reveal diffusion flame structures and confirm that the partially premixed configuration is dominant for all flames measured at the University of Twente: enough mixing occurs between the fuel injection and the combustion zone to provide premixing.

Figure (8.14) shows an instantaneous solution of the vorticity modulus field. A high shear region is observed between the fresh gases streams issuing into the chamber and the CRZ, leading to coherent structures formed by the Kelvin-Helmholtz instability. However, no major vortical structures are found in the burnt gases region which is explained by two factors. First, the burnt gases are much more viscous than fresh gases as a result of the high temperature due to combustion, which dissipates rapidly the vorticity generated in the shear layers. Second, the density gradient encountered as one moves along a line of constant  $y$  coordinate from the liner wall towards the center of the burner is perpendicular to the pressure gradient along the burner (descending along the  $y$  coordinate). This creates the so-called baroclinic torque [91], as a result of which the low-density layer is accelerated with respect to the high-density fresh gases, creating vorticity in the opposite sense as the one created by the vortex shedding from the wedge. Also, gas expansion due to combustion generates vorticity in the same sense as the baroclinic torque. This leads to the suppression of the vortex shedding process.

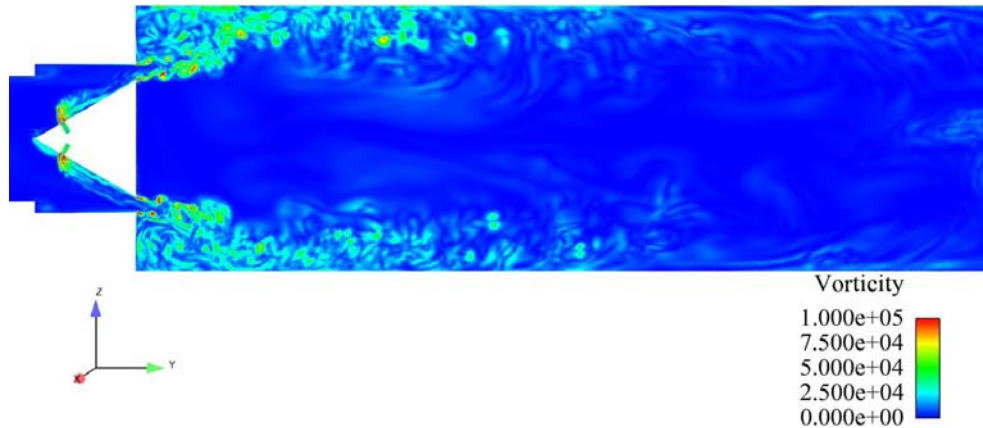


**Figure 8.14:** Cut of an instantaneous vorticity modulus field of Simulation 1 in hot flow at the middle plane ( $x = 0$ ).

### Development of the thermo-acoustic instability

After the flame is initialized, it starts stabilizing its position but it also starts oscillating. Fig.(8.15) displays time traces of total heat release and of pressure at the location of pressure probe 4. An unstable mode develops rapidly. The main mode frequency is at 305 Hz.

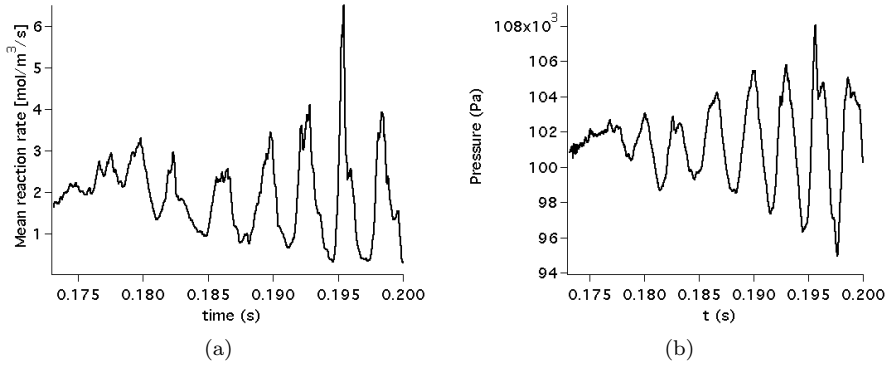


**Figure 8.15:** Time signals of (a) Mean reaction rate and (b) Pressure at probe 4, showing the onset of a CI in Simulation 1.

Figure (8.16) shows a sequence of instantaneous temperature field and reaction rate isocontours, where the onset of a thermo-acoustic instability is observed. Fig.(8.16(a)) shows a flame front which is perturbed by an incoming acoustic wave which accelerates the fresh gases, leading to a mushroom-like shape of the flame above the wedge. The vortices push the burnt gases towards the liner walls, and the flame is able to propagate to the fresh gases in the CORZ, as seen in Fig.(8.16(b)). The non-steady heat release rate of the flame leads to acoustic waves that grow in amplitude, leading in turn to larger flow oscillations that perturb the flame front even more, as seen in Fig.(8.16(c)). Finally, the flow oscillations are so large that a first flashback of the flame towards the upstream duct is observed, as shown in Fig.(8.16(d)).

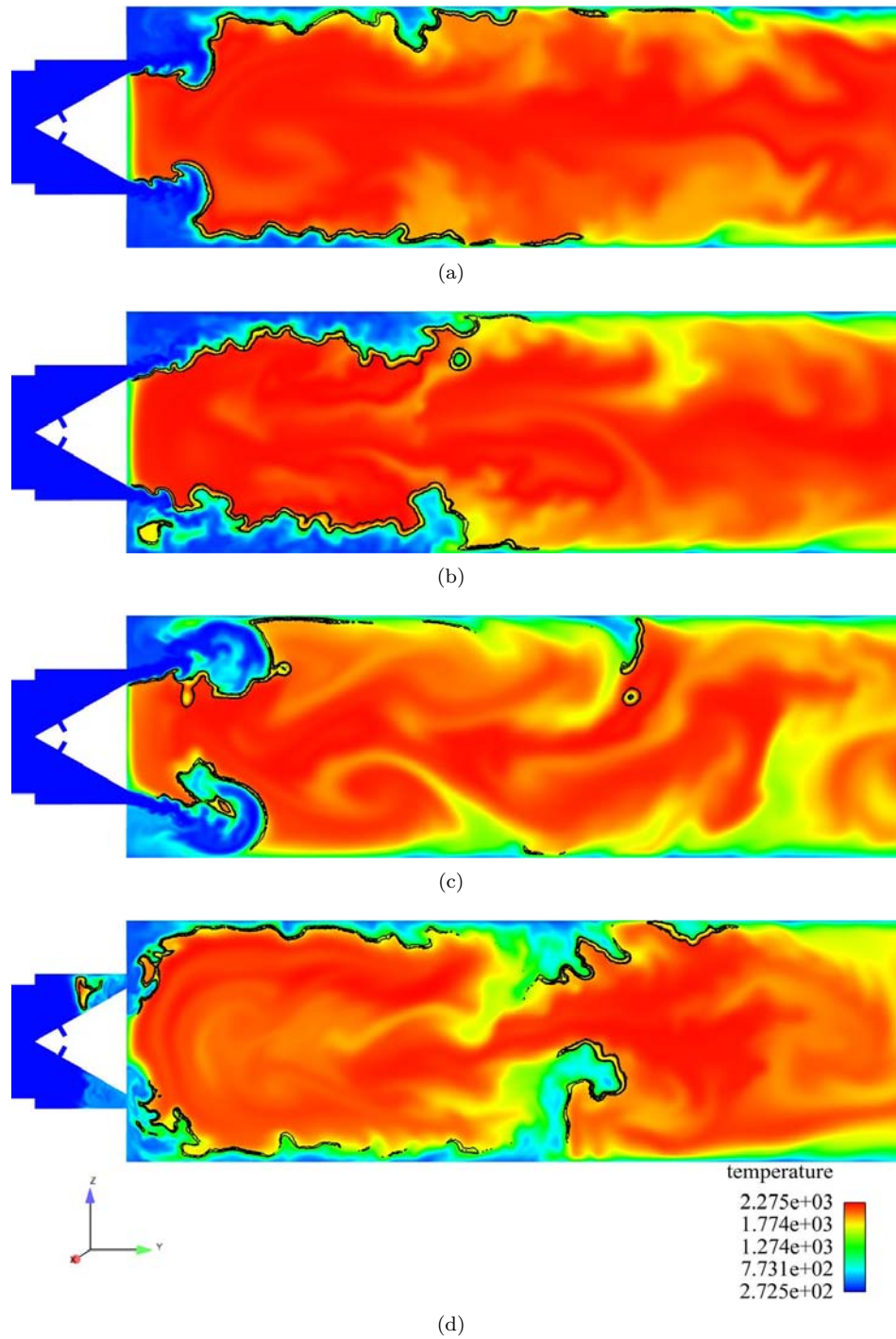


**Figure 8.16:** Sequence of instantaneous temperature fields and reaction rate isocontours showing the onset of the thermo-acoustic instability. Times (s): a) 0.181, b) 0.183, c) 0.188, d) 0.190.

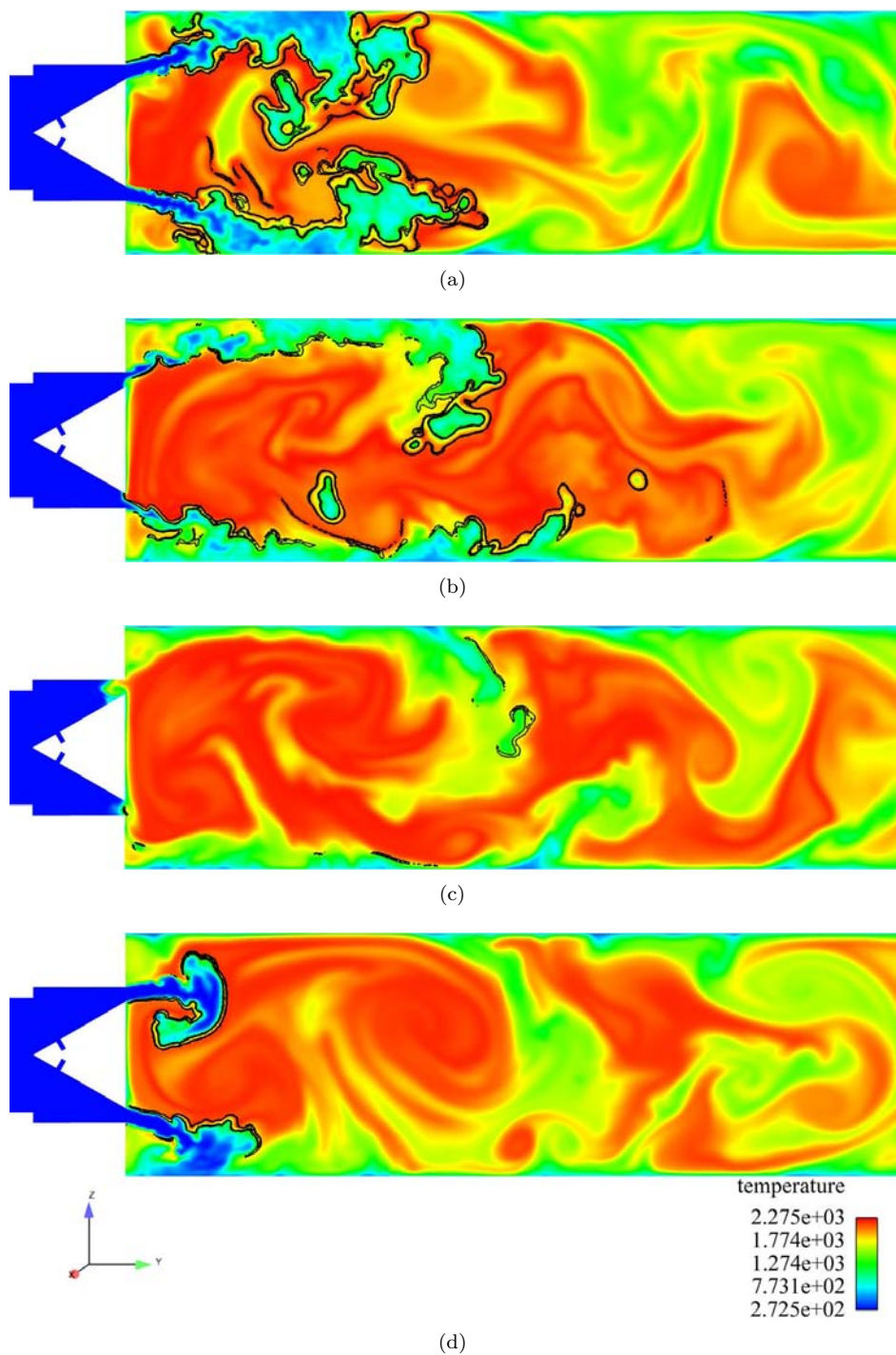
### Limit-cycle of the thermo-acoustic instability

Once the flame starts to oscillate, the amplitude of the oscillations grows in time until a steady-state oscillatory behaviour is reached, referred to as limit cycle-oscillations (LCO), where the instability is self-sustained but does not grow anymore, as seen in Fig.(8.20). Fig.(8.17) shows a sequence of instantaneous temperature field and isocontours of reaction rate over one period of the LCO at 305 Hz. The flame is stabilized by the hot burnt gases trapped in the CRZ and CORZ, which ignite the fresh gases as they enter the chamber, as seen in Fig.(8.17(a)). This double stabilization leads to a flame which is shorter than it would be if it was only stabilized by the CRZ, and the flame becomes compact, as the heat release takes place in a short region compared to a characteristic acoustic wavelength of the combustor. The consequence is that the combustor is more prone to the development of a thermo-acoustic instability. The unsteady heat release of the flame might feed energy on the acoustic field if both heat release and pressure fluctuations occur in phase locally, which excites one (or more) acoustic modes of the combustor. This is exactly what is happening in this simulation (and in the experiment as a matter of fact). This corner flame-trapping process and its impact on combustion stability was reported by Huang [65].

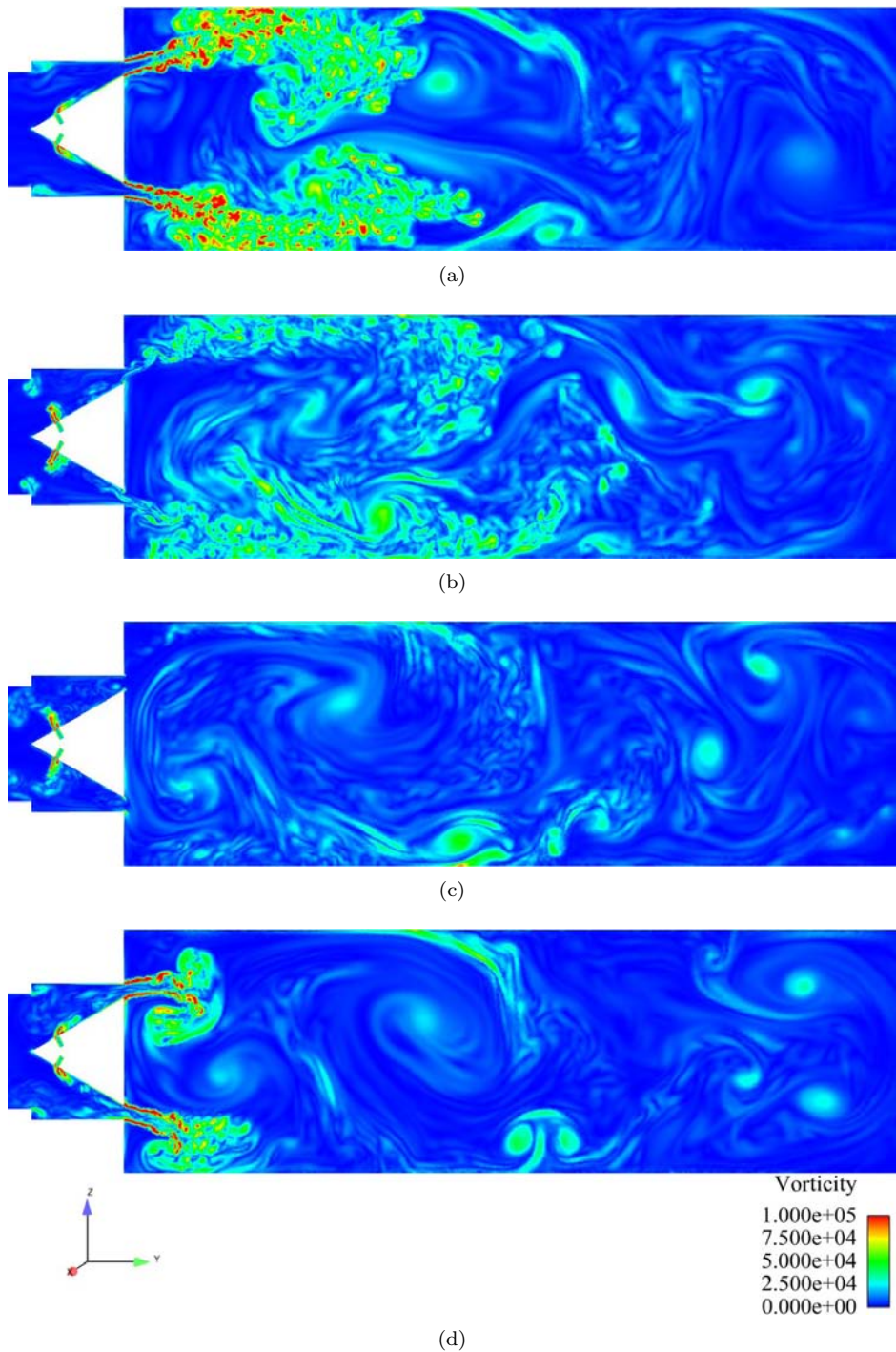
Figures (8.17(a)) to (8.17(d)) show the flame oscillations as the fresh gases are pulsed into the chamber by the velocity oscillations induced by acoustics. Velocity oscillations are of the order of the mean velocity, leading to flow reversal in some cases, and flashbacks of the flame through the gaps. At this point, all the fuel available in the chamber has been consumed, and no flame is observed. Only burnt gases remain in the chamber so there are no chemical reactions anymore, as seen in Fig.(8.17(c)).

Figure (8.18) shows a sequence of vorticity modulus fields corresponding to the same time instants as Fig.(8.17), where the large flow velocity oscillations are readily observed. The fresh gases are forced at high velocity into the chamber in a pulsed manner, leading to the formation of the strong shear layers observed in Figs. (8.18(a)) and (8.18(d)).

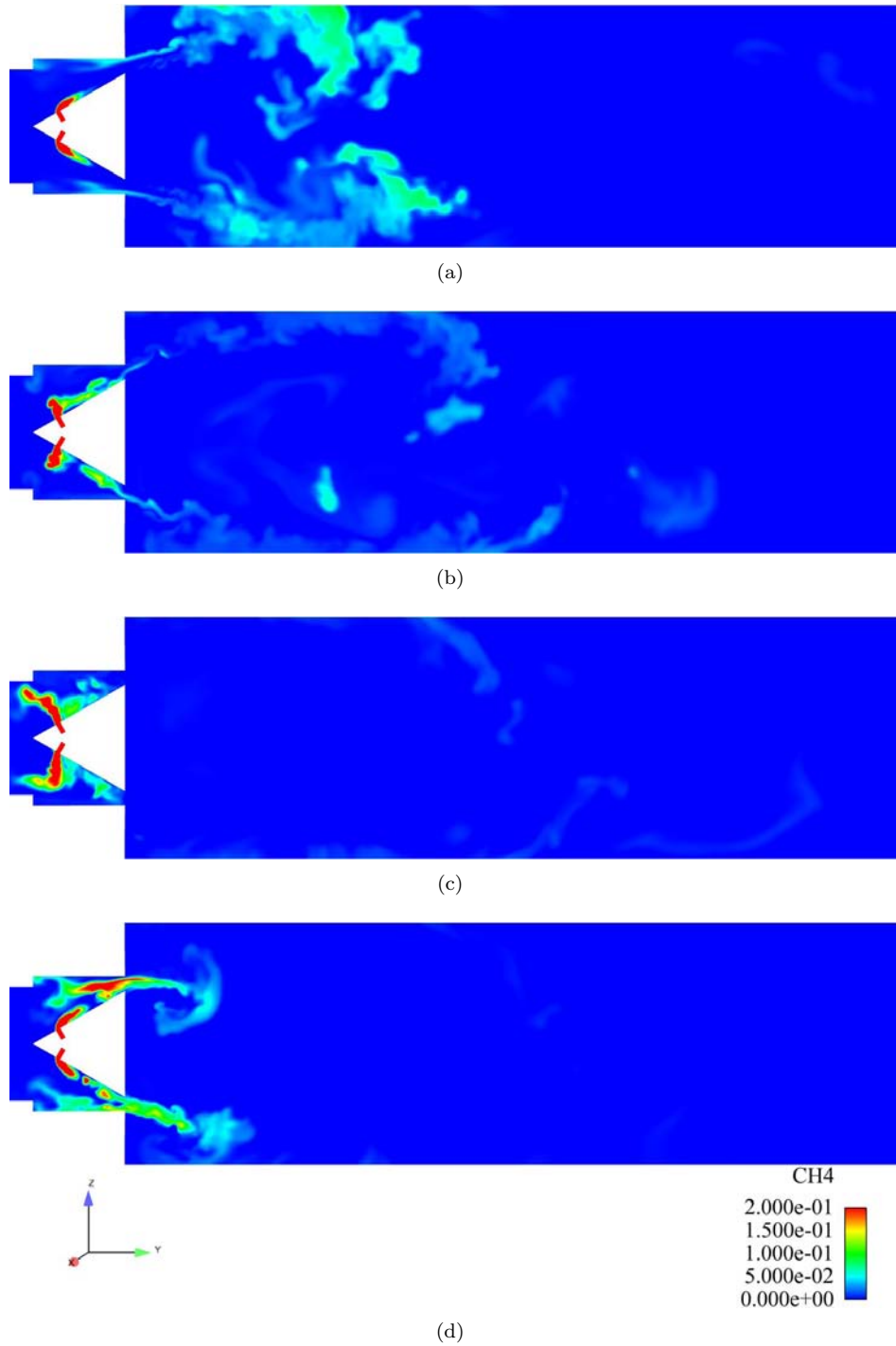
Likewise, Fig. (8.19) shows a sequence of instantaneous fuel mass fraction fields. During a cycle of the LCO, reactive mixture is forced into the chamber in a pulsed manner also, where it burns across the flame front. As the flow accelerates again due to the acoustic velocity oscillations all the fuel enters the chamber, where it burns. This unsteady fuel injection in the chamber is the reason of the oscillatory heat release rate in this case [93]. We will see that it has two sources: (1) the injected fuel flow rate is sensitive to the pressure oscillations and (2) the jets in cross flow (JICF) of methane in the air stream change direction when the air speed changes (see Fig.(8.19(c))), leading to fuel accumulation upstream of the wedge where the air cavity acts as a storage duct of the premixing gases.



**Figure 8.17:** Sequence of instantaneous temperature fields and reaction rate isocontours showing the flame oscillations over a full period of the LCO. Times (s): a) 0.241, b) 0.242, c) 0.243, d) 0.244.



**Figure 8.18:** Sequence of instantaneous vorticity modulus fields showing the flow oscillatory behaviour over a full period of the LCO. Times (s): a) 0.241, b) 0.242, c) 0.243, d) 0.244.



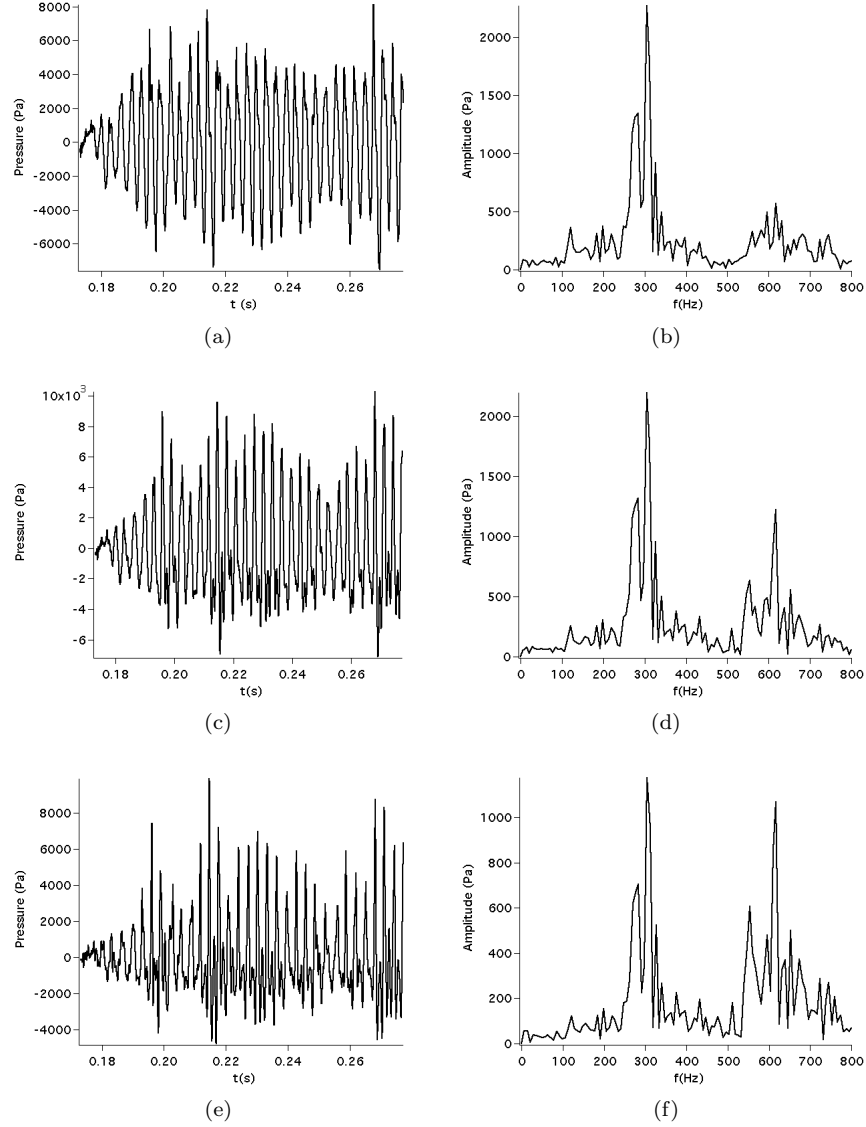
**Figure 8.19:** Sequence of instantaneous fuel mass fraction fields showing the oscillations in flow composition over a full period of the LCO. Times (s): a) 0.241, b) 0.242, c) 0.243, d) 0.244.

Figure 8.20 shows temporal pressure fluctuations signals recorded during the simulation at locations corresponding to probes 4, 5 and 6, as well as their Fourier Transforms. As shown, the amplitude of the pressure fluctuations grows in time in a first stage, which corresponds to the linear regime. In a latter stage, the amplitude of the fluctuations stops growing. This saturation of the pressure fluctuations amplitude is due to non-linear effects. Beyond a certain threshold, an augmentation in the amplitude of the acoustic oscillations is not followed by the corresponding fluctuation in heat release and, eventually, the gain in acoustic power from the flame matches the acoustic losses across boundaries, leading to a limit cycle. Another way to state this is that the LCO is not due to a saturation of the acoustic field but to a saturation of the unsteady combustion process: when combustion completely stops at one point of the cycle (Fig.(8.17(c))), the instability is not fed any more.

The amplitude of the oscillations predicted by LES is of the order of 4000 Pa, which is equivalent to a sound pressure level (SPL) of  $\sim 165$  dB within the burner (taking  $20\mu\text{Pa}$  as the reference pressure), which is representative of the noise encountered in unstable gas turbines. It is readily seen that such noise is unacceptable, since it leads to a deficient combustion performance, induces thermo-mechanical fatigue of the structural components and is harmful for humans.

The Fourier Transforms of the pressure signals show a dominant frequency peak of the pressure fluctuations at  $\mathbf{f}_1 = 305 \text{ Hz}$ . This is the frequency of the LCO, since it is the dominant frequency of the pressure fluctuations, and the frequency of oscillations of the flame. A secondary peak appears at a frequency of  $\mathbf{f}_2 = 617 \text{ Hz}$ .

Having computed a LCO containing two frequencies (305 and 617 Hz) is a first interesting result. The next question is to know where these modes come from. The combination of spectral analysis of LES results and acoustic computation with AVSP allows to identify the nature of the two unstable modes observed in Fig. 8.20: they are the second and third acoustic modes of the experimental set up. To demonstrate this, a collection of instantaneous LES solutions was generated and the Power Spectral Density (PSD) of the pressure field was calculated for the two peak frequencies. Fig. 8.22 shows longitudinal profiles along the combustor of the mode shapes given by LES and compares their structures with the acoustic modes given by AVSP. AVSP was used to compute the modes of the complete combustor: the sound speed field for this computation was given by the average LES data. No active flame effect was included. AVSP predicts longitudinal modes at 186 Hz (mode 1), 337 Hz (mode 2), 691 Hz (mode 3) (Table 8.4). Fig. 8.21 displays the structure of these modes ( $|p'|$  versus spatial location), which correspond to a quarter wave, three-quarters wave and five-quarters wave modes respectively. The 186 Hz mode is not observed in the LES. The 305 Hz mode observed in the LES has a structure which is very close to the second acoustic mode computed by AVSP. The 617 Hz mode



**Figure 8.20:** (a), (c), (e) Temporal pressure signals recorded during the simulation corresponding to pressure probe locations 4, 5 and 6 respectively, as shown in Fig.(7.4). (b), (d), (f) Fourier Transforms of the pressure signals from probes 4, 5 and 6 respectively.

obtained in the LES is close to the third acoustic mode and exhibits a node before the wedge ( $x = 0.1$  m) and a second node in the chamber ( $x = 0.52$  m). The slight discrepancies between the LES and the acoustic modes may be

due to the treatment of the burner outlet at  $x = 1.05$  m and to the fact that no active flame model was included in the computation of the acoustic modes. The agreement in terms of frequencies and mode shapes confirms that the combustor resonates on the second and third acoustic modes of the whole set up and that LES and acoustic analysis match well. The unstable mode at 617 Hz might also be the result of a frequency-doubling of the first unstable mode due to non-linear effects [77], further studies are needed to identify the origin of this mode.

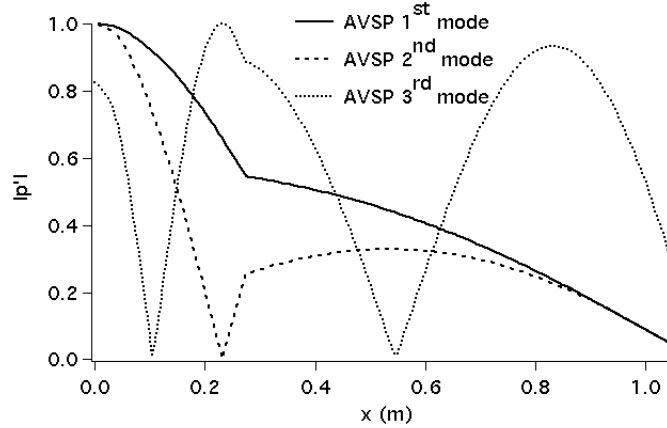


**Figure 8.21:** Spatial structure of the first three acoustic eigenmodes computed with AVSP using an averaged LES solution of Simulation 1.

Order of the mode	Frequency (Hz)
1	185.5
2	336.7
3	691.5

**Table 8.4:** Acoustic eigenfrequencies of the burner given by acoustic analysis (AVSP).

As a result of the acoustic pressure oscillations, the air and fuel mass inlets also pulsate. Fig 8.23 shows the temporal evolution of air and fuel mass flow rates, normalized by their mean values. The amplitude of the inlet mass flow rates fluctuations grows in time following the evolution of the pressure oscillations within the combustor. When the LCO are established, fluctuations of inlet mass flow rates of  $\sim 20\%$  with respect to their mean values are observed. As explained before, fuel inlet mass flow rate fluctuations contribute to the development of thermo-acoustic instabilities. Indeed, a pulsating fuel inlet line creates mixture inhomogeneities that, when convected to the flame front, leads to heat release rate fluctuations [133]. Note that, in the LES, the response of the air and fuel lines are controlled by the NSCBC boundary treatment which

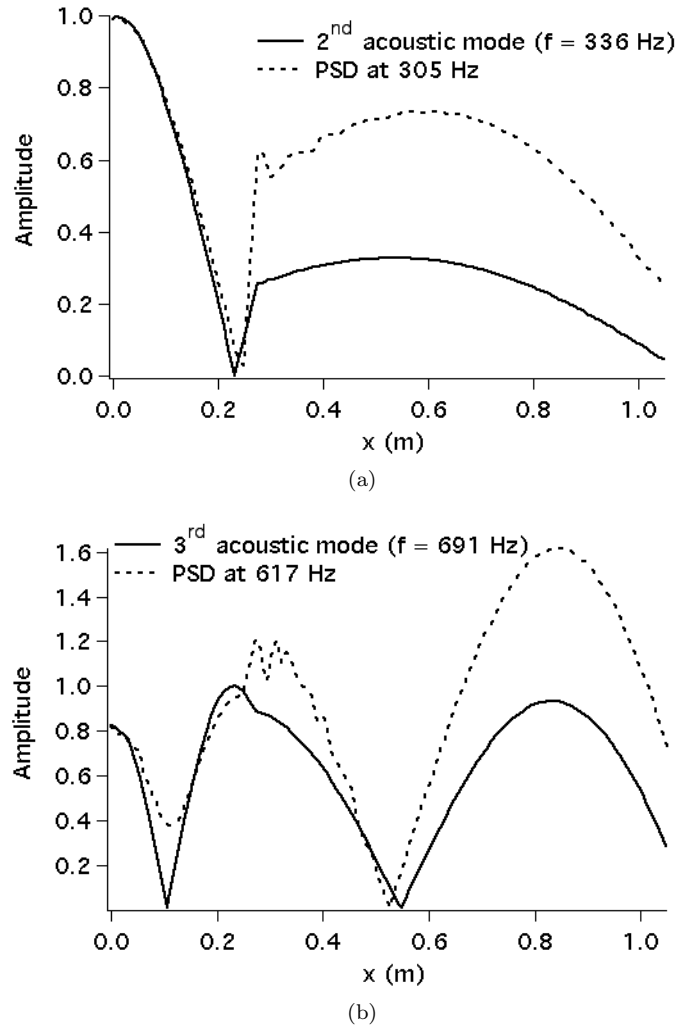
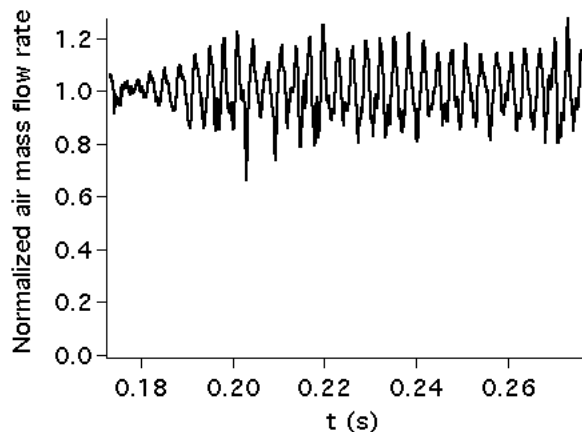


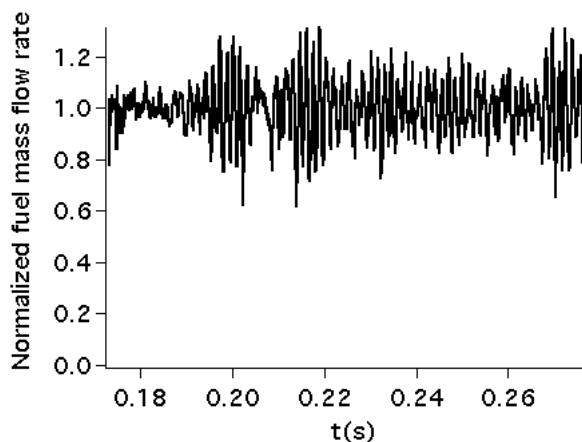
**Figure 8.22:** Longitudinal profiles along the combustor of the normalized pressure fluctuations. Dashed line: spectral analysis of the LES data of Simulation 1 during the LCO. Solid line: acoustic code predictions (AVSP).

imposes a complex impedance. Sections 8.4 and 8.5 will show the effect of these impedances.

In order to confirm the existence of the thermo-acoustic instability, a last verification was performed using Rayleigh's criterion. Fig. 8.24 shows pressure fluctuations  $p'$  at probe 4 (expressed as a percentage of the mean pressure) and a volume-averaged Rayleigh parameter  $R$ , calculated as  $R(t) = \int_V p'q' dV$ ,



(a) Air mass flow rate



(b) Fuel mass flow rate

**Figure 8.23:** Temporal evolution of the air and fuel inlet mass flow rates during the simulation normalized by their respective mean values.

where  $V$  is the volume of the domain and  $q'$  is a non-dimensional reaction rate normalized by its mean value. The Rayleigh criterion is one measurement of the coupling between pressure and heat release oscillations [47, 109, 124]. It is positive when energy is fed into the acoustic field and viceversa. Here,  $R$  is positive most of the time: there is a net energy transfer from combustion to the acoustic field which is the reason why the thermo-acoustic instability is self-sustained. The Rayleigh criterion is, however, only one source term in the acoustic energy equation of the whole combustor [110, 111], and acoustic losses are also important.

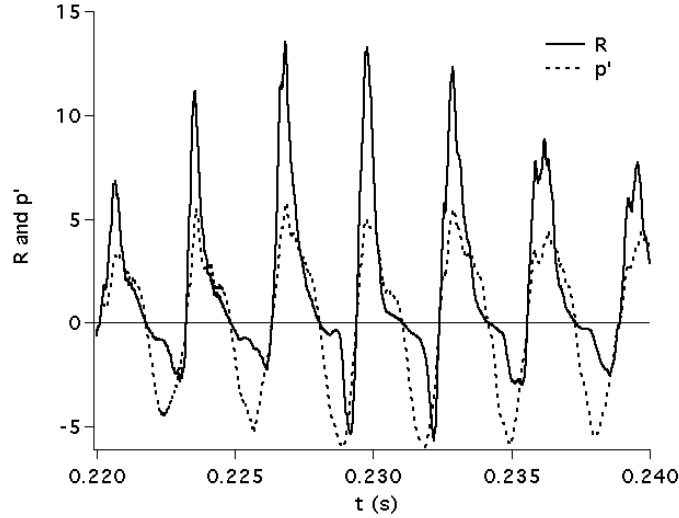


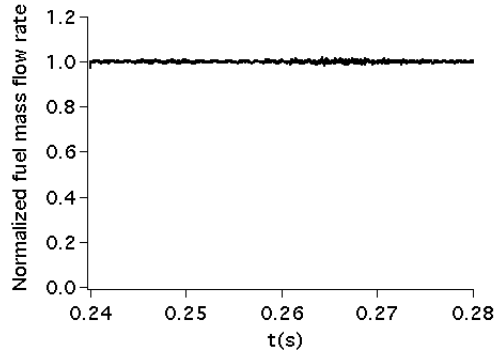
**Figure 8.24:** Rayleigh parameter and relative pressure fluctuation time signals of Simulation 1.

## 8.4 Simulation 1.1: influence of fuel inlet conditions

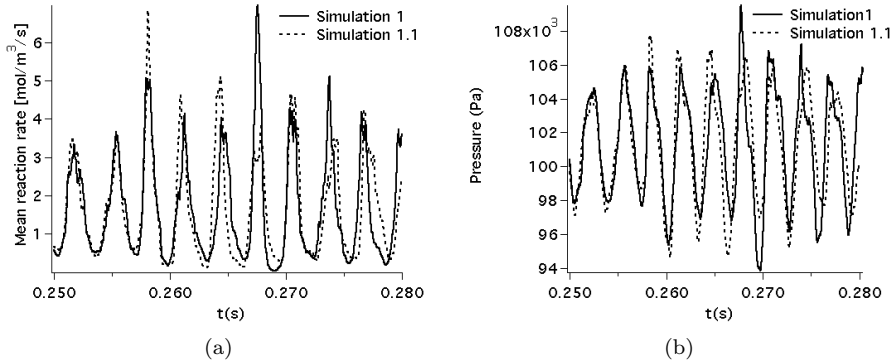
In order to assess the influence of the fuel lines impedance on the burner stability, a simulation was performed (Simulation 1.1) where the fuel inlet relaxation coefficient  $K_{fuel}$  value was increased from  $10^3$  (as it was set in Simulation 1) to  $10^5$ . This value is high enough to ensure that the fuel inlet mass flow rate is almost fixed and fluctuates very slightly around its mean value, as seen in Fig.(8.25) (to be compared with Fig.(8.23(b)) for the reference case).

Fig. 8.26(a) shows a comparison between the temporal evolution of mean reaction rate for Simulations 1 and 1.1. Only small discrepancies in mean reaction rate (proportional to heat release rate) are observed when the fuel inlet mass flow rate is fixed.

Fig. 8.26(b) shows a comparison between the time pressure signals at the location of the pressure probe 4 for Simulations 1 and 1.1 (see Table 8.2). As in the previous figure, no major differences are found with respect to Simulation 1. The pressure peaks of Simulation 1.1 coincide well with the ones predicted in Simulation 1.



**Figure 8.25:** Temporal evolution of the fuel inlet mass flow rate normalized by its mean value, corresponding to Simulation 1.1. A high relaxation coefficient is set on the fuel inlets to impose a constant fuel inlet mass flow rate.



**Figure 8.26:** Comparison of (a) Mean reaction rate temporal evolution and (b) Pressure signal at probe 4, between simulations 1 (solid lines) and 1.1 (dashed lines).

Therefore we can conclude that the fuel inlet impedance is a parameter with little effect, if any, on combustion stability for the configuration studied. The fuel flow rate can be sensitive or not to pressure oscillations: the instability does not depend on it. This does not prove that unsteady mixing is not important. As shown in Fig.(8.19), fuel does accumulate upstream of the wedge at certain instants and the effect of the acoustic pulsations is to inject vortices and mixed (or partially premixed) reactants in the chamber. However, that is independent of the fuel flow rate oscillations. This is a useful piece of information, even experimentally, because it eliminates one potential source for instabilities: the pulsation of flow rates in the fuel lines.

## 8.5 Simulation 1.2: influence of air inlet conditions

The influence of the air inlets impedance on the LCO features was tested as well. Simulation 1.2 was performed using the exact same parameters as in Simulation 1, except for an increased air inlet relaxation coefficient  $K_{air}$ , which was set to  $10^5$ . This allows to fix the air inlet mass flow rate, as shown in Fig.(8.27) (to be compared with Fig.(8.23(a)) for the reference case), so that the effect of air inlet mass flow rate fluctuations can be assessed.

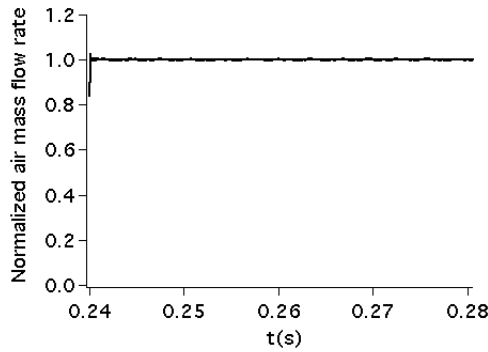


**Figure 8.27:** Temporal evolution of the air inlet mass flow rate normalized by its mean value, corresponding to Simulation 1.2, where a high relaxation coefficient is set on the air inlets.

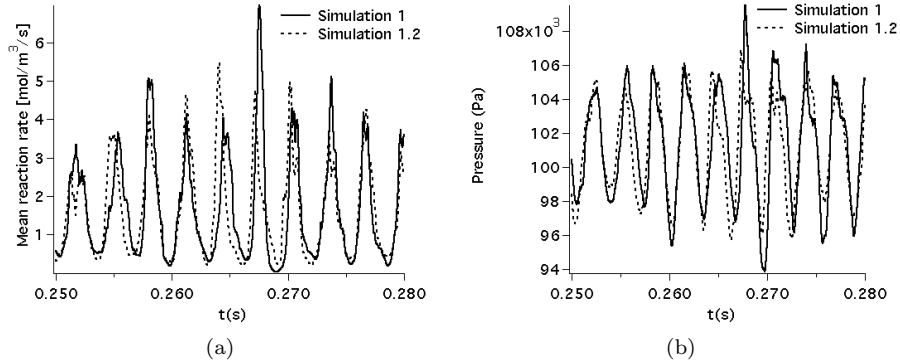


**Figure 8.28:** Comparison of (a) Mean reaction rate temporal evolution and (b) Pressure signal at probe 4, between simulations 1 (solid lines) and 1.2 (dashed lines).

Figure 8.28 shows a comparison of time signals of mean reaction rate and local pressure between simulations 1 and 1.2. Very small differences are seen

between both simulations, the amplitude of the LCO is not amplified nor decreased. Air inlet mass flow rate fluctuations are then ruled out as well as responsible for the heat release oscillations, showing that the problem is correctly closed acoustically: boundary conditions are imposed far enough from the combustor to have a limited impact on the self-excited modes.

## 8.6 Simulations 1.3 and 1.4: influence of mesh

The computational mesh used throughout this work was designed to be able to resolve key aspects of the flow such as fuel/air mixing and the flame features properly. When discretizing the computational domain one might tend to impose a very small cell size so that all the flow features are correctly resolved. This is not always possible due to limited computational resources and a trade-off between accuracy and computational cost is usually made. However, mesh independency of the results must be ensured if trustworthy results are to be produced.

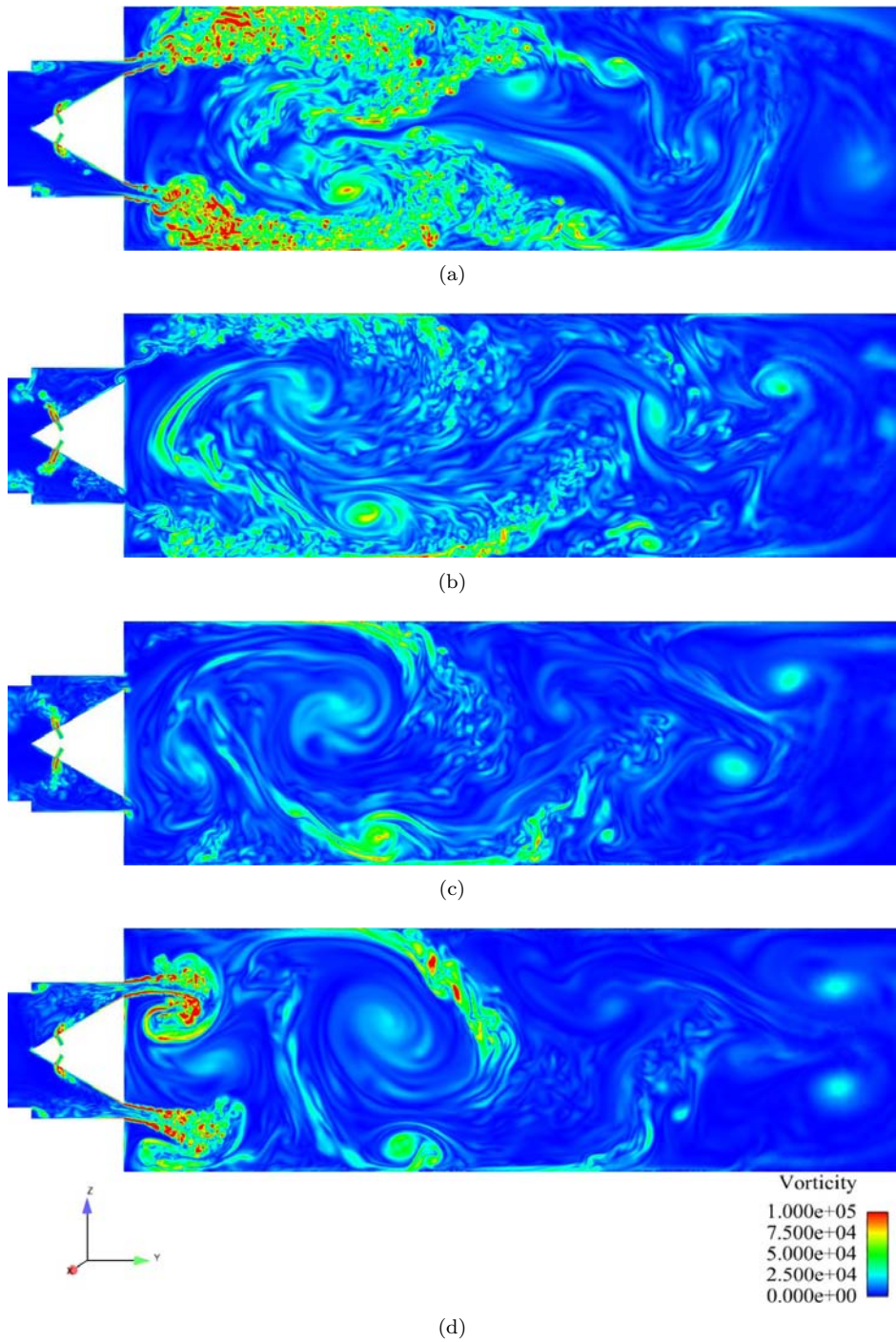
For this exercise, a simulation of the reference case OP1 was first performed using a refined mesh (Simulation 1.3). Cell size was reduced from 0.4 mm to 0.25 mm in the flame zone and the resulting number of nodes in the mesh went up from 1.1 M to 2.8 M. The minimum cell volume decreased from  $V_{min} = 2.444 \cdot 10^{-13} \text{ m}^3$  in Simulation 1 to  $V_{min} = 9.366 \cdot 10^{-14} \text{ m}^3$  in Simulation 1.3. Consequently, the time step of the simulation also decreased, since it is imposed by the CFL condition [34], as in Eq. 8.8.  $|\vec{V}|$  and  $c$  are local values of the modulus of the velocity vector the speed of sound, respectively. AVBP is a compressible code with explicit time integration, thus the CFL condition must be fulfilled in order for the numerical integration to be stable. The CFL number is set to 0.7 here.

$$\Delta t_{max} = CFL \cdot \frac{V_{cell}^{1/3}}{\left(|\vec{V}| + c\right)} \Big|_{min} \quad (8.8)$$

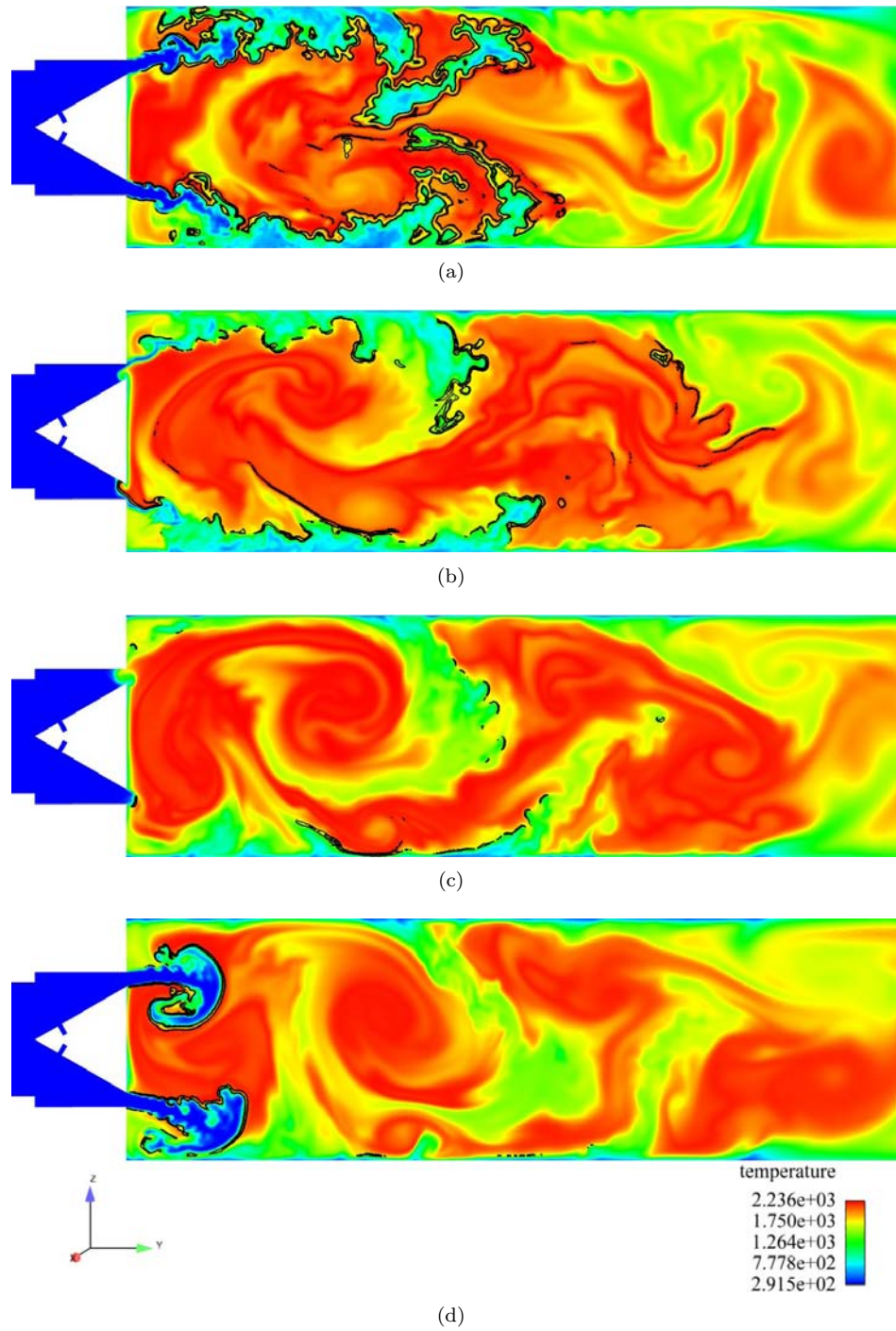
Figure 8.29 shows a sequence of vorticity modulus fields during a period of the LCO in Simulation 1.3. The flow is self-excited as observed in Simulation 1. As the fresh gases enter the chamber through the gaps, strong shear layers are created, leading to the creation of many small vortices that enhance the ignition of the fresh mixture by the hot burnt gases. The refined mesh used for this simulation allows to capture a wider variety of turbulent structures than in Simulation 1.

Figure 8.30 shows a sequence of temperature fields and reaction rate isocontours during a period of the LCO in Simulation 1.3. As observed in Simulation

1, the fresh gases are ignited by the hot burnt gases in the CRZ and CORZ as they enter the downstream duct through the gaps. The shear layers between the fresh gases jets and the hot recirculating gases create turbulence which leads to a highly wrinkled flame front. The mesh refinement in the flame zone, with respect to the mesh of Simulation 1, allows to obtain a turbulent flame front which is distorted by smaller eddies, leading to an augmentation of the flame surface area, and to a decreased thickening factor for the Thickened Flame LES (TFLES) model.



**Figure 8.29:** Sequence of instantaneous vorticity modulus fields showing the flow oscillatory behaviour over a full period of the LCO for Simulation 1.3. Times (s): a) 0.2422, b) 0.2429, c) 0.2436, d) 0.2443.



**Figure 8.30:** Sequence of instantaneous temperature fields and reaction rate isocontours showing the flame oscillations over a full period of the LCO for Simulation 1.3. Times (s): a) 0.2422, b) 0.2429, c) 0.2436, d) 0.2443.

Figures (8.31) and (8.32) shows a comparison of instantaneous thickening factor fields and scatterplots of  $\mathcal{F}$  versus mixture fraction  $Z$  between Simulations 1 and 1.3, respectively. When the cell size of the computational grid in the flame zone is reduced from 0.4 mm to 0.25 mm, the thickening factor gets proportionally reduced from typical values of around 3 in Simulation 1 to values around 1.5 in Simulation 1.3.

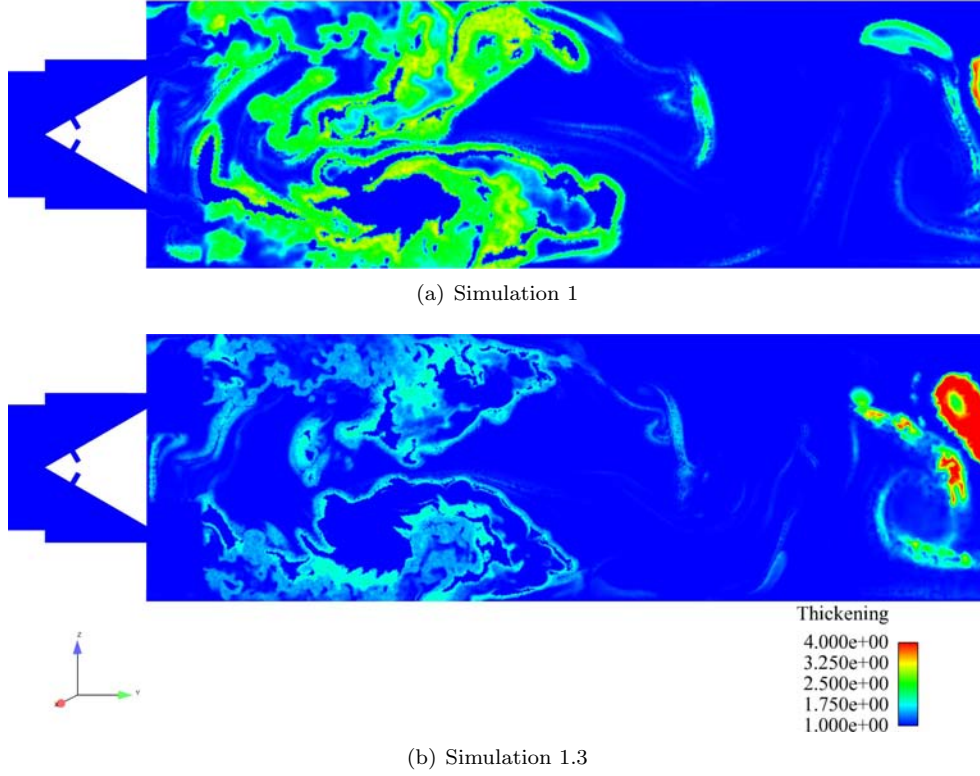


**Figure 8.31:** Instantaneous thickening factor field corresponding to (a) Simulation 1 and (b) Simulation 1.3 at the time instant  $t = 0.242$  s.

Figure 8.33(a) shows a comparison of temporal evolution of mean reaction rate between simulations 1 and 1.3. The agreement is good at the beginning but differences appear as time goes by. In particular, sharper and more localised in time mean reaction rates are found in Simulation 1.3 with respect to Simulation 1, whose amplitude is lower and more distributed in time. The differences are ascribed to the fact that, due to the finer grain turbulence captured by the refined mesh, the reactants burn faster as a result of the higher flame surface area. The spiky mean reaction rate temporal evolution leads to pressure oscillations whose amplitude is somewhat higher than in Simulation 1, as seen in Fig. 8.33(b). Also, the frequency of the LCO seems to increase slightly.

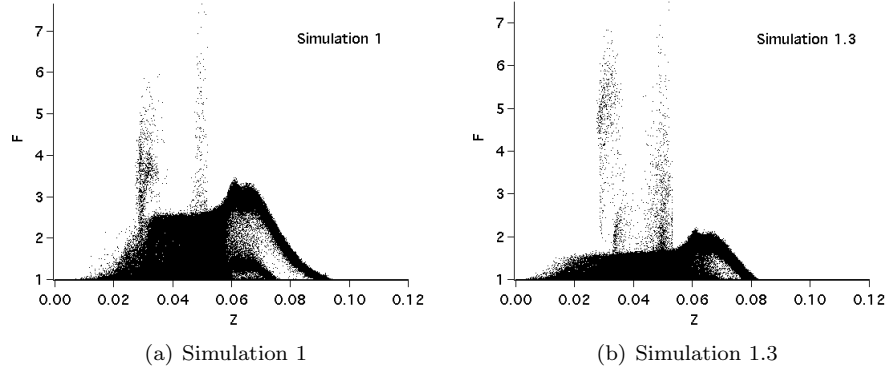


**Figure 8.32:** Scatterplot of the thickening factor  $\mathcal{F}$  versus mixture fraction  $Z$  corresponding to instantaneous solutions of (a) Simulation 1 and (b) Simulation 1.3 at the time instant  $t = 0.242$  s.

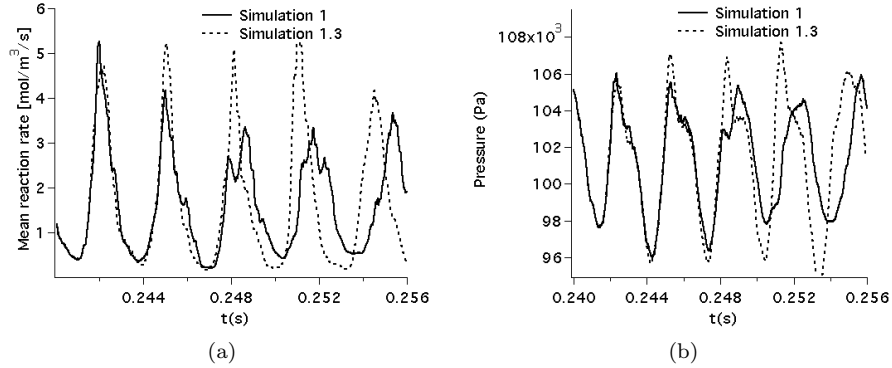


**Figure 8.33:** Comparison of (a) Mean reaction rate temporal evolution and (b) Pressure signal at probe 4, between simulations 1 (solid lines) and 1.3 (dashed lines).

Since Simulation 1 and 1.3 did not demonstrate a full mesh independency, an additional simulation (Simulation 1.4) was performed using the same parameters as in Simulation 1.3 but using an even more refined mesh. In Simulation 1.4, a mesh with 4.4 M nodes was used. The cell size in the flame region was set to 0.2 mm and the minimum cell volume is  $V_{min} = 9.358 \cdot 10^{-14} \text{ m}^3$ . This mesh study allows to determine the number of mesh points needed to attain a mesh-independent solution. A comparison of mean reaction rate and pressure signal at the location of pressure probe 4 between Simulations 1.3 and 1.4 is shown in an independent figure (Fig. 8.34) for the sake of clarity. The results of the LES show slight discrepancies when the computational mesh is refined from 2.8 M to 4.4 M nodes. Even though differences in the instantaneous solution seem to

appear after 3 acoustic periods (from  $t = 0.250$  s), no change on the amplitude or frequency of the LCO is observed. This indicates that, beyond this degree of refinement, no quality improvement of the results is to be expected with an increase in the number of mesh points.

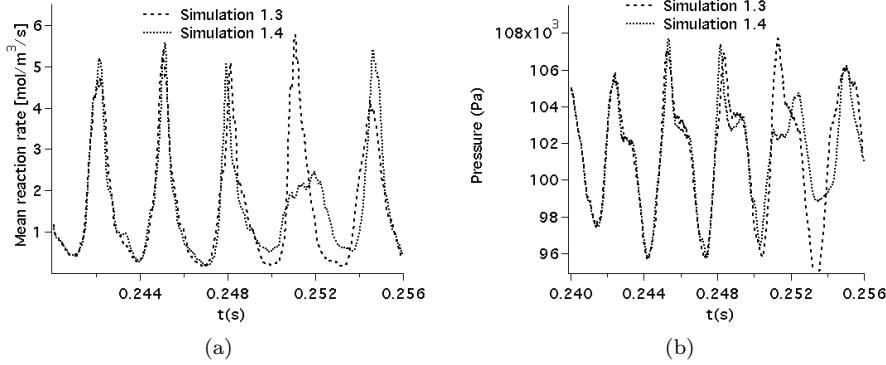


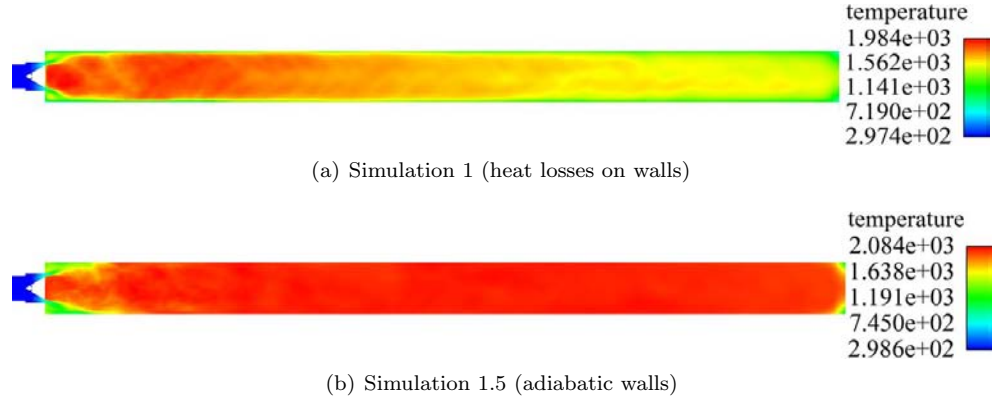
**Figure 8.34:** Comparison of (a) Mean reaction rate temporal evolution and (b) Pressure signal at probe 4, between simulations 1 (solid lines) and 1.3 (dashed lines).

## 8.7 Simulation 1.5: influence of adiabaticity

A simulation corresponding to OP1 was performed (Simulation 1.5) using the exact same parameters as in Simulation 1, except for the boundary conditions on the burner walls. Adiabatic boundary conditions were used on the wedge and the downstream duct walls in Simulation 1.5, instead of the heat losses imposed so far. This allows to observe the effect that heat losses have on the computation of LCO.

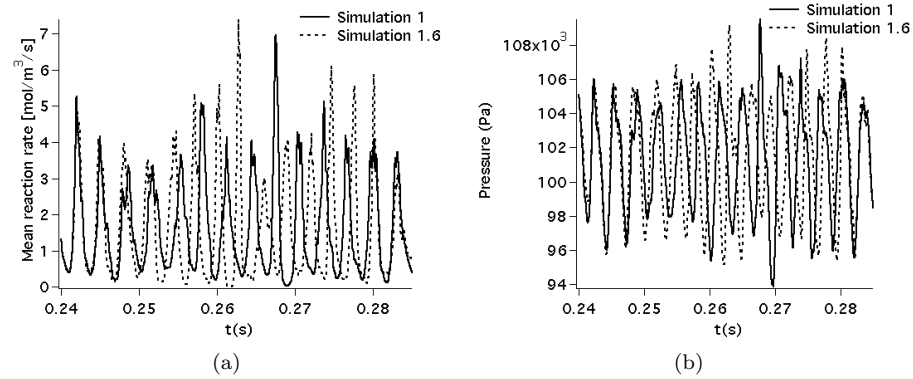
As expected, adiabatic walls prevent the burnt gases to lose heat along the downstream duct as they flow towards the burner outlet. Fig. 8.35 shows mean temperature fields of Simulations 1 and 1.5. When adiabatic walls are imposed, no heat losses from the burnt gases to the walls occur along the downstream duct, leading to temperature differences of the burnt gases of up to  $\sim 400$  K at the burner outlet between Simulations 1 and 1.5.

Figure 8.36 shows a comparison of temporal mean reaction rate and pressure at the location of pressure probe 4 between Simulations 1 and 1.5. Imposing adiabatic walls in the simulation does not have any effect on the amplitude of the computed LCO, however, a phase shift in the mean reaction rate and pressure oscillations is observed. The higher burnt gases temperatures obtained in Simulation 1.5 leads to a higher speed of sound along the downstream duct. As a consequence, a spectral analysis of the LES signals shows that the frequency



**Figure 8.35:** Comparison of averaged temperature fields between (a) Simulation 1 and (b) Simulation 1.5.

of the unstable mode increases from 305 Hz in Simulation 1 to **332 Hz** in Simulation 1.5.



**Figure 8.36:** Comparison of (a) Mean reaction rate temporal evolution and (b) Pressure signal at probe 4, between simulations 1 (solid lines) and 1.5 (dashed lines).

## 8.8 Simulation 1.6: influence of radiative heat losses

So far, conductive and convective heat losses of the burnt gases to the liner walls were taken into account. However, radiative heat losses were neglected. A new simulation (Simulation 1.6) similar to Simulation 1 was performed, but

radiative heat losses were included.

Accurate computations of radiative exchanges within gases is a complicated problem which involves the solution of the radiative transfer equation (RTE) [101]. Radiation emission and absorption must be accounted for, considering the directions of propagation (non-local exchanges) and the spectral dependence of the radiative properties. This problem constitutes a challenge in itself and, although technically possible to couple LES and detailed radiation computations [3, 4, 119], reduced models are used to ensure the best accuracy with an acceptable CPU time ratio between LES and radiation.

Here the optically thin limit (OTL) approximation is made, whereby the gases are supposed to be transparent to radiation. Radiation exchanges occur with the surroundings at temperature  $T_s$  (here the chamber walls): absorption within the gas is neglected. Also, the frequency dependence of the radiative properties is eliminated assuming grey gases with spectral-averaged properties. A source term  $\dot{S}_{rad}$  was added to the energy equation 6.19 accounting for the volumetric power loss due to radiative heat exchange between the hot burnt gases and the cold surroundings (the liner walls here) [133], and is computed as in Eq. 8.9:

$$\dot{S}_{rad} = -4\sigma (T^4 - T_s^4) \sum_{i=1}^{N_{spec}} (p_i a_{p,i}) \quad (8.9)$$

where  $\sigma = 5.669 \cdot 10^{-8} \text{ W/m}^2\text{K}^4$  is the Stefan-Boltzmann constant,  $T$  is the local gas temperature,  $T_s$  is the temperature of the surroundings,  $p_i$  is the partial pressure of species  $i$  and  $a_{p,i}$  is the Planck absorption coefficient of the grey gases for species  $i$ . Absorbing species are  $CO_2$  and  $H_2O$ . The Planck mean absorption coefficients are given in terms of a polynomial expression as follows:

$$a_{p,i} = \exp \left( C_0 + C_1 \cdot \ln(T) + C_2 \cdot [\ln(T)]^2 + C_3 \cdot [\ln(T)]^3 + C_4 \cdot [\ln(T)]^4 \right) \quad (8.10)$$

where the coefficients in Eq. 8.10 were taken from Gore et al.[59] and are summarized in Table 8.5.

Species	$C_0$	$C_1$	$C_2$	$C_3$	$C_4$
$H_2O$	278.713	-153.24	32.1971	-3.0087	0.104055
$CO_2$	969.86	-588.38	132.89	-13.182	0.48396

**Table 8.5**

The temperature of the walls is assumed constant and set to  $T_s = 550$  K, value estimated from available measurements performed at University of

Twente.

Note that the OTL approximation is not suitable for optically thick gases, such as in the presence of soot. In the LIMOUSINE test rig, no soot was observed. However, the downstream duct might be long enough ( $L_{dsduct} = 0.78$  m) for radiation absorption to become non-negligible in the  $y$  direction (along the burner). The assessment of the impact of the radiative model on the results is left for future studies.

Figure 8.37 shows the mean temperature field corresponding to Simulation 1.6. The additional heat losses due to radiation lead to a larger temperature decrease along the combustor. The temperature of the burnt gases at the burner outlet is  $\approx 300$  K lower than the one obtained in Simulation 1. The impact on the acoustics of the burner is summarized in Tab. 8.6, where the frequencies of the first three acoustic eigenmodes obtained with an averaged solution from Simulation 1.6 are shown. Somewhat lower frequencies are obtained due to the lower temperature, and therefore of the sound speed, of the burnt gases along the combustor. However, the differences in acoustic frequencies are small as there is only a significant temperature difference in the region near the burner outlet.

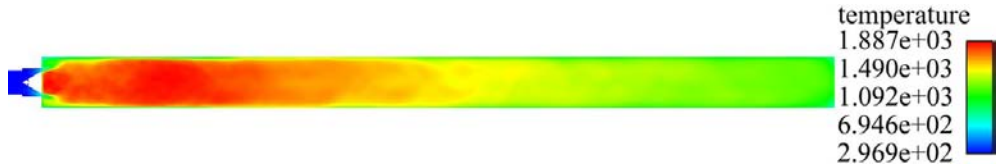


**Figure 8.37:** Mean temperature field corresponding to Simulation 1.6.

Order of the mode	Frequency (Hz)	Difference with Simulation 1 (Hz)
1	177.0	-8
2	330.0	-6
3	664.7	-27

**Table 8.6:** Acoustic eigenfrequencies of the burner given by acoustic analysis (AVSP) in Simulation 1.6.

Figure 8.38 shows a comparison between mean reaction rate and pressure signal at the location of pressure probe 4 between Simulations 1 and 1.6. The amplitude of the reaction rate and pressure oscillations is conserved, but both signals seem to shift apart very slowly with time. The frequency of the LCO predicted in Simulation 1.6 is **303 Hz**, which is only 2 Hz lower than the frequency of the unstable mode of Simulation 1. This difference is readily explained

by the decrease in the burnt gases temperature along the combustor due to radiative losses.

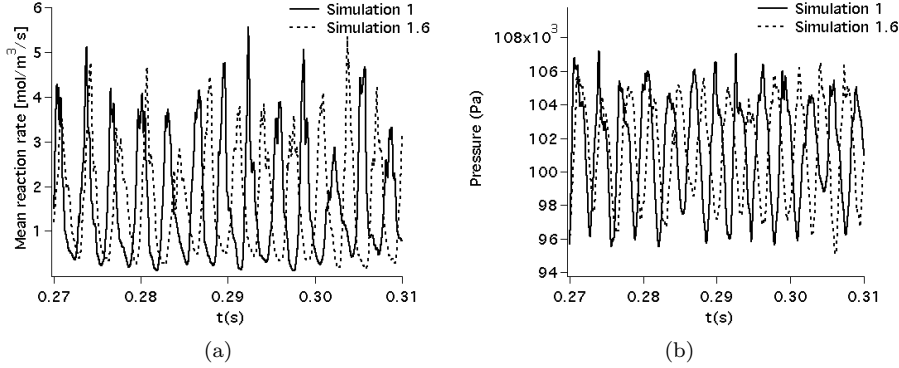


**Figure 8.38:** Comparison of (a) Mean reaction rate temporal evolution and (b) Pressure signal at probe 4, between simulations 1 (solid lines) and 1.6 (dashed lines).

## 8.9 Simulation 2: influence of the OP.

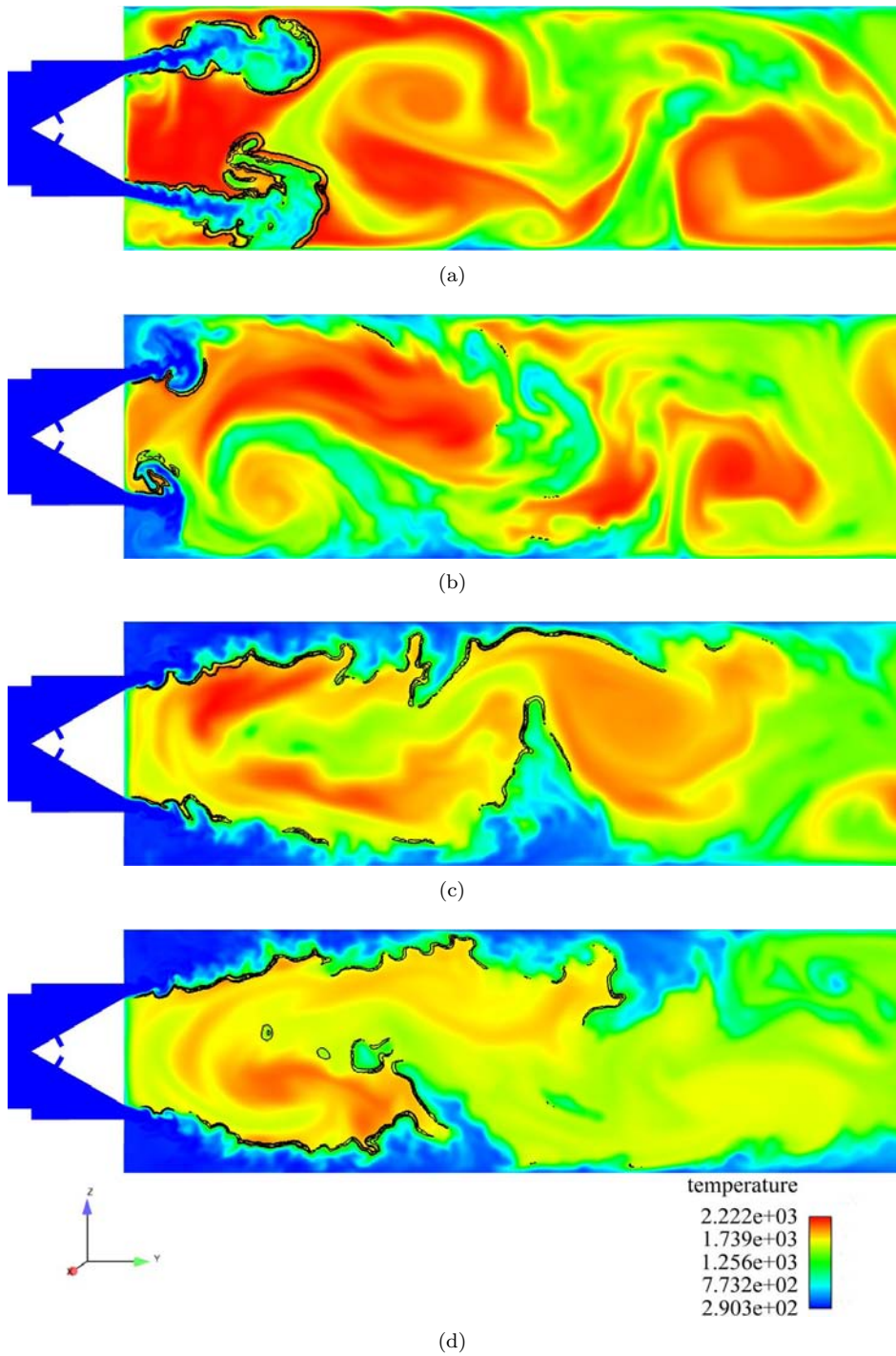
As seen in Fig. 7.5 stable combustion was observed when the burner was operated at the conditions of OP2. In order to shed some light on the physical phenomena responsible for the transition to stability in the LIMOUSINE burner, a simulation was performed reproducing the conditions at OP2, and the results are shown in the present section. Simulation 2 was initialized with a solution corresponding to Simulation 1, and only the air mass flow rate was changed to that of OP2, with an air factor  $\lambda = 1.8$ .

Figure 8.39 shows a sequence of instantaneous temperature fields and reaction rate isocontours corresponding to Simulation 2. It is observed that the flame behaviour changes along the sequence. Fig. 8.39(a) depicts an oscillating flame, corresponding to Simulation 2 before the transition to stability takes place. In the subsequent snapshots, it is seen that the flame stops oscillating and stabilizes above the wedge, where it remains. Position changes of the flame front still occur, but are due to turbulence, and not to a thermo-acoustic instability.

Different factors explain the transition to stable combustion. The increase in air factor  $\lambda$  from 1.25 in Simulation 1 to 1.8 in Simulation 2 has two immediate consequences. First, the flow velocity increases due to the increase in air inlet mass flow rate. Second, the turbulent flame speed of the mixture decreases, as a result of the decrease in global equivalence ratio within the burner (the fuel inlet mass flow rate is held constant). The fresh gases are now being squeezed

through the gaps into the downstream duct at an even higher mean velocity than before and, as a result, the hot burnt gases in the CORZ are blown away. Burnt gases are then replaced by cold fresh gases in the CORZ. Unlike in Simulation 1, the flame is not able to propagate upstream to the CORZ due to the increased flow velocity and the diminished flame speed. In this situation, the flame is only stabilized by the burnt gases in the CRZ, as seen in Fig. 8.39(d). The fresh gases jets issuing into the chamber are only ignited through their sides in contact with the CRZ, and not through both sides, as seen in Fig. 8.39(a). This, combined with a higher gases flow velocity than in Simulation 1 forces the fresh gases to travel a longer distance before burning: the flame obtained in Simulation 2 is longer than that of Simulation 1.

Figure 8.40 shows a comparison of time averaged heat release fields between simulations 1 and 2: the presence of hot burnt gases in both the CRZ and the CORZ in Simulation 1 leads to a compact flame. On the other hand, a flame  $\sim 50\%$  longer is found in Simulation 2, as it is only stabilized by the CRZ. The latter flame is also observed to be much more defined in space, as a result of the stable behaviour.



**Figure 8.39:** Sequence of instantaneous temperature fields and reaction rate isocontours showing the transition to stability in Simulation 2.

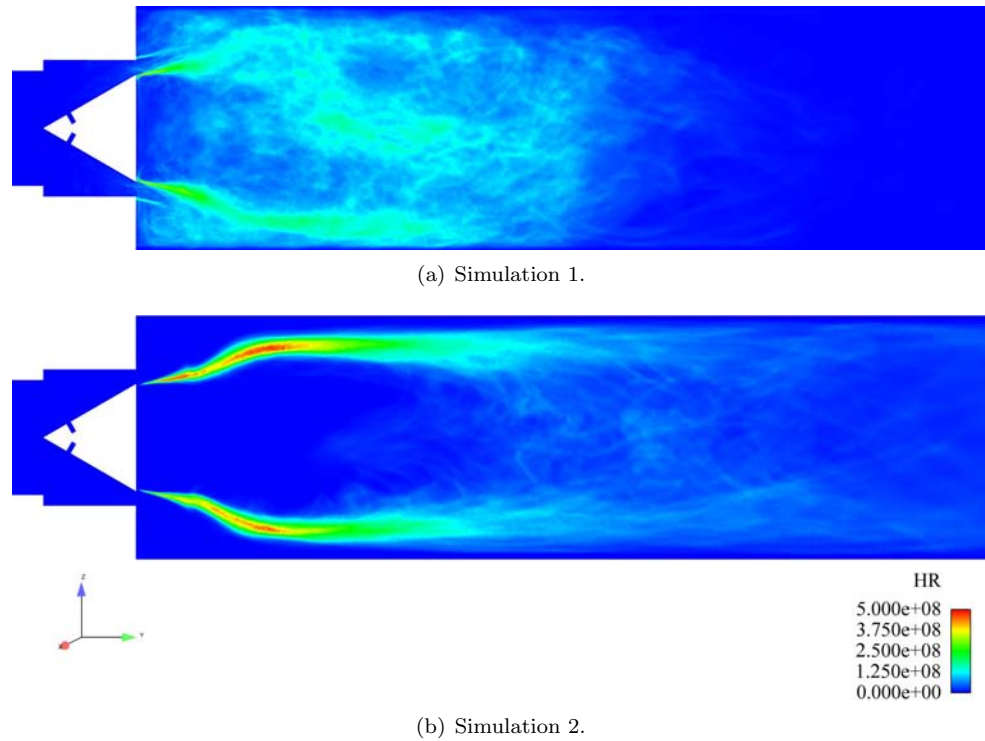
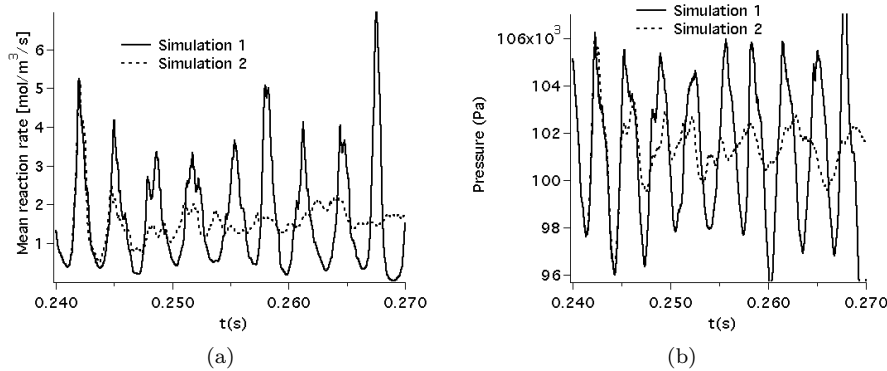


**Figure 8.40:** Comparison of mean heat release rate fields between simulations 1 and 2 showing the difference in flame length and flame stabilization by the CORZ.

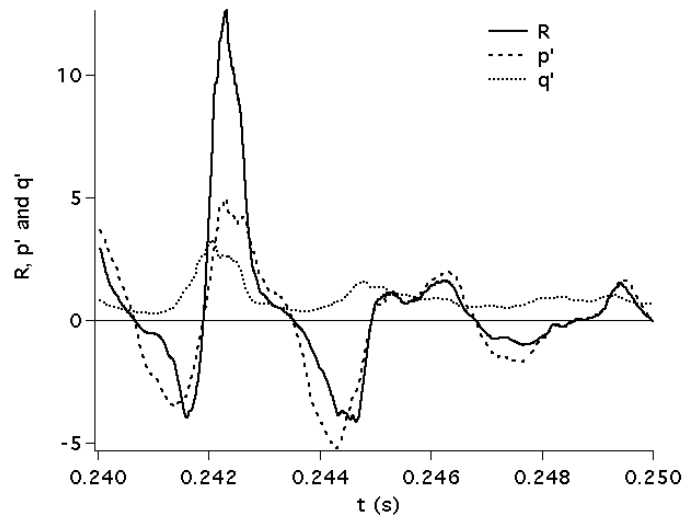
Figure 8.41 shows a comparison of mean reaction rate temporal evolution and pressure signal at the location of probe 4 between simulations 1 and 2. When conditions are changed from OP1 (Simulation 1) to those of OP2 (Simulation 2), the mean reaction rate within the combustor stops oscillating and gets stabilized, showing only small amplitude around its mean value, which are ascribed to turbulent fluctuations. The effect on the pressure signal is clear, the large amplitude periodic oscillations cease to exist and only uncorrelated pressure fluctuations are observed. This behaviour is explained by the fact that, as a result of the change in flame stabilization process, the longer flame obtained leads to a spatially distributed heat release rate which is no longer in phase with the pressure oscillations. Even when heat release rate temporal fluctuations might be locally in phase with pressure oscillations, injecting energy into the acoustic field, heat release rate and pressure fluctuations are out of phase elsewhere, hence an inverse energy transfer out of the acoustic field is taking place. Globally, there is not a net energy transfer from the flame to the acoustic mode of the LCO, and the thermo-acoustic instability dies out.

Figure 8.42 shows the temporal evolution of the Rayleigh parameter, relative

pressure fluctuations at the location of probe 4 and normalized mean heat release rate corresponding to Simulation 2. Acoustic pressure oscillations cease to be in phase with the heat release rate leading to negative values of the Rayleigh parameter. Negative values of  $R$  indicate that, globally, energy is being pumped out of the acoustic mode thus leading to the suppression of the thermo-acoustic instability. The role of the flame stabilization by the hot gases in the CORZ on the transition to combustion stability was previously studied by Huang [65], where similar conclusions were drawn.



**Figure 8.41:** Comparison of (a) Mean reaction rate temporal evolution and (b) Pressure signal at probe 4, between simulations 1 (solid lines) and 2 (dashed lines).



**Figure 8.42:** Rayleigh parameter, relative pressure fluctuation time signal and normalized mean heat release rate of Simulation 2.

### 8.10 Simulation 3: influence of burner geometry

Before the definitive version (V.3) of the LIMOUSINE burner, another version was built and operated, referred to as V.2. Fig. 8.43 shows burner geometry details around the wedge zone for the V.3 and V.2 versions. It is seen that side blocks were added at both sides of the wedge in the version V.3 with respect to V.2. When the side blocks are removed, the contraction to the flow passage to the downstream duct is eliminated. Also, the right angle corners between the side blocks and the liner walls disappear.

V.2 was observed to show a stable behaviour for all the operating range studied. Since the purpose of the LIMOUSINE project was to study thermo-acoustic oscillations, version V.3 was built and tested, showing LCO as desired. However, studying version V.2 was also a useful exercise, described here with LES.

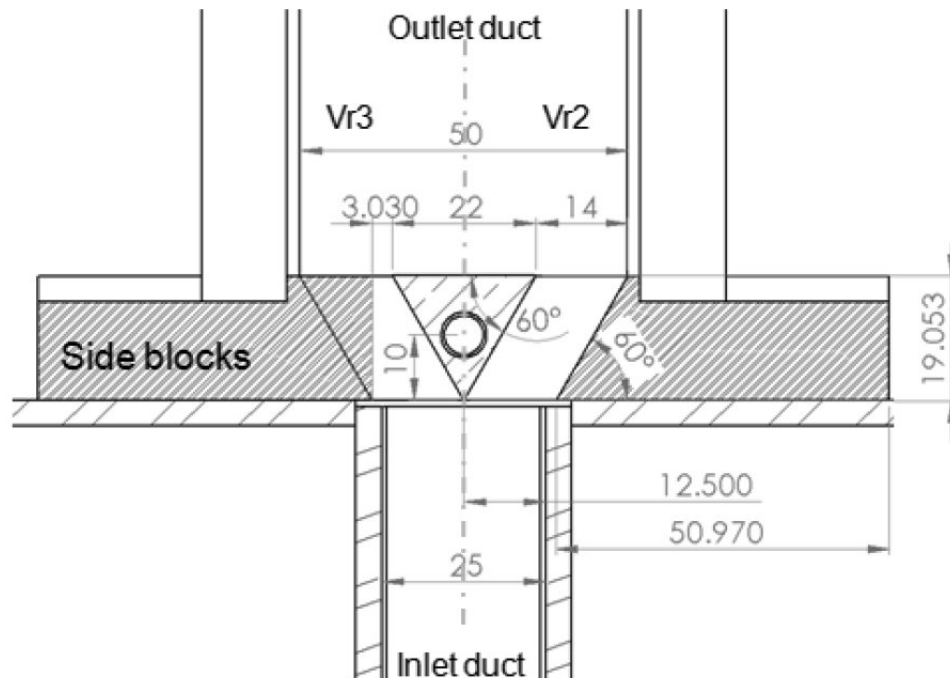
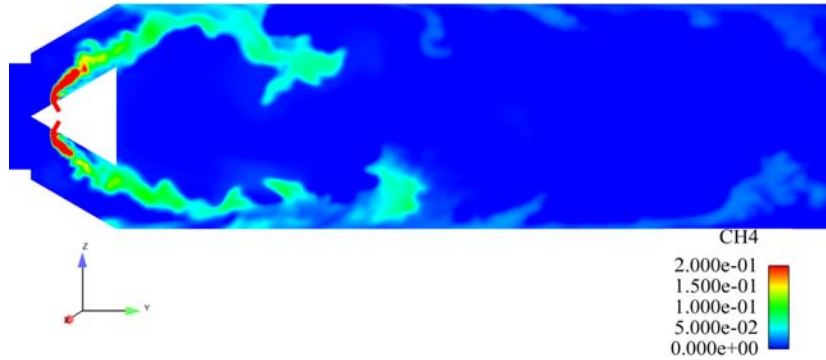


**Figure 8.43:** Drawing of the burner geometry around the wedge showing the differences between versions V.3 (left half) and V.2 (right half). Dimensions are in *mm*. Figure provided by the University of Twente..

In order to study the effect of geometrical changes on the stability of the LIMOUSINE burner, a simulation of version V.2 was performed (Simulation

3). This allows to determine the flow features in this configuration, and the possible reasons of its behaviour. The operating point and the parameters of the simulation are those of Simulation 1.

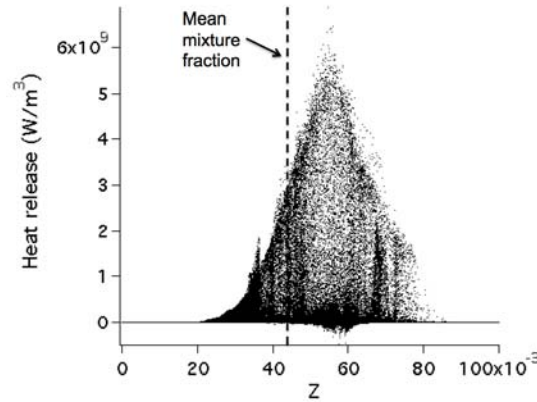
Figure 8.44 shows an instantaneous fuel mass fraction field of Simulation 3. Fuel jets start mixing as they meet the air stream in cross flow but they do not have enough time to mix before entering the downstream duct. Indeed, two separate streams, corresponding the fuel and air can be clearly differentiated as the chamber entrance. As the side blocks were removed, the flow does not experience any acceleration as they enter the chamber, and a poor fuel/air mixing is achieved. Also, no CORZ at both sides of the wedge are observed, since the removal of the side blocks leads to a straight duct configuration with no place for the flow to recirculate, except for the CRZ.



**Figure 8.44:** Instantaneous fuel mass fraction field of Simulation 3.

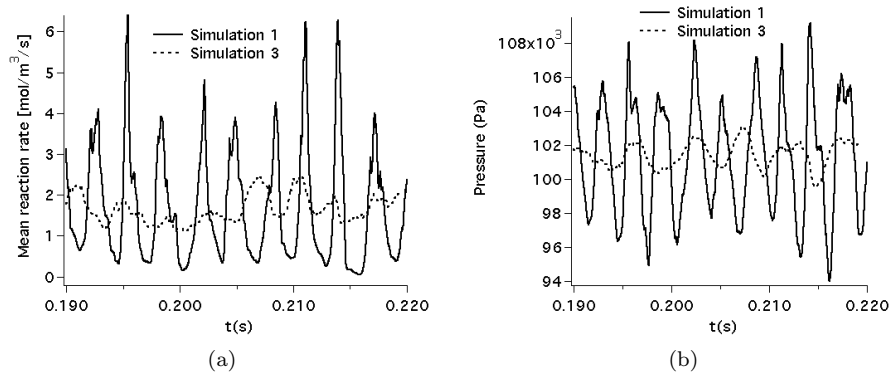
Figure 8.45 shows a scatterplot of heat release rate versus mixture fraction of an instantaneous solution of Simulation 3. The shape of the scatterplot indicates that combustion is taking place mainly in a diffusion mode, as the flame structure reproduces the theoretical Burke-Schumann structure of diffusion flames [24]. The flame structure obtained in the burner version V.2 is therefore different from the one obtained in the simulations of version V.3, as seen previously in Fig. 8.13, where a partially-premixed mode of combustion was observed.

Figure 8.47 shows a sequence of instantaneous temperature fields and reaction rate isocontours of Simulation 3. It is seen that the flame is only stabilized by the hot gases in the CRZ, since the CORZ does not even exist on this configuration. The poor fuel/air mixing leads to a diffusion flame which spans a distance of  $\sim 10$  cm along the downstream duct, which is  $\sim 50\%$  to  $100\%$  longer than the flame of Simulation 1, as seen in Fig. 8.17. Also, due to the absence of flow acceleration at the chamber entrance, low turbulence levels are generated at the shear layers between the fresh gases and the gases in the CRZ, leading to a flame front which is less wrinkled than in Simulation 1.



**Figure 8.45:** Scatterplot of heat release versus mixture fraction of an instantaneous solution of Simulation 3.

Figure 8.46 shows a comparison of mean reaction rate temporal evolution and pressure signals between simulations 1 and 3: the heat release rate experiences some perturbations whose amplitude is, however, much lower than the ones seen in Simulation 1. Likewise, pressure fluctuations are observed in Simulation 3, which are small compared to the ones of Simulation 1. Even though pressure and heat release oscillations are present in Simulation 3, they are not LCO, since their amplitude is low and they do not follow a clear pattern. The reasons why LCO are not reached in this case are similar to the ones explained for Simulation 2: the long flame obtained (here due to a poor fuel/air mixing) decouples the heat release rate oscillations from the pressure oscillations because of the subsequent spatially distributed heat release.



**Figure 8.46:** Comparison of (a) Mean reaction rate temporal evolution and (b) Pressure signal at probe 4, between simulations 1 (solid lines) and 3 (dashed lines).

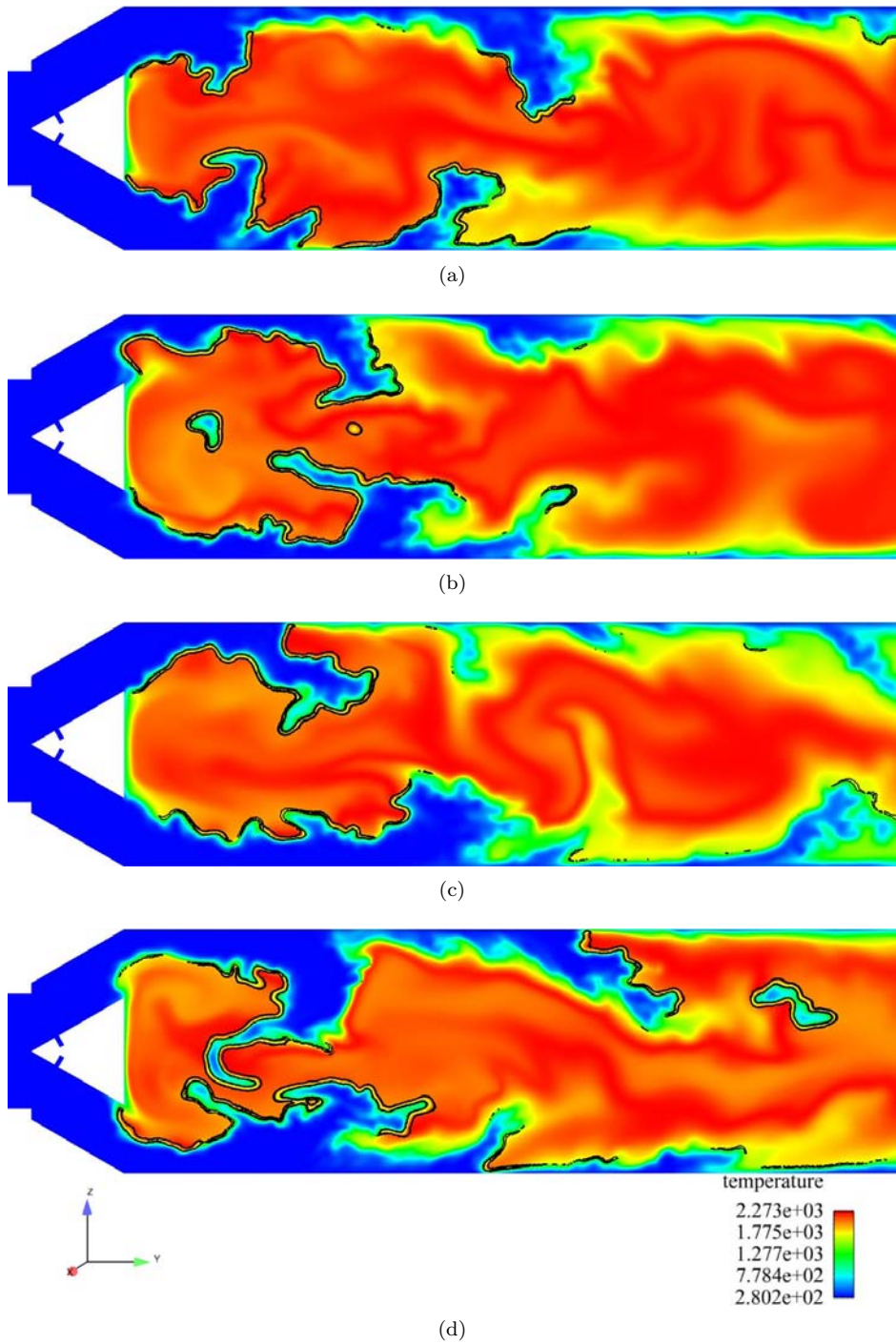


**Figure 8.47:** Sequence of instantaneous temperature fields and reaction rate isocontours showing the flame behaviour in Simulation 3.

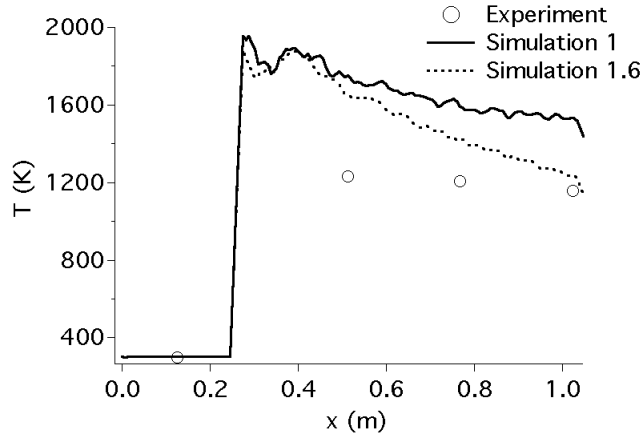
## 8.11 Comparison with experimental results

Several experimental measurements are available for the validation of the LES. Comparisons between the simulations and the experiments are made in this section.

### 8.11.1 Version V.3 at OP1

Figure 8.48 shows temperature profiles along the central line of the burner in Simulations 1 and 1.6, as well as temperature values measured with the thermocouples of Fig. 7.4. Simulation 1 seems to overpredict the temperature of the burnt gases by  $\sim 400$  K with respect to the experimental measurements. This difference is lower for Simulation 1.6 (radiative heat losses included), who predicts the correct gases temperature only at the burner outlet.

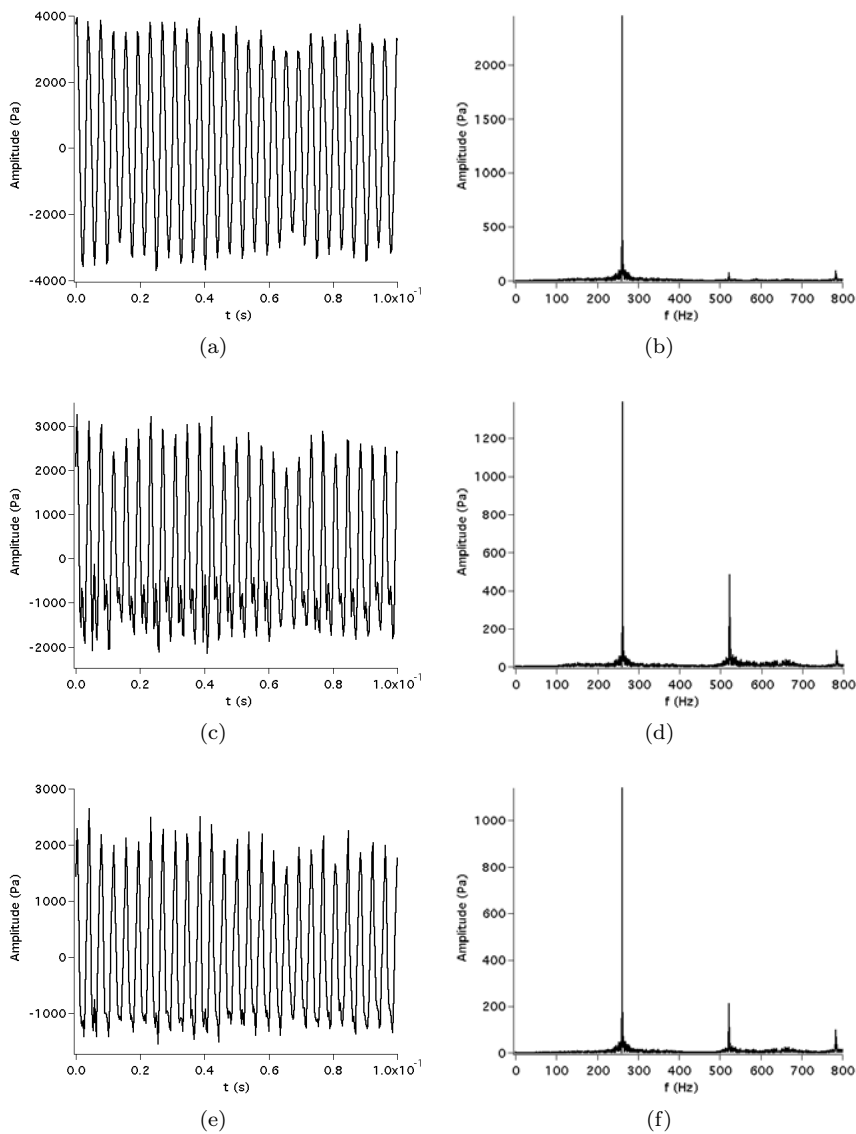
It is worth noting that the thermocouples used (thick type) are subject to radiative losses, so that the temperature value they provide underestimates the real temperature within the burner. The error is estimated to be 100 K so that the difference between simulation and experiment might not be that high. However, even taking into account the temperature correction of the measurements, temperature is still overpredicted by the LES.



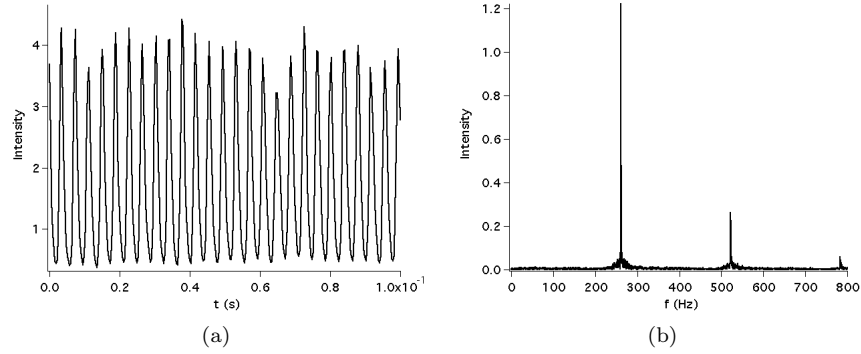
**Figure 8.48:** Comparison of experimental temperature measurements and computed temperature profiles along the central axis of the burner without (Simulation 1) and with (Simulation 1.6) radiative losses.

Figure 8.49 shows pressure signals measured with the pressure probes 4, 5 and 6 and their Fourier Transforms. A clear oscillatory behaviour at a dominant frequency of **261 Hz** is observed. The amplitude of the pressure oscillations is  $\approx 4000$  Pa, which indicates the presence of LCO of a thermo-acoustic instability. Also, a secondary pressure peak is found at a frequency of **522 Hz**, indicating the appearance of another unstable mode. Finally, a heat release rate time

signal (and Fourier Transform) obtained with a OH radical photomultiplier are shown in Fig. 8.50, which confirms the existence of LCO at a frequency of 261 Hz.



**Figure 8.49:** (a), (c), (e) Time signals of the pressure fluctuations around their mean value recorded in the experiment of V.3 burner at OP1. Signals correspond to pressure probe locations 4, 5 and 6 respectively. (b), (d), (f) Fourier Transforms of the pressure signals from probes 4, 5 and 6 respectively.



**Figure 8.50:** Heat release rate signal of the V.3 burner at OP1 measured with a OH radical photomultiplier. (a) Time signal. (b) Fourier Transform of the time signal.

The LES of the V.3 burner at OP1 also captured LCO. However, the predicted frequency of the dominant unstable mode was higher than the one observed in the experiment (303 Hz in Simulation 1.6). This is partly ascribed to the fact that heat losses seem to be underestimated in the simulations, leading to an overprediction of the burnt gases temperature along the combustor, as seen in Fig. 8.48. Another source of error might be the resolution of the pressure spectrum from the LES. Indeed, a poor resolution is observed compared to the experiment. The spectral resolution is proportional to the number of cycles computed and the only way to improve this is to compute longer times. However, the cost of LES in terms of computational time and money were already high enough, so that they were stopped after an acceptable resolution of the spectra was obtained. There is no way the LES can compete with the experiment when it comes to resolution of the spectra, since the experiment captures seconds (or minutes) of pressure signal in real time, whereas this would be years of computing. Nevertheless the spectrum resolution is still an additional source of error, so that the frequency of the LCO captured by the LES might be closer to the experiment than expected. Finally, the amplitude of the LCO is well predicted by the simulations.

The flame shape in the unstable case seems to be well described by the simulations. Figure 8.51 shows a sequence of images of the flame obtained experimentally using CH radical chemiluminescence. The frequency of the CH camera is 500 Hz which, taking into account that the flame is observed in exactly 1 snapshot out of two, confirms again that LCO occur at a frequency close to 250 Hz in the experiment. The flame observed in the experiment has a ball-like shape, rather than well defined flame wings at each side of the flame holder. This is in accordance with the simulations, where it was seen that large mushroom-like vortices issuing from the 3mm gaps, as well as small scale turbulence, fold the flame fronts leading to a flame shape similar to the one observed experimentally.

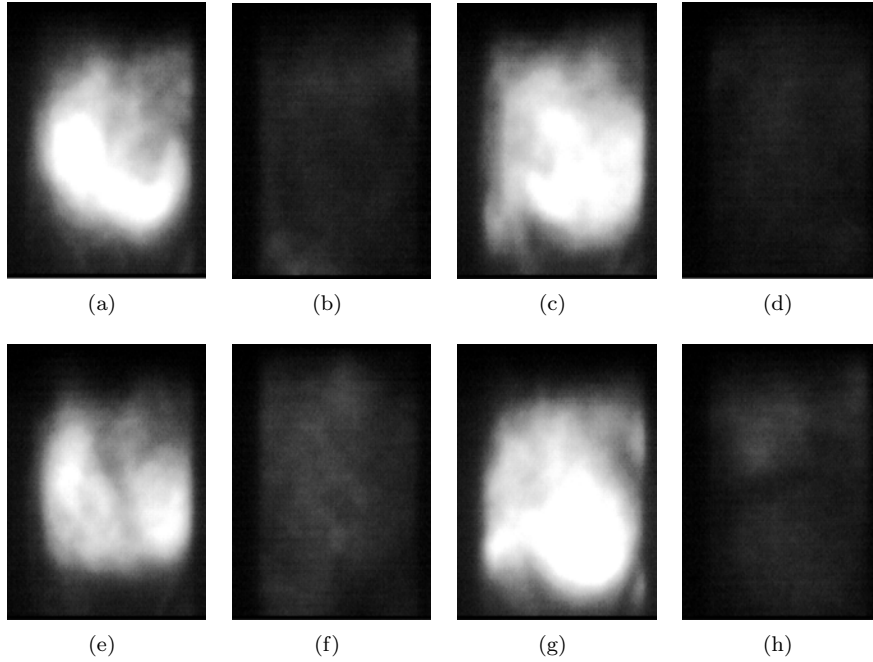


**Figure 8.51:** Sequence of CH radical chemiluminescence images recorded at a frequency of 500 Hz on the V.3 burner at OP1. Unstable combustion is observed.

Figure 8.50 shows a comparison of the modes structures between the acoustic code, the LES and the experiment. The experimental modes structures were constructed using the Fourier Transform of the pressure signals at the six pressure probes along the combustor. Fig. 8.52(a) shows the dominant unstable mode predicted in the LES and the one measured experimentally. The second acoustic eigenmode given by AVSP is included in the figure. This mode corresponds to a three-quarters wave mode of the whole burner, where a discontinuity is observed in the wedge zone due to the sudden change in cross section area. The shape of the unstable mode is well predicted by the LES, with respect to the experiment. However, AVSP underestimates the amplitude of the pressure mode in the downstream duct. This may be due to the fact that no active flame model was used in computations of the acoustic eigenmodes. Fig. 8.52(b) shows the structure of the secondary unstable mode predicted by the LES and the one measured experimentally, as well as the third acoustic eigenmode given by AVSP. This mode corresponds to the five-quarters wave mode of the chamber and there is a good agreement between the LES, the experiment and AVSP.

A question arises at this point regarding the instability modes observed both in the LES and in the experiment: why is it that the unstable modes are the three-quarters and five-quarters wave modes, and not the quarter wave mode of

the chamber? Indeed, the quarter wave mode is *a priori* the most likely mode to become unstable, since it is the dominant one. Let us notice that, in the present configuration, the so-called three-quarter wave mode of the full burner can also be seen as the quarter wave mode of the downstream duct alone. The small dimension of the gaps between the wedge and the side walls defines a high blockage ratio between the upstream and downstream ducts, so that the interface section acts practically as a solid wall, therefore imposing a pressure antinode, as observed in Fig. 8.52. Therefore the dominant mode of the LCO is in reality a quarter wave mode.

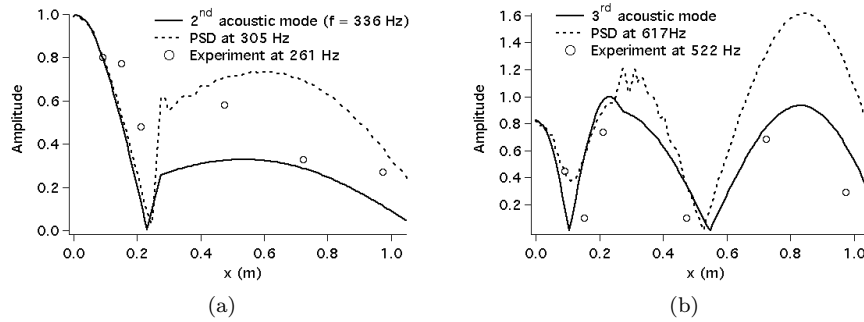


**Figure 8.52:** Comparison of modes structures: a) Second acoustic mode given by AVSP and dominant unstable modes from the LES and the experiment, b) Third acoustic mode given by AVSP and secondary unstable modes from the LES and the experiment.

### 8.11.2 Version V.3 at OP2

The V.3 burner, although unstable at OP1, showed a stable behaviour at when working under conditions of OP2 (see Fig. 7.5). Indeed, when the air factor was increased from the one of OP1 to that of OP2, the LCO disappeared and a stable flame was observed. Fig. 8.53 shows a sequence of images recorded with CH radical chemiluminescence. A stable flame is observed in the sense that the heat release is located in the same region over time, except for some small flapping of the flame wings due to turbulence. Also, only low-amplitude broadband noise was recorded with the pressure probes during operation indicating the absence of LCO.

Similar characteristics were observed in Simulation 2: a stable flame regime was predicted. Only low-amplitude pressure fluctuations at no particular frequency were recorded in the simulation. Also, a well-defined in space flame was obtained (see Fig. 8.40(b)), in accordance with the experimental observations.

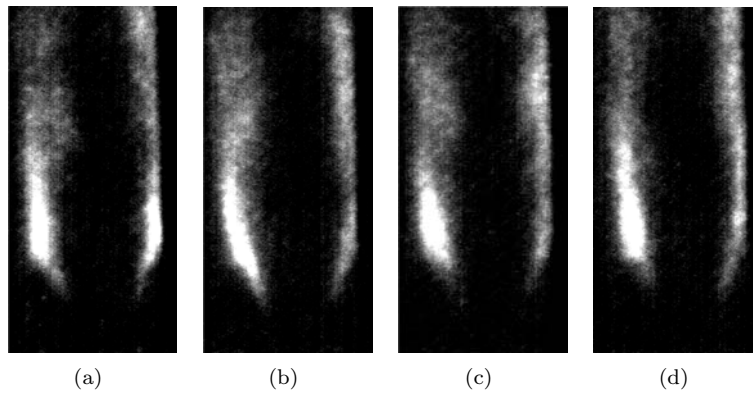


**Figure 8.53:** Sequence of CH radical chemiluminescence images recorded at a frequency of 500 Hz on the V.3 burner at OP2. Stable combustion is observed.

### 8.11.3 Version V.2 at OP1

Figure 8.54 shows a picture of the flame observed in the V.2 burner at OP1. A stable flame is obtained, with two wings at each side of the wedge which are well located in space. Also, no pressure or heat release oscillations were observed in this burner version. The same results were predicted by the LES in Simulation 3: a stable flame was obtained and only low-amplitude broadband noise was recorded at the location of the pressure probes.

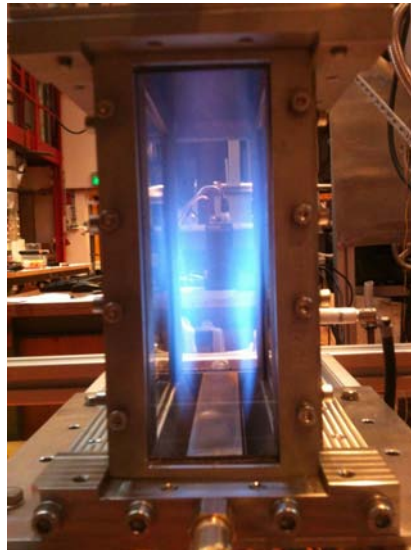


**Figure 8.54:** Picture showing the stable flame on the V.2 burner at OP1.



## Chapter 9

# Conclusions and perspectives II

### 9.1 Conclusions on LES of thermo-acoustic instabilities

Large-Eddy Simulation and acoustic analysis tools were used to study the behaviour of a partially premixed, methane/air burner operating at atmospheric pressure known as the LIMOUSINE test rig. In particular, the flame stability and the characteristics of the LCO are studied and the results are compared to experimental measurements. Several conclusions are drawn:

- The LES was able to capture the appearance and development of thermo-acoustic instabilities in the configuration studied. The amplitude of the LCO and the shape of the unstable modes were well predicted. However, the frequency of the LCO was somewhat overpredicted by the LES. This is ascribed to the fact that the burnt gases temperature along the combustor were overpredicted, which is due to an underestimation of the heat losses through the walls.
- The LES shows that the stability of the flame can be changed with the mean flow velocity. An increase in air mass flow rate implied a increase in flame length which led to its stabilization due to a decoupling of the flame and the acoustic field. The LES allowed to identify the role of the corner recirculation zones (CORZ) on the flame stability. It was shown that the presence of CORZ leads a short flame which is prone to thermo-acoustic instabilities.
- A stabilization of the flame was observed when the burner geometry was changed from the one of version V.3 to that of version V.2. A poor mixing

and a change in the flame stabilization characteristics led to the suppression of the thermo-acoustic instability. This stable flame regime was also captured by the LES.

- The LES results showed a small dependence on the fuel lines inlet impedances for the configuration studied. The region upstream of the wedge acts as a reservoir that absorbs transients in the fuel/air mixing process due to fuel inlet mass flow rate fluctuations. Likewise, air lines inlet impedance showed to have little or no effect on the LES results.
- Heat losses showed to play no major role on the stability of the flame for the configuration studied. However, they control the temperature of the burnt gases along the combustor, which has an influence on the frequency of the LCO.

## 9.2 Perspectives

The LES results showed a good agreement with the experiments. However, there are certain aspects that require some improvements. They constitute additional topics left for future studies:

- Accurate boundary conditions are needed in order to describe the correct heat losses to the walls. It was shown that they control the temperature of the gases along the downstream duct, with the associated impact on the acoustics of the chamber. A correct prediction of the wall temperature and the heat losses to the walls demands the use of conjugate heat transfer methods [46], whereby the heat equation is solved within the solid parts.
- More complicated radiative models are costly but offer greater accuracy. Here, the length of the combustor seems to demand models where radiation absorption within the gas phase is accounted for. The adoption here of the optically thin limit approximation was made for the sake of simplicity but coupled simulations of the LES with a radiative code seem to be a good option for the future [118].
- The utilization of a reduced computational domain throughout the present work implied that the interaction between adjacent fuel holes, as well as 3D turbulence were neglected. A step further would imply computations of the full burner to account for such effects. Also, the use of a full 3D domain would present two extra solid surfaces that might have an impact on the heat losses.
- Computations of fluid-structure interaction (FSI) seem to be interesting for the present configuration. The large pressure oscillations arising during the LCO of the thermo-acoustic instability might affect the structure in

such a way that one or more natural vibration modes of the burner liner could be excited, and thus, affect the acoustics of the chamber. As a matter of fact, previous experimental studies on the LIMOUSINE test rig showed that wall vibrations had a large impact on the stability of the flame [28].



# References

- [1] F.J. Diez C. Aalburg, P.B. Sunderland, D.L. Urban, W.G. Yuan, and G.M. Faeth. Soot properties of laminar jet diffusion flames in microgravity. *Combust. Flame* , 156:1514–1524, 2009.
- [2] A.D. Abid, N. Heinz, E.D. Tolmachoff, D.J. Phares, C.S. Campbell, and H. Wang. On evolution of particle size distribution functions of incipient soot in premixed ethylene-oxygen-argon flames. *Combust. Flame* , 154:775–788, 2008.
- [3] J. Amaya, O. Cabrit, D. Poitou, B. Cuenot, and M. El Hafi. Unsteady coupling of Navier-Stokes and radiative heat transfer solvers applied to an anisothermal multicomponent turbulent channel flow. *J. Quant. Spect. and Radiative Transfer* , 111(2):295–301, January 2010.
- [4] J. Amaya, E. Collado, B. Cuenot, and T. Poinso. Coupling LES, radiation and structure in gas turbine simulations. In NASA Ames/Stanford Univ. Center for Turbulence Research, editor, *Proc. of the Summer Program* , volume in press, 2010.
- [5] E. Anderson, Z. Bai, C. Bischof, S. Blackford, J. Demmel, J. Dongarra, J. Du Croz, A. Greenbaum, S. Hammarling, A. McKenney, and D. Sorensen. *LAPACK Users' Guide*. Society for Industrial and Applied Mathematics, Philadelphia, PA, third edition, 1999.
- [6] J. Appel, H. Bockhorn, and M. Frenklach. Kinetic modeling of soot formation with detailed chemistry and physics: laminar premixed flames of C<sub>2</sub> hydrocarbons. *Combust. Flame* , 121:122–136, April 2000.
- [7] S. Apte, K. Mahesh, and P. Moin. Large-eddy simulation of evaporating spray in a coaxial combustor. *Proc. Combust. Inst.* , 32(2):2247–2256, 2009.
- [8] ASCAC. The opportunities and challenges of Exascale computing. Summary report of the advanced Advisory committee (ASCAC) subcommittee. Technical report, Department of Energy, 2010.

- [9] M. Barrère and F. A. Williams. Comparison of combustion instabilities found in various types of combustion chambers. *Proc. Combust. Inst.* , 12:169–181, 1968.
- [10] T. Beji, J. P. Zhang, W. Yao, and M. Delichatsios. Validation of a novel soot model in laminar diffusion flames: fuel, flow rate and thermophoretic effects. In The Combustion Institute, editor, *Sixth Mediterranean Combustion Symposium*, 2009.
- [11] T. Beji, J.P. Zhang, W. Yao, and M. Delichatsios. A novel soot model for fires: validation in a laminar non-premixed flame. *Combust. Flame* , 158(2):281–290, 2010.
- [12] M. Bhaltasar and M. Kraft. A stochastic approach to calculate the particle size distribution function of soot particles in laminar premixed flames. *Combust. Flame* , 133(289-298), 2003.
- [13] A. Bhargava and P.R. Westmoreland. Measured flame structure and kinetics in a fuel-rich ethylene flame. *Combust. Flame* , 113(3):333–347, 1998.
- [14] R. B. Bird, W. E. Stewart, and E. N. Lighfoot. *Transport phenomena*. John Wiley, New York, 1960.
- [15] T. Blacha, M. Di Domenico, P. Gerlinger, and M. Aigner. Soot predictions in premixed and non-premixed laminar flames using a sectional approach for PAHs and soot. *Combust. Flame* , 2011.
- [16] T. Blacha, M. Di Domenico, M. Köhler, P. Gerlinger, and M. Aigner. Soot modeling in a turbulent unconfined C<sub>2</sub>H<sub>4</sub>/air jet flame. *Proceedings 49th AIAA Aerospace Sciences Meeting Including the New Horizons Forum and Aerospace Exposition, Orlando (USA)*, 2011.
- [17] G. Blanquart, P. Pepiot-Desjardins, and H. Pitsch. Chemical mechanism for high temperature combustion of engine relevant fuels with emphasis on soot precursors. *Combust. Flame* , 156:588–607, 2008.
- [18] M. Bönig, Chr. Feldermann, H. Jander, B. Lüers, G. Rudolph, and H. Gg. Wagner. Soot formation in premixed C<sub>2</sub>H<sub>4</sub> flat flames at elevated pressure. In The Combustion Institute, editor, *Twenty-Third Symposium (International) on Combustion*, pages 1581–1587, 1990.
- [19] J. Boussinesq. Essai sur la théorie des eaux courantes. *26ème édn. Acad. Sci. Paris*, 1877.
- [20] N. W. Bressloff, J. B. Moss, and P. A. Rubini. CFD prediction of coupled radiation heat transfer and soot production in turbulent flames. In The Combustion Institute, editor, *Twenty-Sixth Symposium (International) on Combustion*, 1996.

- [21] H. T. Brocklehurst, J. B. Moss, C. D. Hurley, and C. H. Priddin. Soot and Radiation Modeling in Gas Turbine Combustion Chambers. In *RTO AVT Symposium on "Gas Turbine Engine Combustion, Emissions and Alternative Fuels"*, 1998.
- [22] S. J. Brookes and J. B. Moss. Predictions of soot and thermal radiation properties in confined turbulent jet diffusion flames. *Combust. Flame* , 116:486–503, 1999.
- [23] N J. Brown, K. L. Revzan, and M. Frenklach. Detailed kinetic modeling of soot formation in ethylene/air mixtures reacting in a perfectly stirred reactor. *Twentieth Symposium (International) on Combustion*, 27:1573–1580, 1998.
- [24] S. P. Burke and T. E. W. Schumann. Diffusion flames. *Industrial and Engineering Chemistry*, 20(10):998–1005, 1928.
- [25] H. F. Calcote and D. M. Manos. Effect of molecular structure on incipient soot formation. *Combust. Flame* , 49:289–304, 1983.
- [26] S. Candel, C. Huynh., and T. Poinso. Some modeling methods of combustion instabilities. In *Unsteady combustion*, pages 83–112. Nato ASI Series, Kluwer Academic Publishers, Dordrecht, 1996.
- [27] D. Carbonell, A. Oliva, and C.D. Pérez-Segarra. Implementation of two-equation soot flamelet models for laminar diffusion flames. *Combust. Flame* , 156:621–632, 2009.
- [28] J.C. Román Casado, R. Alemela, and J.B.W. Kok. Combustion dynamics coupled to structural vibration. In *The 17th International Congress on Sound and Vibration*, Cairo, 2010.
- [29] CERFACS. *AVBP Handbook* - [http://cerfacs.fr/~avbp/AVBP\\_V6.X/HANDBOOK/handbook.php](http://cerfacs.fr/~avbp/AVBP_V6.X/HANDBOOK/handbook.php). CERFACS, 2009.
- [30] C. Changan, P. Liaw, M. Ye, and J. Yu. Recent developments in the thermomechanical fatigue life prediction of superalloys. *Journal of metals*, 51(4), 1999.
- [31] F. Charlette, D. Veynante, and C. Meneveau. A power-law wrinkling model for LES of premixed turbulent combustion: Part I - non-dynamic formulation and initial tests. *Combust. Flame* , 131:159–180, 2002.
- [32] O. Colin, F. Ducros, D. Veynante, and T. Poinso. A thickened flame model for large eddy simulations of turbulent premixed combustion. *Phys. Fluids* , 12(7):1843–1863, 2000.
- [33] O. Colin and M. Rudgyard. Taylor-Galerkin Schemes in AVBP. Technical Report TR/CFD/98/56, CERFACS, 1998.

- [34] R. Courant, K. O. Friedrichs, and H. Lewy. On the partial differential equations of mathematical physics. *Math Ann.*, 100:32–74, 1928.
- [35] C.P.Fenimore and G.W.Jones. Oxidation of soot by hydroxyl radicals. *J. Phys. Chem*, 71:593–597, 1967.
- [36] L. Crocco. Aspects of combustion instability in liquid propellant rocket motors. Part I. *J. American Rocket Society* , 21:163–178, 1951.
- [37] L. Crocco and S. I. Cheng. *Theory of combustion instability in liquid propellant rocket motors*, volume Agardograph No 8. Butterworths Science, 1956.
- [38] F. E. C. Culick. Combustion instabilities in liquid-fueled propulsion systems- An overview. In *AGARD 72B PEP meeting*, 1987.
- [39] A. D’Anna, M. Sirignano, and J. Kent. A model of particle nucleation in premixed ethylene flames. *Combust. Flame* , 157(1):2106–2115, November 2010.
- [40] S. G. Davis, C. K. Law, and H. Wang. Propene pyrolysis and oxidation kinetics in a flow reactor and laminar flames. *Combust. Flame* , 119:375–399, 1999.
- [41] D.G.Goodwin. *Cantera C++ Users Guide*. <http://sourceforge.net/projects/cantera>, 2002.
- [42] M. Di Domenico, P. Gerlinger, and M. Aigner. Development and validation of a new soot formation model for gas turbine combustor simulations. *Combust. Flame* , 157:246–258, 2009.
- [43] L. H. Dorey, L. Tessé, N. Bertier, and F. Dupoirieux. A strategy for modeling soot formation and radiative transfer in turbulent flames. In *Proceedings of the International Heat Transfer Conference, Washington DC, USA*, 2010.
- [44] A. P. Dowling. The calculation of thermoacoustic oscillations. *J. Sound Vib.* , 180(4):557–581, 1995.
- [45] Ann P. Dowling. The challenges of lean premixed combustion. *Proc. International Gas Turbine Congress*, 2003.
- [46] F. Duchaine, S. Mendez, F. Nicoud, A. Corpron, V. Moureau, and T. Poinso. Conjugate heat transfer with Large Eddy Simulation application to gas turbine components. *C. R. Acad. Sci. Mécanique*, 337(6-7):550–561, 2009.
- [47] D. Durox, T. Schuller, N. Noiray, A.L. Birbaud, and S. Candel. Rayleigh criterion and acoustic energy balance in unconfined self-sustained oscillating flames. *Combust. Flame* , 155(3):416–429, 2008.

- [48] H. El-Asrag. *Large Eddy Simulation subgrid model for soot prediction*. PhD thesis, Georgia Institute of Technology, May 2007.
- [49] H. El-Asrag, T. Lu, C. K. Law, and S. Menon. Simulation of soot formation in turbulent premixed flames. *Combust. Flame*, 150:108–126, 2007.
- [50] H. El-Asrag and S. Menon. Large eddy simulation of soot formation in a turbulent non-premixed jet flame. *Combust. Flame*, 156(2):385–395, 2009.
- [51] A. Ern and V. Giovangigli. *Multicomponent Transport Algorithms*. Lecture Notes in Physics. Springer Verlag, Heidelberg, 1994.
- [52] O. A. Ezekoye and Z. Zhang. Soot oxidation and agglomeration modeling in a microgravity diffusion flame. *Combust. Flame*, 110:127–139, 1997.
- [53] L. Selle F. Duchaine and T. Poinso. *Combust. Flame*, 2011.
- [54] M. Frenklach. Method of moments with interpolative closure. *Chem. Eng. Sci.*, 57(12):2229–2239, 2002.
- [55] M. Frenklach. Reaction mechanism of soot formation in flames. *Phys. Chem. Chem. Phys.*, (4):2028–2037, 2002.
- [56] M. Frenklach and H. Wang. *Twenty-Third Symposium (International) on Combustion*, page 1559, 1990.
- [57] M. Frenklach, H. Wang, M. Goldenberg, G. P. Smith, D. M. Golden, C. T. Bowman, R. K. Hanson, W. C. Gardiner, and V. Lissianki. GRI-Mech: an optimized detailed chemical reaction mechanism for methane combustion. Technical Report GRI-Report GRI-95/0058, Gas Research Institute, 1995.
- [58] N. Georgiadis, D. P. Rizzetta, and C. Fureby. Large-Eddy Simulation: Current capabilities, recommended practices and future research. In *47th Aerospace Sciences Meeting*. AIAA, 2009.
- [59] J. P. Gore, J. Lim, T. Takeno, and X. L. Zhu. A study of the effects of thermal radiation on the structure of methane/air counter-flow diffusion flames using detailed chemical kinetics. In *Book of Abstracts of the 5th ASME/JSME Joint Thermal Engineering Conference*, page 50, 1999.
- [60] V. Goutière, A. Charette, and L. Kiss. Comparative performance of non-gray gas modeling techniques. *Numerical Heat Transfer Part B: Fundamentals*, 41:361–381, 2002.
- [61] H. Hassan. Scaling of combustion generated noise. *J. Fluid Mech.*, 49:445–453, 1974.
- [62] B. S. Haynes and G. Gg. Wagner. Soot formation. *Prog. Energy Comb. Sci.*, 7:229–237, 1981.

- [63] J. O. Hirschfelder, C. F. Curtiss, and R. B. Bird. *Molecular theory of gases and liquids*. John Wiley & Sons, New York, 1969.
- [64] S. Hong, M. S. Wooldridge, H. G. Im, D. N. Assanis, and H. Pitsch. Development and application of a comprehensive soot model for 3D CFD reacting flow studies in a Diesel engine. *Combust. Flame*, 143:11–26, 2005.
- [65] Y. Huang and V. Yang. Bifurcation of flame Structure in a Lean Premixed Swirl-Stabilized Combustor: Transition from Stable to Unstable Flame. *Combust. Flame*, 136:383–389, 2004.
- [66] I. R. Hurle, R. B. Price, T. M. Sudgen, and A. Thomas. Sound emission from open turbulent premixed flames. *Proc. R. Soc. Lond.*, 303:409–427, 1968.
- [67] J. Y. Hwang and S. H. Chung. Growth of soot particles in counterflow diffusion flames of ethylene. *Combust. Flame*, 125:752–762, 2001.
- [68] F. P. Incropera, D. P. Dewitt, T. L. Bergman, and A. Lavine. *Fundamentals of heat and mass transfer*. John Wiley & Sons, 6th edition, 2007.
- [69] F. Jaegle. *LES of two-phase flow in aero-engines*. PhD thesis, Université de Toulouse - Ecole doctorale MEGeP, CERFACS - CFD Team, Toulouse, December 2009.
- [70] H. Jung, B. Guo, C. Anastasio, and I. M. Kennedy. Quantitative measurements of the generation of hydroxyl radicals by soot particles in a surrogate lung fluid. *Atmospheric Environment*, 40(6):1043–1052, 2006.
- [71] B. A. Kader. Temperature and Concentration Profiles in Fully Turbulent Boundary Layers. *Int. J. Heat and Mass Transfer*, 24(9):1541–1544, 1981.
- [72] C. R. Kaplan, C. R. Shaddix, and K. C. Smyth. Computations of enhanced soot production in time-varying CH<sub>4</sub>/Air diffusion flames. *Combust. Flame*, 106:392–405, 1996.
- [73] B. Kärcher, O. Möhler, P. J. DeMott, S. Pechtl, and F. Yu. Insights into the role of soot aerosols in cirrus clouds formation. *Atmospheric Chemistry and Physics*, 7:4203–4227, 2007.
- [74] A. Kazakov, M. Frenklach, and H. Wang. Detailed modeling of soot formation in laminar premixed ethylene flames at a pressure of 10 bar. *Combust. Flame*, 100:111–120, 1995.
- [75] Ian M. Kennedy. Models of soot formation and oxidation. *Prog. Energy Comb. Sci.*, 23:95–132, 1997.
- [76] P. A. Kharecha and J. E. Hansen. Implications of "peak oil" for atmospheric CO<sub>2</sub> and climate. *Global Biogeochem.*, 22, 2008.

- [77] J.B.W. Kok. Non-linear processes in combustion dynamics driven acoustics. *To be submitted*, 2011.
- [78] S. Kraft and H. Mughrabi. Thermo-mechanical fatigue of the monocrystalline nickel-base superalloy cmsx-6. *Thermomechanical Fatigue Behaviour of Materials*, 1263, 1996.
- [79] K. K. Kuo. *Principles of combustion*. John Wiley & Sons, Inc., Hoboken, New Jersey, 2nd edition, 2005.
- [80] C. W. Lautenberger, J. L. de Ris, N. A. Dembsey, J. R. Barnett, and H. R. Baum. A simplified model for soot formation and oxidation in CFD simulation of non-premixed hydrocarbon flames. *Fire Safety Journal*, 40:141–176, 2005.
- [81] C. K. Law. *Combustion Physics*. Cambridge University Press, 2006.
- [82] C. K. Law. Combustion at a crossroads: Status and prospects. *Proc. Combust. Inst.* , pages 1–29, 2007.
- [83] P. D. Lax and B. Wendroff. Systems of conservation laws. *Commun. Pure Appl. Math.* , 13:217–237, 1960.
- [84] G. Lecocq, I. Hernández, D. Poitou, E. Riber, and B. Cuenot. Soot prediction by LES of complex geometry combustion chambers. In *3rd INCA Colloquium*, Toulouse, France, November 2011.
- [85] S.Y. Lee, S.R. Turns, and R.J. Santoro. Measurements of soot, OH and PAH concentrations in turbulent ethylene/air jet flames. *Combust. Flame* , 156:2264–2275, 2009.
- [86] A. H. Lefebvre. Flame radiation in gas turbine combustion chambers. *Int. J. Heat and Mass Transfer* , 27(9):1493–1510, 1984.
- [87] J.-Ph. L egier, T. Poinso, and D. Veynante. Dynamically thickened flame LES model for premixed and non-premixed turbulent combustion. In *Proc. of the Summer Program* , pages 157–168. Center for Turbulence Research, NASA Ames/Stanford Univ., 2000.
- [88] R. Lehoucq and D. Sorensen. ARPACK: Solution of Large Scale Eigenvalue Problems with Implicitly Restarted Arnoldi Methods. [www.caam.rice.edu/software/ARPACK](http://www.caam.rice.edu/software/ARPACK). User’s guide, 1997.
- [89] K. M. Leung and R. P. Lindstedt. A simplified reaction mechanism for soot formation in nonpremixed flames. *Combust. Flame* , 87:289–305, 1991.
- [90] M. Leyko, F. Nicoud, S. Moreau, and T. Poinso. Massively parallel LES of azimuthal thermo-acoustic instabilities in annular gas turbines. *C. R. Acad. Sci. M ecanique*, 337(6-7):415–425, 2009.

- [91] T. Lieuwen, S. Shanbhogue, S. Khosla, and C. Smith. Dynamics of bluff body flames near blowoff. In *45th AIAA Aerospace Sciences Meeting and Exhibit, Reno, Nevada*, January 2007.
- [92] T. Lieuwen and V. Yang. Combustion Instabilities in Gas Turbine Engines. Operational Experience, Fundamental Mechanisms and Modeling. In *Prog. in Astronautics and Aeronautics AIAA*, volume 210, 2005.
- [93] T. Lieuwen and B. T. Zinn. The Role of Equivalence Ratio Oscillations In Driving Combustion Instabilities In Low NOx Gas Turbines. *Proc. Combust. Inst.* , 27:1809–1816, 1998.
- [94] F. Liu, H. Guo, G. J. Smallwood, and Ö. L. Gülder. Effects of gas and soot radiation on soot formation in a coflow laminar ethylene diffusion flames. *J. Quant. Spect. and Radiative Transfer* , 73:409–421, 2002.
- [95] F. Liu, H. Guo, G. J. Smallwood, and M. El Hafi. Effects of gas and soot radiation on soot formation in counterflow ethylene diffusion flames. *J. Quant. Spect. and Radiative Transfer* , 84:501–511, 2004.
- [96] C. Marchal. *Modélisation de la formation et l’oxydation des suies dans un moteur automobile*. PhD thesis, Université d’Orléans, 2008.
- [97] F. Di Mare, W. P. Jones, and K. Menzies. Large Eddy Simulation of a model gas turbine combustor. *Combust. Flame* , 137:278–295, 2004.
- [98] J. Marquetand and U. Riedel. A two-equation model to simulate soot formation under shock-tube conditions. *Zeitschrift für Physikalische Chemie*, 223:605–619, 2009.
- [99] C. Martin, L. Benoit, Y. Sommerer, F. Nicoud, and T. Poinso. LES and acoustic analysis of combustion instability in a staged turbulent swirled combustor. *AIAA Journal* , 44(4):741–750, 2006.
- [100] R.S. Mehta, D.C. Haworth, and M.F. Modest. An assessment of gas-phase reaction mechanisms and soot models for laminar atmospheric-pressure ethylene-air flames. In *Proceedings of the Combustion Institute*, volume 32, pages 1327–1334, 2009.
- [101] M. F. Modest. *Radiative Heat Transfer*. Academic Press, 2nd edition, 2003.
- [102] J.B. Moss, C.D. Stewart, and K.J. Young. Modeling soot formation and burnout in a high temperature laminar diffusion flame burning under oxygen-enriched conditions. *Combust. Flame* , 101:491–500, 1995.
- [103] V. Moureau, G. Lartigue, Y. Sommerer, C. Angelberger, O. Colin, and T. Poinso. Numerical methods for unsteady compressible multi-component reacting flows on fixed and moving grids. *J. Comput. Phys.* , 202(2):710–736, 2005.

- [104] M.E. Mueller, G. Blanquart, and H. Pitsch. Hybrid method of moments for modeling soot formation and growth. *Combust. Flame* , 156(6):1143–1155, June 2009.
- [105] Praveen Narayanan and Arnaud Trouvé. Radiation-driven flame weakening effects in sooting turbulent diffusion flames. *Proc. Combust. Inst.* , 32:1481–1489, 2009.
- [106] K. Netzell, H. Lehtiniemi, and F. Mauss. Calculating the soot particle size distribution function in turbulent diffusion flames using a sectional method. *Proc. Combust. Inst.* , 31(1):667–674, 2007.
- [107] F. Nicoud, L. Benoit, and C. Sensiau. Acoustic Modes in Combustors with Complex Impedances and Multidimensional Active Flames. *AIAA Journal* , 45:426–441, 2007.
- [108] F. Nicoud, L. Benoit, C. Sensiau, and T. Poinso. Acoustic modes in combustors with complex impedances and multidimensional active flames. *AIAA Journal* , 45:426–441, 2007.
- [109] F. Nicoud and T. Poinso. Thermoacoustic instabilities: should the Rayleigh criterion be extended to include entropy changes ? *Combust. Flame* , 142:153–159, 2005.
- [110] N. Noiray, D. Durox, T. Schuller, and S. Candel. Self-induced instabilities of premixed flames in a multiple injection configuration. *Combust. Flame* , 145(3):435–446, 2006.
- [111] P. Palies. *Dynamique et instabilities de combustion de flammes swirlées*. Phd thesis, Ecole Centrale Paris, 2010.
- [112] N. Patel and S. Menon. Simulation of spray–turbulence–flame interactions in a lean direct injection combustor. *Combust. Flame* , 153(1-2):228–257, 2008.
- [113] T. Pedot. PhD thesis, INP Toulouse, 2011.
- [114] U. Piomelli. Wall-layer models for large-eddy simulations. *Prog. Aerospace Sci.* , 44(6):437–446, 2008.
- [115] T. Poinso and S. Lele. Boundary conditions for direct simulations of compressible viscous flows. *J. Comput. Phys.* , 101(1):104–129, 1992.
- [116] T. Poinso, A. Trouvé, D. Veynante, S. Candel, and E. Esposito. Vortex driven acoustically coupled combustion instabilities. *J. Fluid Mech.* , 177:265–292, 1987.
- [117] T. Poinso and D. Veynante. *Theoretical and Numerical Combustion*. R.T. Edwards, 2nd edition, 2005.

- [118] D. Poitou, J. Amaya, M. El Hafi, and B. Cuenot. Analysis of the interaction between turbulent combustion and thermal radiation using unsteady coupled LES/DOM simulations. *Combust. Flame*, 2011.
- [119] D. Poitou, M. El Hafi, and B. Cuenot. Analysis of radiation modeling for turbulent combustion: development of a methodology to couple turbulent combustion and radiative heat transfer in LES. *J. Heat Trans.*, 133, 2011.
- [120] S. B. Pope. *Turbulent flows*. Cambridge University Press, 2000.
- [121] A. A. Putnam. *Combustion driven oscillations in industry*. American Elsevier, fuel and energy science series, j.m. beer edition, 1971.
- [122] N.H. Qamar, Z.T. Alwahabi, Q.N. Chan, G.J. Nathan, D. Roekaerts, and K.D. King. Soot volume fraction in a piloted turbulent jet non-premixed flame of natural gas. *Combust. Flame*, 2009.
- [123] R. L. Raun, M. W. Beckstead, J. C. Finlison, and K. P. Brooks. A review of Rijke tube, Rijke burners and related devices. *Prog. Energy Comb. Sci.*, 19:313–364, 1993.
- [124] L. Rayleigh. On the theory of resonance. *Phil. Trans. R. Soc. Lond.*, 161:77–118, 1870.
- [125] L. Rayleigh. The explanation of certain acoustic phenomena. *Nature*, July 18:319–321, 1878.
- [126] A. Roshko. On the drag and shedding frequency of two-dimensional bluff bodies. Technical Report 3169, NACA, 1954.
- [127] A. Roux. *Simulation aux grandes échelles d'un statoréacteur*. PhD thesis, Université de Toulouse - Ecole doctorale MEGeP, CERFACS - CFD Team, Toulouse, July 2009.
- [128] S. Roux, G. Lartigue, T. Poinso, U. Meier, and C. Bérat. Studies of mean and unsteady flow in a swirled combustor using experiments, acoustic analysis and Large Eddy Simulations. *Combust. Flame*, 141:40–54, 2005.
- [129] M. Rudgyard. Integrated Preprocessing Tools for Unstructured Parallel CFD Applications. Technical Report TR/CFD/95/08, CERFACS, 1995.
- [130] M. A. Rudgyard. *Cell Vertex methods for compressible gas flows*. Phd thesis, Oxford University Computing Laboratory, 1990.
- [131] H.I.H. Saravanamuttoo, G.F.C. Rogers, H. Cohen, and P. Straznicky. *Gas Turbine Theory*. Prentice Hall, 6th edition, 2008.
- [132] R. F. Sawyer. Science based policy for addressing energy and environmental problems. *Proc. Combust. Inst.*, 32:45–56, 2009.

- [133] P. Schmitt. *Simulation aux grandes échelles de la combustion étagée dans les turbines à gaz et son interaction stabilité-polluants-thermique*. Phd thesis, INP Toulouse, 2005.
- [134] P. Schmitt, T. Poinsot, B. Schuermans, and K. P. Geigle. Large-eddy simulation and experimental study of heat transfer, nitric oxide emissions and combustion instability in a swirled turbulent high-pressure burner. *J. Fluid Mech.* , 570:17–46, 2007.
- [135] T. Schønfeld and M. Rudgyard. A cell-vertex approach to local mesh refinement for the 3-D Euler equations. In AIAA-94-0318, editor, *32nd Aerospace Sciences Meeting & Exhibit*, Reno, U.S.A., 1994. AIAA.
- [136] H. Sehitoglu. Thermo-mechanical fatigue life prediction methods. *Advances in Fatigue Lifetime Predictive Techniques*, 1122:47–76, 1992.
- [137] L. Selle, T. Poinsot, and B. Ferret. Experimental and numerical study of the accuracy of flame-speed measurements for methane/air combustion in a slot burner. *Combust. Flame* , 158(1):146–154, 2011.
- [138] A. Sengissen. *Simulation aux grandes échelles des instabilités de combustion: vers le couplage fluide/structure - TH/CFD/06/12*. Phd thesis, Université de Montpellier II, 2006.
- [139] A. Sengissen, J. F. Van Kampen, R. Huls, G. Stoffels, J. B. W. Kok, and T. Poinsot. LES and experimental studies of cold and reacting flows in a swirled partially premixed burner with and without fuel modulation. *Combust. Flame* , 150:40–53, 2007.
- [140] C. Sensiau. *Simulations numériques des instabilités thermoacoustiques dans les chambres de combustion aéronautiques - TH/CFD/08/127*. Phd thesis, Université de Montpellier II, - Institut de Mathématiques et de Modélisation de Montpellier, France, 2008.
- [141] J. Smagorinsky. General circulation experiments with the primitive equations: 1. The basic experiment. *Mon. Weather Rev.* , 91:99–164, 1963.
- [142] G.P. Smith, D.M. Golden, M. Frenklach, N.W. Moriarty, B. Eiteneer, M. Goldenberg, C.T. Bowman, R.K. Hanson, S.Song, Jr. W.C. Gardiner, V.V. Lissianski, and Z. Qin. <http://www.me.berkeley.edu/gri-mech/>.
- [143] M. D. Smooke, C. S. McEnally, L. D. Pfefferle, R. J. Hall, and M. B. Colket. Computational and experimental study of soot formation in a coflow, laminar diffusion flame. *Combust. Flame* , 117:117–139, 1999.
- [144] G. Staffelbach, L.Y.M. Gicquel, G. Boudier, and T. Poinsot. Large Eddy Simulation of self-excited azimuthal modes in annular combustors. *Proc. Combust. Inst.* , 32:2909–2916, 2009.

- [145] G. Staffelbach, P. Wolf, R. Balakrishnan, A. Roux, and T. Poinso. Massively parallel LES of azimuthal instabilities in helicopter combustion chambers. In NASA Ames/Stanford Univ. Center for Turbulence Research, editor, *Proc. of the Summer Program*, volume in press, 2010.
- [146] W. Strahle. Combustion noise. *Prog. Energy Comb. Sci.*, 4:157–176, 1978.
- [147] W. C. Strahle. On combustion generated noise. *J. Fluid Mech.*, 49:399–414, 1971.
- [148] A. Trouvé and Y. Wang. Large eddy simulation of compartment fires. *Int. J. Comput. Fluid Dynamics*, 24(10):449–466, 2010.
- [149] Combustion Division University of California San Diego, Center for Energy Research. <http://maeweb.ucsd.edu/combustion/cermech/index.html>.
- [150] U. Vandsburger, I. M. Kennedy, and I. Glassman. Sooting counterflow diffusion flames with varying oxygen index. *Combust. Sci. Tech.*, 39:263–285, 1984.
- [151] R. Viskanta and M. P. Mengüik. Radiation heat transfer in combustion systems. *Prog. Energy Comb. Sci.*, 13:97–160, 1987.
- [152] H. Watanabe, R. Kurose, S. Komori, and H. Pitsch. Effects of radiation on spray flame characteristics and soot formation. *Combust. Flame*, 152:2–13, 2008.
- [153] F. A. Williams. *Combustion Theory*. Benjamin Cummings, Menlo Park, CA, 1985.
- [154] F. Xu, P. B. Sunderland, and G. M. Faeth. Soot formation in laminar premixed ethylene/air flames at atmospheric pressure. *Combust. Flame*, 108:471–493, 1997.

# Appendices



# Appendix A

## The 1D code *CAN2SOOT*

### A.1 Introduction

A numerical tool has been developed that allows to calculate, in the post-processing stage, the soot mass fraction and the soot particle number density corresponding to a one-dimensional flame. The flame must have been previously computed with a code capable of handling steady-state one-dimensional flames, such as *CANTERA*, which is the case here. This tool has been written in structured Fortran 90 and needs the flame profiles as an input. Several hypothesis have been taken for the development of such tool:

1. The problem is time-independent and one-dimensional, no matter whether the flame is burner-stabilised or freely propagating.
2. There is no two-way coupling between the gas phase and the discrete phase (soot). Soot is dependent on the gas phase profiles, since its production and transport depend on gas phase variables such as density, temperature and species concentration. Gas phase, on the other hand, does not depend on soot variables, hence we eliminate its dependence through the soot-induced radiative term. This one-way dependence allows for the calculation of soot a posteriori.

### A.2 Derivation of the equations

#### A.2.1 Soot model and simplifications

The soot model used is a semi-empirical two-equations model proposed by Leung et al.[89]. Equations (A.1) and (A.2) describe the production and transport of these two variables, where  $Y_s$  is the soot mass fraction and  $n_s$  is the soot particle number density.

$$\frac{\partial \rho Y_s}{\partial t} + \frac{\partial \rho Y_s u_i}{\partial x_i} = -\frac{\partial}{\partial x_i} (\rho Y_s V_{t,i}) + \frac{\partial}{\partial x_i} \left( \rho \frac{\nu}{Sc_s} \cdot \frac{\partial Y_s}{\partial x_i} \right) + \dot{\omega}_s'' \quad (\text{A.1})$$

$$\frac{\partial}{\partial t} \left( \frac{\rho n}{N_0} \right) + \frac{\partial}{\partial x_i} \left( \frac{\rho n}{N_0} u_i \right) = - \frac{\partial}{\partial x_i} \left( \frac{\rho n}{N_0} V_{t,i} \right) + \frac{\partial}{\partial x_i} \left( \rho \frac{\nu}{Sc_s} \cdot \frac{\partial}{\partial x_i} \left( \frac{n}{N_0} \right) \right) + \dot{\omega}_n'' \quad (\text{A.2})$$

These equations are simplified applying the hypothesis mentioned. An additional hypothesis is taken, whereby the molecular diffusion term is neglected, as it is usually very small with respect to the thermophoretic transport term. After re-arranging, the resulting equations are:

$$\frac{\partial}{\partial x} (\rho Y_s (u + V_t)) - \dot{\omega}_{ys}'' = 0 \quad (\text{A.3})$$

$$\frac{\partial}{\partial x} \left( \frac{\rho n}{N_0} (u_i + V_t) \right) - \dot{\omega}_n'' = 0 \quad (\text{A.4})$$

Equations (A.3) and (A.4) express a balance between convection, thermophoretic transport and production/destruction of the soot variables.

## A.2.2 Discretization

In order to obtain a numerical solution, equations (A.3) and (A.4) must be discretised. The input flame profiles were obtained with *CANTERA* using a first-order spatial discretization, hence the equations will be discretised to first order too. Finite differences are used, making a distinction between interior points and the left boundary. The spatial domain is discretized by *CANTERA* using a non-uniform grid, this allows to solve the sharp gradients in the flame front without compromising the computational cost by introducing small cells everywhere. Upwind differences are used. An inlet boundary condition is imposed in the equations at the left boundary, leading to the following expressions:

– Left boundary

$$\frac{(u_i + V_{t,i}) (\rho_i Y_{s,i}) - \rho_{inlet} u_{inlet} Y_{s,inlet}}{\Delta x_i} - \dot{\omega}_{ys,i}'' = 0 \quad (\text{A.5})$$

$$\frac{(u_i + V_{t,i}) \left( \frac{\rho n}{N_0} \right)_i - u_{inlet} \left( \frac{\rho n}{N_0} \right)_{inlet}}{\Delta x_i} - \dot{\omega}_{n,i}'' = 0 \quad (\text{A.6})$$

– Interior points and right boundary

$$\frac{(u_i + V_{t,i}) (\rho_i Y_{s,i}) - (u_{i-1} + V_{t,i-1}) (\rho_{i-1} Y_{s,i-1})}{\Delta x_{i-1}} - \dot{\omega}_{ys,i}'' = 0 \quad (\text{A.7})$$

$$\frac{(u_i + V_{t,i}) \left( \frac{\rho n}{N_0} \right)_i - (u_{i-1} + V_{t,i-1}) \left( \frac{\rho n}{N_0} \right)_{i-1}}{\Delta x_{i-1}} - \dot{\omega}_{n,i}'' = 0 \quad (\text{A.8})$$

The subscript  $i$  makes reference to the value of the variable at the node  $i$ . The cell size being  $\Delta x_i = x_{i+1} - x_i$ .

Eqs. (A.5) - (A.8) are formulated for each of the two soot variables at each of the  $N$  nodes in which the domain is discretised, hence defining a system of  $2N$  non-linear equations for the variables  $\rho Y_s$  and  $\frac{n}{N_0}$ . The non-linearity is introduced through the non-linear dependence of the source terms  $\dot{\omega}_{ys}''$  and  $\dot{\omega}_n''$  on the soot variables.

## A.3 Numerical solution

### A.3.1 Problem formulation

Depending on the terms considered in the equations, these show a different nature. Then, the equations that describe the equilibrium problem are elliptic in nature, while the ones describing the time-dependent one are hyperbolic. Different methods must be used to solve each kind of problem. As is shown in section A.3.2, a combined approach is used in order to converge to a physical solution.

#### Equilibrium problem

Equations (A.5) to (A.8) yield a system of  $2N$  equations, where the first  $N$  equations correspond to the equations for  $\rho Y_s$  at each node and the equations  $N + 1$  to  $2N$  correspond to the equations for  $\frac{n}{N_0}$  at each node.

$$\begin{cases} f_1 \left( \rho_1 Y_{s,1}, \rho_2 Y_{s,2}, \dots, \rho_N Y_{s,N}, \left( \frac{\rho n}{N_0} \right)_1, \left( \frac{\rho n}{N_0} \right)_2, \dots, \left( \frac{\rho n}{N_0} \right)_N \right) = 0 \\ f_2 \left( \rho_1 Y_{s,1}, \rho_2 Y_{s,2}, \dots, \rho_N Y_{s,N}, \left( \frac{\rho n}{N_0} \right)_1, \left( \frac{\rho n}{N_0} \right)_2, \dots, \left( \frac{\rho n}{N_0} \right)_N \right) = 0 \\ \vdots \\ f_{2N} \left( \rho_1 Y_{s,1}, \rho_2 Y_{s,2}, \dots, \rho_N Y_{s,N}, \left( \frac{\rho n}{N_0} \right)_1, \left( \frac{\rho n}{N_0} \right)_2, \dots, \left( \frac{\rho n}{N_0} \right)_N \right) = 0 \end{cases} \quad (\text{A.9})$$

System (A.9) can be expressed in a more compact form as:

$$F(\mathbf{y}) = 0 \quad (\text{A.10})$$

The solution vector  $\mathbf{y}$  stores the values of  $\rho Y_s$  at the  $N$  nodes in its first  $N$  components and the values of  $\frac{\rho n}{N_0}$  at the  $N$  nodes at its  $N + 1$  to  $2N$  components.

#### Time-dependent problem

If the temporal variation term from Eqs.(A.1) and (A.2) is retrieved, then the problem to solve is time-dependent and must be integrated over time at

each point. For the sake of simplicity the Euler method is used, whereby the time derivative is approximated by a first order difference in time.

$$\frac{\partial \rho Y_s}{\partial t} \approx \frac{(\rho Y_s)^{n+1} - (\rho Y_s)^n}{\Delta t} \quad (\text{A.11})$$

$$\frac{\partial \left( \frac{\rho n}{N_0} \right)}{\partial t} \approx \frac{\left( \frac{\rho n}{N_0} \right)^{n+1} - \left( \frac{\rho n}{N_0} \right)^n}{\Delta t} \quad (\text{A.12})$$

Superscript  $n$  indicates the solution at instant  $t = n \cdot \Delta t$ .

### A.3.2 Problem solution

#### Solution of the time-dependent problem

Substituting expressions (A.11) and (A.12) in Eqs.(A.1) and (A.2), applying the spatial discretization and re-arranging, the following expression is obtained:

$$\mathbf{y}^{n+1} = \mathbf{y}^n - F \cdot \Delta t \quad (\text{A.13})$$

Vector  $\mathbf{y}$  stores both soot variables and  $F$  is the residuals vector of the discretized equations, which are advanced in time with a time step  $\Delta t$ .

#### Solution of the equilibrium problem

The method chose to solve the problem is the Newton-Raphson's method. It is an iterative method that allows to converge to the final solution from a given initial solution, as shown in Eqn. (A.14):

$$F(\mathbf{y}^k) + J(\mathbf{y}^k) \cdot (\mathbf{y}^{k+1} - \mathbf{y}^k) = 0 \quad (\text{A.14})$$

↓

$$\boxed{\mathbf{y}^{k+1} = \mathbf{y}^k - J^{-1}(\mathbf{y}^k) F(\mathbf{y}^k)} \quad (\text{A.15})$$

Index  $\mathbf{k}$  refers to the iteration number. As shown in Eqn. (A.15), in order to obtain a new solution  $\mathbf{y}^{k+1}$ , the solution vector  $\mathbf{y}^k$  at the previous iteration  $\mathbf{k}$  is needed, as well as the functions vector  $F$  and the jacobian matrix  $J$  both evaluated with the solution vector  $\mathbf{y}^k$ .

#### Jacobian matrix computation

Unlike other existing codes like *CANTERA* or *PREMIX*, the jacobian matrix is not approximated numerically, but it is calculated analitically, leading to exact results. This is possible due to the reduced number of equations to solve (only two variables), otherwise it would be a cumbersome task.

The expression for the jacobian matrix is:

$$J(\mathbf{y}^k) = \begin{bmatrix} \frac{\partial f_1}{\partial y_1} & \frac{\partial f_1}{\partial y_2} & \cdots & \frac{\partial f_1}{\partial y_N} & \frac{\partial f_1}{\partial y_{N+1}} & \frac{\partial f_1}{\partial y_{N+2}} & \cdots & \frac{\partial f_1}{\partial y_{2N}} \\ \frac{\partial f_2}{\partial y_1} & \frac{\partial f_2}{\partial y_2} & \cdots & \frac{\partial f_2}{\partial y_N} & \frac{\partial f_2}{\partial y_{N+1}} & \frac{\partial f_2}{\partial y_{N+2}} & \cdots & \frac{\partial f_2}{\partial y_{2N}} \\ \vdots & \vdots & \vdots & \vdots & \vdots & \vdots & \ddots & \vdots \\ \frac{\partial f_{2N}}{\partial y_1} & \frac{\partial f_{2N}}{\partial y_2} & \cdots & \frac{\partial f_{2N}}{\partial y_N} & \frac{\partial f_{2N}}{\partial y_{N+1}} & \frac{\partial f_{2N}}{\partial y_{N+2}} & \cdots & \frac{\partial f_{2N}}{\partial y_{2N}} \end{bmatrix} \quad (\text{A.16})$$

As said before, the vector  $\mathbf{y} \in \mathbb{R}^{2N}$  stores both soot variables, hence the relations  $y_i = \rho_i Y_{s,i}$  and  $y_{i+N} = \left(\frac{\rho^n}{N_0}\right)_i$ . Taking expressions (A.5) - (A.8) for the  $f_i$  functions and performing the corresponding derivatives, the jacobian matrix is reduced to:

$$J(\mathbf{y}^k) = \begin{bmatrix} \frac{\partial f_1}{\partial y_1} & 0 & 0 & \cdots & 0 & \frac{\partial f_1}{\partial y_{N+1}} & 0 & \cdots & \cdots & 0 \\ \frac{\partial f_2}{\partial y_1} & \frac{\partial f_2}{\partial y_2} & 0 & \cdots & 0 & \ddots & \frac{\partial f_2}{\partial y_{N+2}} & \ddots & 0 & \vdots \\ 0 & \frac{\partial f_3}{\partial y_2} & \frac{\partial f_3}{\partial y_3} & 0 & \ddots & \ddots & 0 & \ddots & \ddots & \vdots \\ \vdots & \ddots & \ddots & \ddots & \ddots & \vdots & \ddots & \ddots & \ddots & 0 \\ \vdots & \vdots & 0 & \frac{\partial f_N}{\partial y_{N-1}} & \frac{\partial f_N}{\partial y_N} & 0 & \ddots & \vdots & 0 & \frac{\partial f_N}{\partial y_{2N}} \\ 0 & \cdots & \vdots & 0 & \frac{\partial f_{N+1}}{\partial y_{N+1}} & 0 & 0 & \ddots & \vdots & 0 \\ 0 & \cdots & \vdots & 0 & \frac{\partial f_{N+2}}{\partial y_{N+1}} & \frac{\partial f_{N+2}}{\partial y_{N+2}} & 0 & \cdots & \vdots & \vdots \\ \vdots & \vdots & 0 & \ddots & 0 & \ddots & \ddots & \ddots & \ddots & \vdots \\ \vdots & \vdots & 0 & \ddots & \ddots & \ddots & \ddots & \ddots & \vdots & \vdots \\ \vdots & \vdots & \vdots & \vdots & \ddots & \ddots & \ddots & \ddots & \ddots & 0 \\ 0 & \cdots & \cdots & \cdots & \cdots & \cdots & \cdots & 0 & \frac{\partial f_{2N}}{\partial y_{2N-1}} & \frac{\partial f_{2N}}{\partial y_{2N}} \end{bmatrix} \quad (\text{A.17})$$

The components of the jacobian matrix are then, for  $i = 1, N$ :

$$\begin{aligned} \frac{\partial f_i}{\partial y_i} &= \frac{\partial f_i}{\partial \rho_i Y_{s,i}} = \frac{u_i + V_{t,i}}{x_i} - \frac{\partial \omega''_{ys,i}}{\partial \rho_i Y_{s,i}} \\ \frac{\partial f_i}{\partial y_{i-1}} &= \frac{\partial f_i}{\partial \rho_{i-1} Y_{s,i-1}} = \frac{u_i + V_{t,i}}{x_i} \\ \frac{\partial f_i}{\partial y_{N+i}} &= \frac{\partial f_i}{\partial \left(\frac{\rho^n}{N_0}\right)_i} = -\frac{\partial \omega''_{ys,i}}{\partial \left(\frac{\rho^n}{N_0}\right)_i} \\ \frac{\partial f_{N+i}}{\partial y_{N+i}} &= \frac{\partial f_{N+i}}{\partial \left(\frac{\rho^n}{N_0}\right)_i} = \frac{u_i + V_{t,i}}{x_i} - \frac{\partial \omega''_{n,i}}{\partial \left(\frac{\rho^n}{N_0}\right)_i} \\ \frac{\partial f_{N+1}}{\partial y_{N+i-1}} &= -\frac{\partial f_{N+1}}{\partial \left(\frac{\rho^n}{N_0}\right)_{i-1}} = -\frac{u_{i-1} + V_{t,i-1}}{x_i} \end{aligned}$$

All the other elements of the jacobian matrix are null.

**Matrix operations**

As seen in (A.17), the jacobian matrix is a sparse matrix (only three bands with non-null terms) that has to be inverted at each iteration in order to calculate the new solution.

To do that, the routine makes use of the LAPACK [5] libraries, as they are optimised routines for handling matrices.

**Combined solution procedure**

The solution is sought applying both solution methods described in sections A.3.2 and A.3.2. For the Newton method to converge it is a must to provide it with a sufficiently accurate initial solution. This is done by advancing the equations in time and feeding the Newton method with the outcome of this time stepping procedure. If the Newton method does not converge then the equations are advanced in time again. This iterative procedure is illustrated in Fig.(A.1).

Advancing the equations in time allows to bring the solution into the convergence domain of the Newton method.

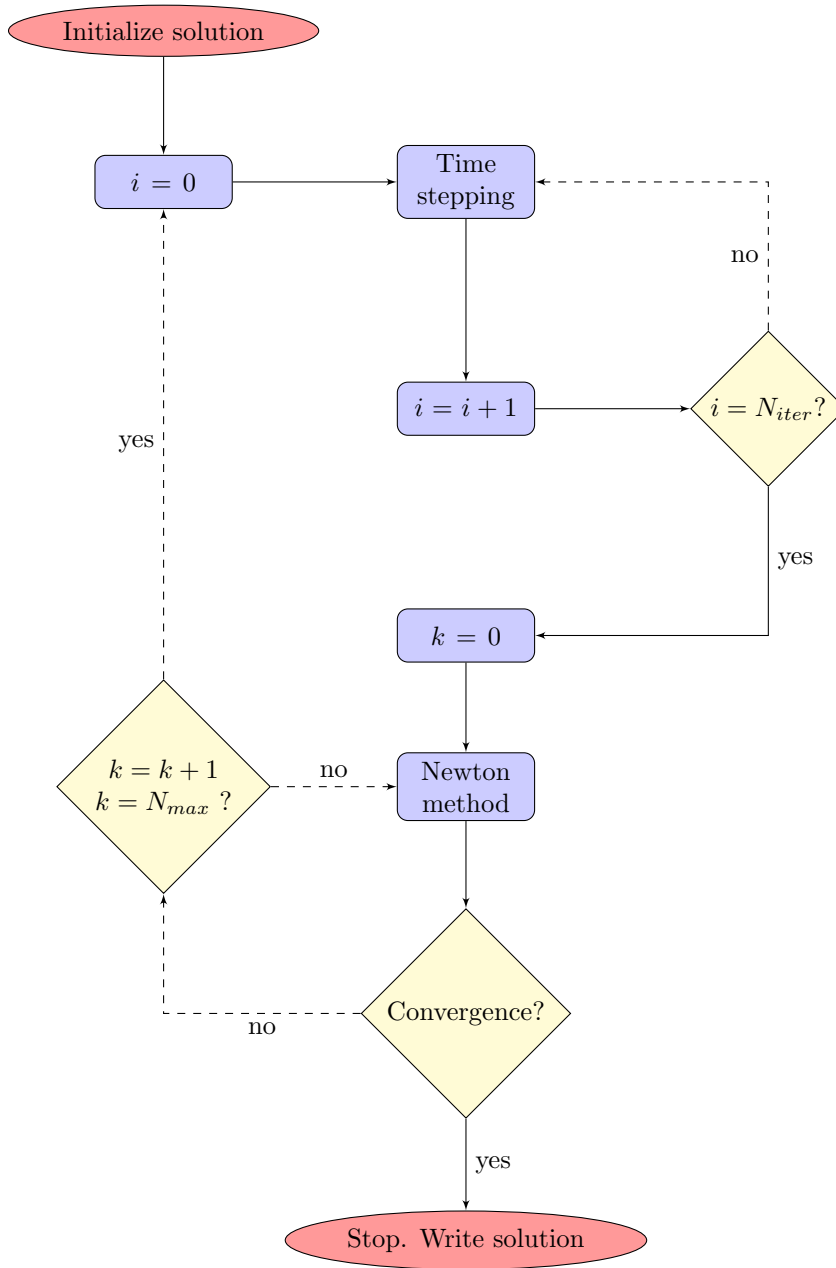


Figure A.1: Flow chart of the solution procedure.